FINITE ELEMENT ANALYSIS OF LEFT VENTRICLE MOTION AND MECHANICAL PROPERTIES IN THREE DIMENSIONS

ABDALLAH IBRAHIM MOHAMMED HASABALLA

DISSERTATION SUBMITTED IN FULFILLMENT
OF THE REQUIREMENTS FOR THE DEGREE OF
MASTER OF ENGINEERING SCIENCE

FACULTY OF ENGINEERING
UNIVERSITY OF MALAYA
KUALA LUMPUR

2014

UNIVERSITI MALAYA

ORIGINAL LITERARY WORK DECLARATION

Name of Candidate: **Abdallah Ibrahim Mohammed** (I.C/Passport No:

Registration/Matric No: **KGA110058**

Name of Degree: **Master of Engineering Science (MEngSc).**

Title of Project Paper/Research Report/Dissertation/Thesis ("this work")/:

"Finite Element Analysis of Left Ventricle Motion and Mechanical Properties in Three Dimensions"

Field of Study: **Finite Element Analysis**

I do solemnly and sincerely declare that:

(1) I am the sole author/writer of this work;

(2) This work is original;

(3) Any use of any work in which copyright exists was done by way of fair dealing and for permitted purposes and any excerpt or extract from, or reference to or reproduction of any copyright work has been disclosed expressly and sufficiently and the title of the work and its authorship have been acknowledged in this work;

(4) I do not have any actual knowledge nor do I ought reasonably to know that the making of this work constitutes an infringement of any copyright work;

(5) I hereby assign all and every rights in the copyright to this work to the University of Malaya ("UM"), who henceforth shall be owner of the copyright in this work and that any reproduction or use in any form or by any means whatsoever is prohibited without the written consent of UM having been first had and obtained;

(6) I am fully aware that if in the course of making this work I have infringed any copyright whether intentionally or otherwise, I may be subject to legal action or any other action as may be determined by UM.

    Candidate's Signature   Date:

Subscribed and solemnly declared before,

    Witness's Signature   Date:

Name:

Designation:

ABSTRACT

Despite the wide variety of research in medicine and bioengineering treatment strategies developed over the last half century, heart disease remains among the most serious diseases threatening human longevity. Modeling the mechanics of the human myocardium, particularly the left ventricle, which is the main pumping chamber and most common site for heart disease, plays a significant role in better understanding the performance of the heart in healthy and diseased states. The core part of this work constitutes the implementation of a more realistic three-dimensional finite element model of the human left ventricle to provide a reliable description of both myofiber orientation and material characteristics. In this study, direct and inverse finite element methods of human left ventricle were developed. The direct finite element method is suitable for studying the influences of different mesh densities, constitutive models, fibers orientations, and myofiber volume fractions. Meanwhile, the inverse finite element method served to determine the bulk modulus of the left human ventricle during a cardiac cycle. The simulation results indicate that the changes in transverse angle hardly affected the pressure-volume relation of the ventricle, but significantly do so with changes in helix angle (up to 50% change). The ejection fraction decreased with decreasing total volume fraction (increasing the infarct myocardial volume). Total volume fraction of less than 60% deceased the ejection fraction by over 50%. Thus, the myofibers' architecture plays a significant role in the mechanics of the left ventricle. Finally, the myocardium bulk modulus may be employed as a diagnostic tool (clinical indicator) for heart ejection fraction, and hence, heart function performance. Therefore, this study offers a new perspective and means of studying living-myocardium tissue properties. The research may also pave the way towards more effective treatment.

ABSTRAK

Walaupun terdapat pelbagai kajian dalam bidang perubatan dan rawatan biokejuruteraan yang dibangunkan sejak lebih setengah abad yang lalu, penyakit jantung masih kekal sebagai salah satu penyakit yang serius yang memberi ancaman kepada jangka hayat umur manusia. Model mekanik myocardium manusia terutamanya ventrikel kiri, yang merupakan pam utama dan lokasi yang paling biasa bagi penyakit jantung, memainkan peranan penting dalam pemahaman yang lebih baik terhadap prestasi jantung di dalam keadaan yang sihat dan berpenyakit. Dengan pengetahuan ini, kita akan dapat mengenal pasti sindrom kegagalan jantung dan kajian mengenai kuantiti yang tidak boleh diukur dalam suasana klinikal atau eksperimen. Bahagian utama karya ini adalah pelaksanaan model unsur terhingga tiga dimensi yang lebih realistik daripada ventrikel kiri manusia yang memberikan penerangan yang lebih mantap mengenai orientasi myofiber dan sifat-sifat bahan. Dalam kajian ini , kaedah unsur terhingga langsung dan tidak langsung untuk ventrikel kiri manusia telah dibangunkan. Kaedah langsung unsur terhingga adalah sesuai untuk mengkaji pengaruh ketumpatan yang mesh yang berbeza, model juzuk yang berbeza, orientasi myofiber yang berbeza , dan pecahan isipadu myofiber yang berbeza. Sementara itu, kaedah unsur terhingga secara songsang telah digunakan untuk menentukan modulus pukal ventrikel kiri manusia semasa kitaran jantung. Keputusan simulasi menunjukkan bahawa perubahan dalam sudut melintang tidak memberi kesan terhadap hubungan antara tekanan-isipadu ventrikel, namun perubahan dalam sudut helix mempunyai kesan signifikan (perubahan sehingga 50%) terhadap hubungan antara tekanan-isipadu ventrikel. Pecahan pelemparan dikurangkan dengan mengurangkan pecahan isipadu total (meningkatkan isipadu infarct myocardium). Pecahan isipadu total yang kurang daripada 60% menurunkan pecahan pelemparan sehingga 50%. Maka, seni bina myofiber memainkan peranan penting dalam mekanisme ventrikel kiri.

Justeru modulus myocardium pukal boleh digunakan sebagai alat diagnostik (penunjuk klinikal) daripada pecahan pelemparan jantung, dan dengan itu prestasi fungsi jantung. Oleh itu, kajian ini menawarkan perspektif baru dan kaedah untuk kajian hidup – sifat tisu myocardium. Penyelidikan ini juga boleh membuka jalan ke arah rawatan yang lebih berkesan.

ACKNOWLEDGEMENT

First and foremost I praise and acknowledge Allah, the most gracious and the most merciful, for giving me the strength and ability to complete this thesis.

I express my profound sense of reverence to my parents for always supporting me and keeping me focused on the fact that in the end only eternal values will truly matter.

Special appreciation goes to my supervisors Associate Prof. Dr. Mohsen Abdel Naeim Hassan, and Dr. Noor Azizi Bin Mardi for their assistance and advice during this work.

My deepest gratitude goes to Dr. Reza Mahmoodian for his expert advice on thesis formatting.

Last but not least, my deepest gratitude goes to the Mechanical Engineering Department, University of Malaya, for providing the equipment and opportunity to study towards a Master of Engineering Science (MEngSc). I would also like to thank the Centre of Advanced Manufacturing and Material Processing (AMMP Centre) for the financial support.

TABLE OF CONTENTS

LIST OF FIGURES

LIST OF TABLES

LIST OF SYMBOLS AND ABBREVIATIONS

Symbols	Description
$\widetilde{t}$	Nominal traction force vector
μ_n, α_n	Material constants (Ogden parameters)
Δu	Incremental displacement vector
$\Delta \sigma$	Incremental stress vector
$\Delta \epsilon$	Incremental strain vector
B	Strain-displacement relation matrix
b, $\{b^i\}$	External body force vector
C, $\{C_{MN}\}$	Right Cauchy-Green or Green deformation tensor
Ca^{2+}	Calcium ion
C_{ij}	ij-th component of the right Cauchy-Green deformation tensor C
D	Stress-strain relation matrix
dX	Undeformed line segment
dx	Deformed line segment
E	Young's modulus
E_{def}	Deformation energy
E_{exf}	Energy due to external forces
E_g	Global energy functional
f, $\{f^i\}$	Acceleration vector
F, $\{F^i_M\}$	Deformation gradient tensor
I	Vector of resorting loads corresponding to element internal loads
$\mathbf{i}_j$	Base vectors for the rectangular cartesian coordinate system
J	Volumetric ratio
K	Bulk modulus
k	Global stiffness matrix
k^e	Element stiffness matrix
n	Number of element in the left ventricle model
N	Element shape function
$\emptyset_{tot}$	Total myofiber volume fractions

P	Applied load vector
P_{bp}	Force generated by blood pressure on the surface of the endocardium
P_{ma}	Active force generated by the myocardium muscles
P_{sp}	Force generated by pressure external from surrounding organs
S	First Piola-Kirchhoff stress tensor or surface on V where $\tilde{t}$ is applied
s, $\{s^i\}$	External stress vector
s^{endo}	Surface area of elements on the endocardial surface
s^{epi}	Surface area of elements on the epicardial surface
t, $\{t^i\}$	Internal stress or traction vector
T, $\{T^{MN}\}$	Second Piola-Kirchhoff stress tensor
TOL	Relative displacement tolerance
u, u_0	Displacement vector in deformed and undeformed body, respectively
V	Initial configuration of the material
v, $\{v^i\}$	Velocity vector
v^e	Volume of the element
W	Strain energy function
W_{act}	Active component of strain energy function
W_{pass}	Passive component of strain energy function
α	A large value corresponding to the bulk modulus
β	Helix angle
δC_{ij}	Variation of C_{ij} due to δu
δu	Variation of the displacement vector u
δu_i	*i-th* component of δu
η	Transverse angle
λ	Lagrange multiplier
$\lambda_1, \lambda_2, \lambda_3$	Principal stretch ratios
σ^{ij}	Physical Cauchy stress components
Ψ	A function to describe volume change
ν	Poisson's ratio
ρ, ρ_0	Densities for deformed and undeformed configurations, respectively

Abbreviations	Description
3D	Three dimensions
ADP	Adenosine diphosphate
ATP	Adenosine triphosphate
AV	Atrioventricular
CAD	Coronary Artery Disease
DT	Diffusion tensor
ECG	Electrocardiography
EDV	End diastolic volume
EF	Ejection fraction
ESV	End systolic volume
FE	Finite element
LV	Left ventricle
MI	Myocardial infarction
MRI	Magnetic Resonant Imaging
MRT	Magnetic Resonant Tagging
P	Phosphate
PV	Pressure-Volume
SA	Sinus-atrial
SV	Stroke volume
WHO	World Health Organization

CHAPTER 1: INTRODUCTION

1.1 General background

Heart disease is the leading cause of death nearly in the entire world, especially in developed countries. According to the World Health Organization (WHO), deaths caused by heart disease each year are more than by cancer, diabetes, respiratory diseases, and accidents combined. Death attributable to heart disease in the United States of America today is over 25% of the total number of deaths.

Computational cardiac models are undoubtedly powerful tools used to guide successful patient therapy design. They not only play a crucial role in reproducing biological cardiac behavior by incorporating experimental findings but also serve as a virtual testing environment for predictive analyses where experimental techniques fall short.

1.2 Anatomy and functions of the heart

The heart is a hollow muscular organ located behind and to the left of the breastbone and between the lungs (Toronto, 1964). The heart is contained within a sack called "the pericardium," which sits on top of the diaphragmatic muscle and is surrounded by the ribcage. These structures all serve to protect the heart. As shown in Figure 1.1, the pericardium consists of two parts, the inner serous pericardium and the outer fibrous pericardium. (Iaizzo, 2009).
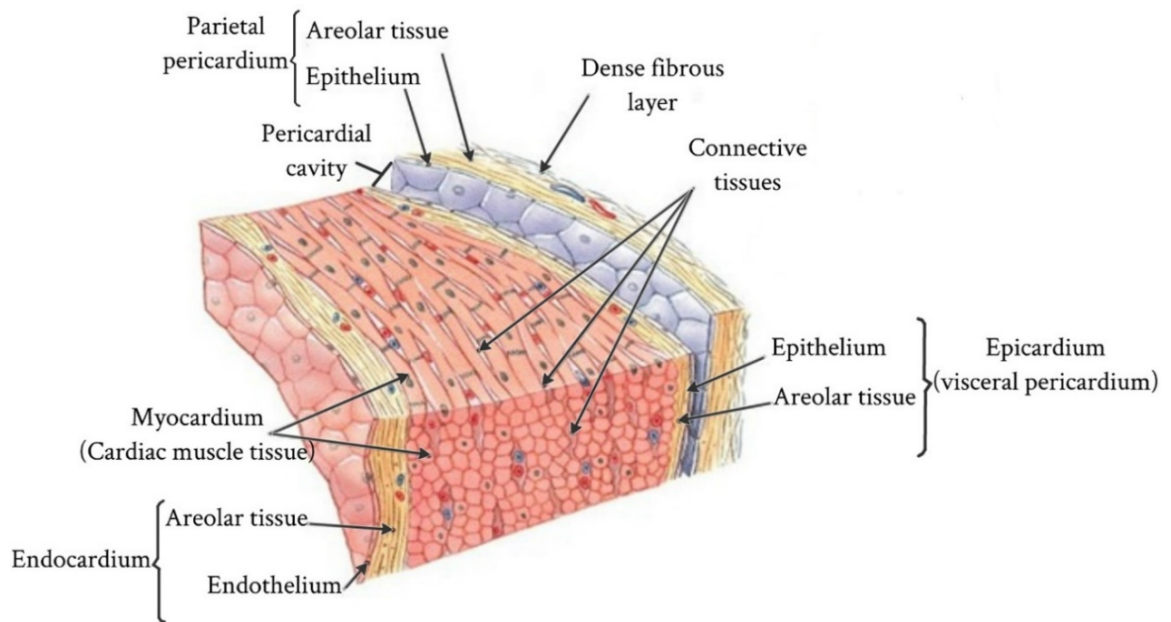
Figure 1.1: Internal anatomy of the heart. The walls of the heart consist of three layers – the superficial epicardium, the middle myocardium composed of cardiac muscle, and the inner endocardium (Iaizzo, 2009)

The heart has two separate pumps, the right and left side, which work together. The right side of the heart collects de-oxygenated blood from the body via the superior and inferior vena cava in the right atrium; the right atrium pumps the blood through the tricuspid valve into the right ventricle; the right ventricle pumps the blood through the pulmonary valve into the lungs -- a cycle known as "pulmonary circulation." In the lungs, carbon dioxide is removed from the blood and oxygen is picked up. Meanwhile, the left side of the heart collects oxygenated blood from the lungs via the pulmonary veins in the left atrium; the left atrium pumps the blood through the bicuspid valve into the left ventricle (LV); the LV pumps the blood out of the heart through the aortic valve, a cycle called "systemic circulation." When this pumping cycle is complete, the aortic valve closes to prevent blood from dropping back into the heart (Figure 1.2) (Martini et al., 2012).
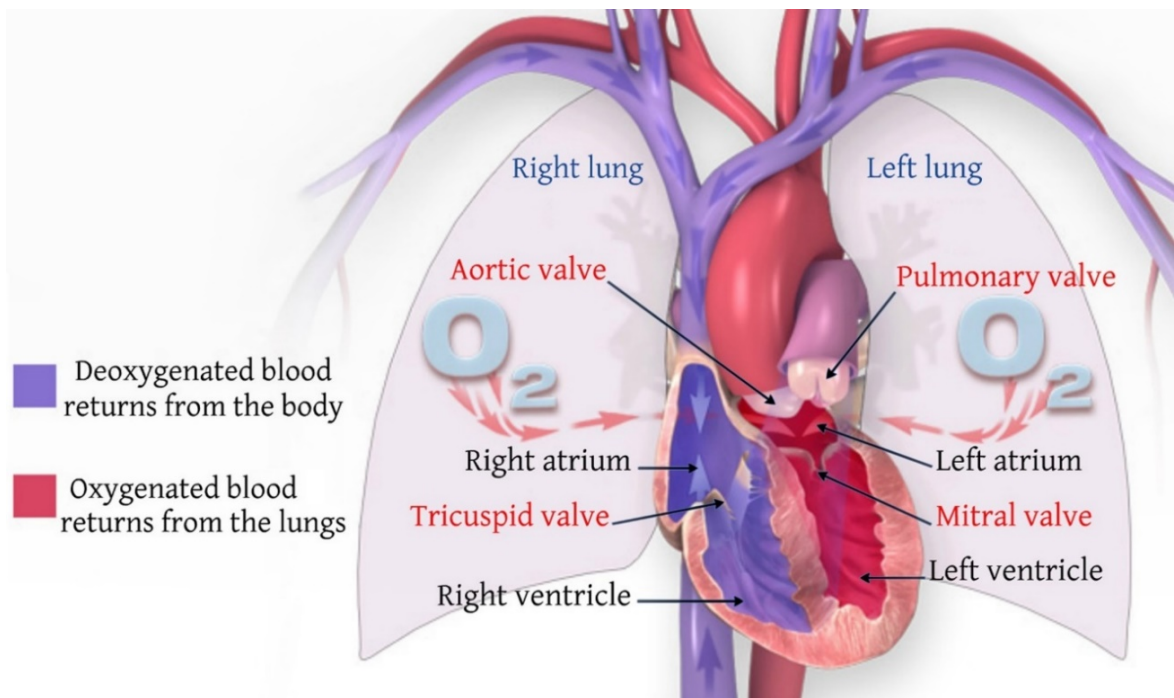
Figure 1.2: Blood flow (American Heart Association, 2013)

As shown in Figure 1.2, the heart is a single organ divided into four chambers, two at the top: right and left atria, and two at the bottom: right and left ventricles (Phibbs, 2007). The upper chambers, the atria, receive blood returning to the heart and transfer it to the lower chambers, the ventricles, which pump blood from the heart (Sherwood, 2012). Blood flows through the heart in one direction from veins to atria, to ventricles, and to arteries (Gray & Lewis, 1918). The four valves are the tricuspid, pulmonary, mitral, and aortic valves (Figure 1.2). The tricuspid valve positioned between the right heart atrium and right ventricle controls blood flow between the right atrium and right ventricle. The pulmonary valve separates the right ventricle from the pulmonary artery, and it lies between the right ventricle and pulmonary artery. The pulmonary artery takes deoxygenated blood from the heart to the lungs. The mitral valve (bicuspid valve) located at the left side of the heart, between the left atrium and LV, allows oxygen-rich blood from the lungs to flow between the left atrium and

LV. The aortic valve separates the LV from the aorta and controls blood flow between the LV and the main blood vessel leaving the heart (Snell, 2011).

The sinus-atrial (SA) node contains pacemaker cells, which help the heart beat in a regular rhythm (Figure 1.3). The SA node's activity, i.e., the heart rate, is essentially controlled by three sources. First, the SA node has its own intrinsic rhythm (more than 60 beats per minute). Second, the sympathetic as well as the parasympathetic nervous system are directly coupled to the SA node and have an increasing or decreasing effect on the heart rhythm, respectively. Third, a number of hormones, such as adrenalin, influence the SA node's activity (Gacek, 2012).

The SA node sends out a regular electrical impulse, causing the atria to contract and pump blood into the bottom chambers, or ventricles. After the atria contract, the electrical impulse reaches the ventricles through a junction box called the atrioventricular (AV) node, which is located at the base of the right atrium. The AV node is only a conductive link between the atria and ventricles. This node acts as a filter that permits the atrial contraction to fill the ventricles with blood before the ventricles begin to contract. The bundle of His represents a continuation of the AV node and provides the electrical connection to the ventricles. It separates into two parts: one that activates the right ventricle and the other the LV. These parts descend on either side of the septum and divide into hundreds of tiny nerve fibrils called Purkinje fibers throughout the wall of each ventricle. Purkinje fibers are conductile cells that conduct action potentials very rapidly. These fibers, however, cause the ventricles to contract and pump out the blood. The blood from the right ventricle goes to the lungs and the blood from the LV goes to the body (Berne & Levy, 1996; Smith & Roberts, 2011). This process takes 0.8 seconds and is a single heartbeat. The electrical currents occurring during depolarization (contraction) and repolarization (relaxation) of the myocytes are powerful

enough to be detected by electrodes on the surface of the body using conductive adhesive patches. The obtained recording is called the electrocardiogram (ECG). By comparing the information obtained from an ECG, a clinician can monitor the heart's electrical activity, which is directly related to the performance of specific nodal, conducting, and contractile components (Davey et al., 2008).
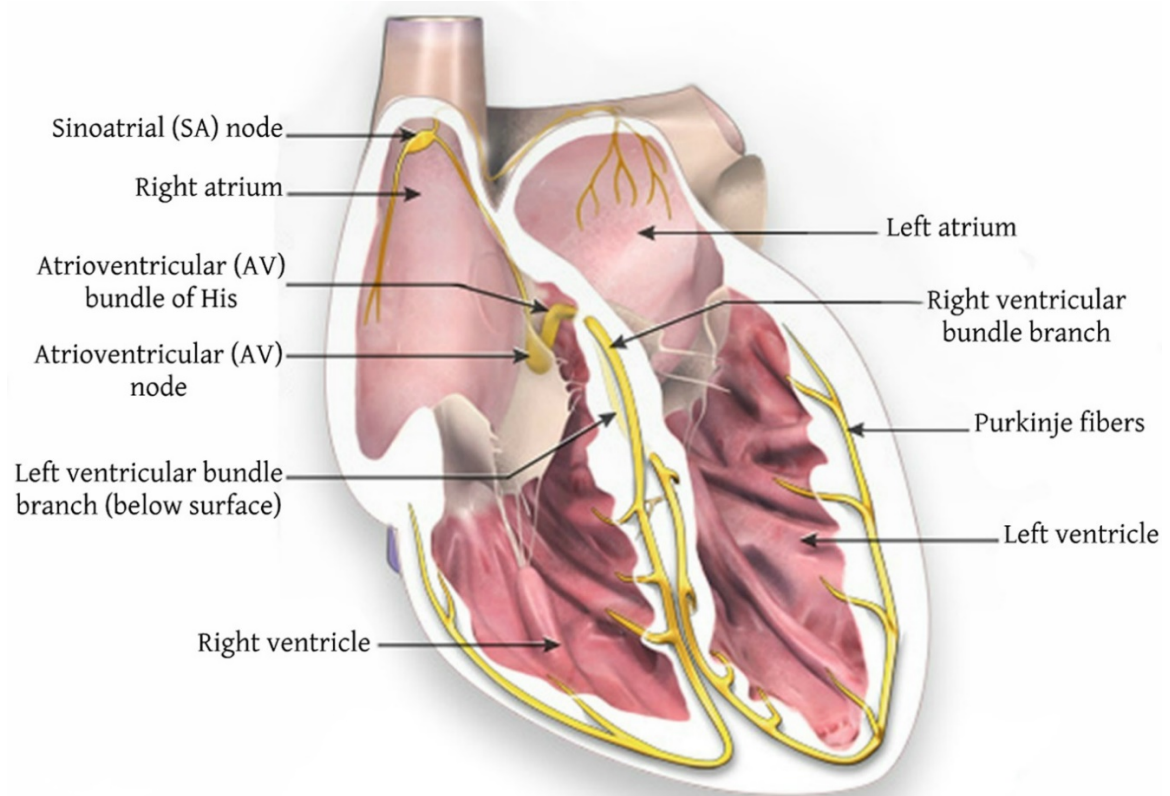
Figure 1.3: Conduction system of the heart (American Heart Association, 2013)

The ECG is subdivided into two segments that are separated by three waves: the P wave represents atrial contraction, the complex QRS represents LV depolarization, and the T wave represents the ventricles' repolarization (Figure 1.4).
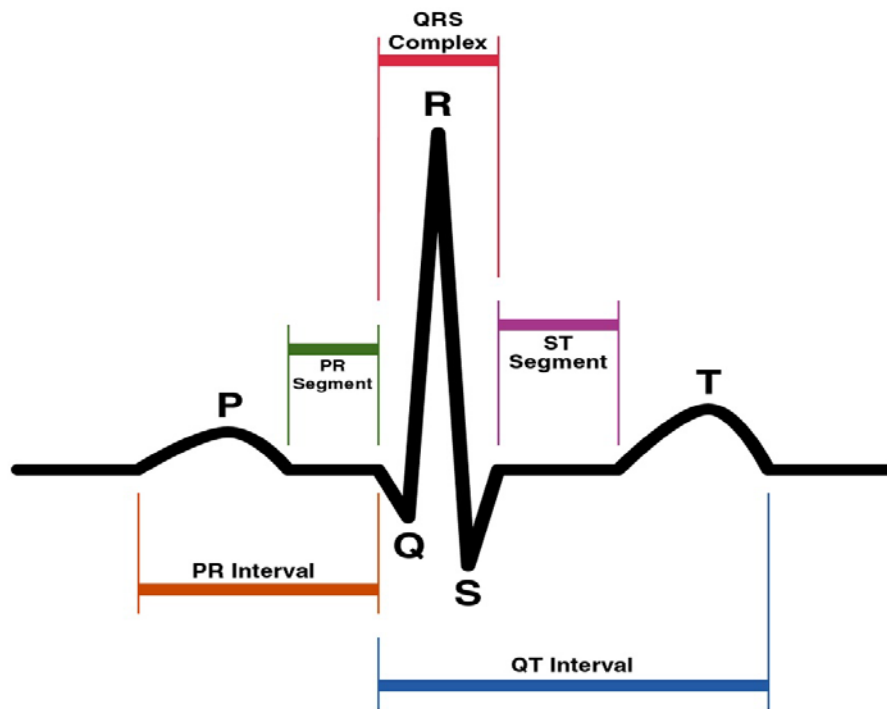
Figure 1.4: Normal electrocardiogram (Rn, 2007)

The first, PR segment, represents the time delay of the AV node's electrical stimulation. The second, ST segment, denotes the time delay between the end of ventricle contraction and beginning of full ventricular relaxation. The PR interval extends from the start of atrial depolarization to the start of the QRS complex (ventricular depolarization) rather than to R, because in abnormal ECGs the peak can be difficult to determine. PR interval of more than 0.2 seconds may be indicative of damage to the conducting pathways or AV node. The QT interval indicates the time required for the ventricles to undergo a single cycle of depolarization and repolarization. It is usually measured from the end of the PR interval rather than from the bottom of the Q wave. The QT interval can be longer due to conduction problems, coronary ischemia, or myocardial damage. A congenital heart defect can cause sudden death without warning, but may be detectable as a prolonged QT interval (Sperelakis et al., 2000; Walsh & Crumbie, 2007).

1.3   The cardiac cycle

There is continuous demand for blood in the human body. To fulfill this demand the heart
beats about seventy times a minute to pump blood through the human body. The events that
occur from the beginning of one heartbeat to the beginning of the next are known as a
"cardiac cycle." The cardiac cycle is divided into two main stages: a period of relaxation
called diastole, in which the heart fills with blood, followed by a period of contraction, or
systole, and ejection of blood. During every beat, the heart undergoes seven different phases
(Figure 1.5). Each of these is reviewed in more detail below.
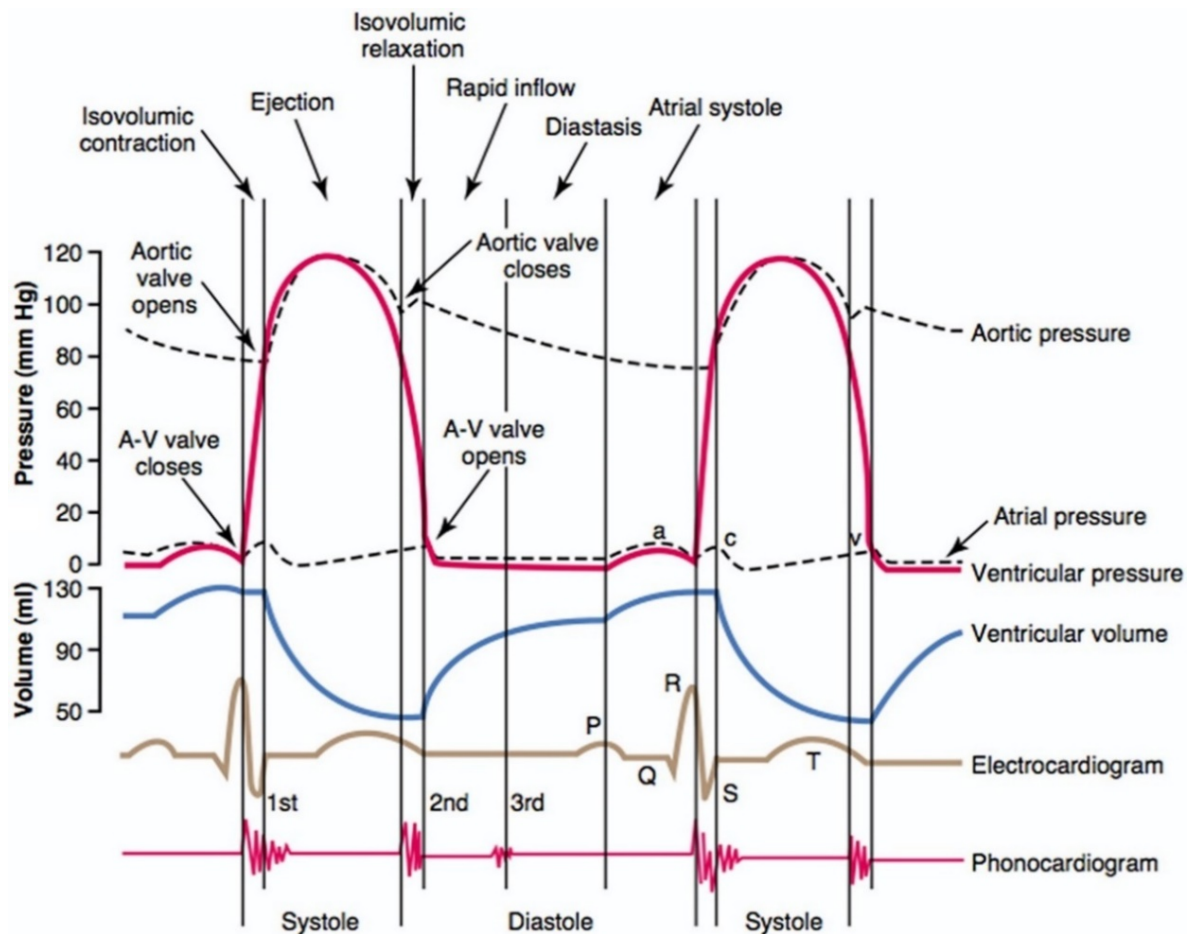
Figure 1.5: Cardiac cycle for left ventricle function (Hall, 2011)

Atrial Systole (Atrial Contraction) is the first phase of a cardiac cycle, which occurs when the left atrium contracts causing an increase in left atrial pressure (Sandhar, 2004). Following atrial contraction, the left atrial pressure eventually falls causing the mitral valve to close, thus concluding the diastole phase (Klabunde, 2011).

Isovolumetric Contraction: This is when the valves of the left and right ventricles are closed and the myocardium is contracting. The cavity pressure increases while the volume stays constant (Sicar, 2008).

Rapid Ejection: As soon as the pressure in the left ventricle exceeds the pressure in the aorta, the aortic valves open and blood flows rapidly from the ventricle into the aorta. This corresponds to a sharp decrease in ventricular volume. Atrial pressure drops below venous pressure, and the atria begin to fill at this time (Rhoades & Bell, 2009).

Reduced Ejection: Following rapid ejection, the rate of outflow from the ventricle decreases and the ventricular and aortic pressures begin to decrease. At this point, muscle fibres have become shorter and can no longer contract forcefully. The venous pressure is still greater than atrial pressure, and the atria are still filling (Deepa, 2012).

Isovolumetric Relaxation: During the isovolumetric relaxation phase the myocardium is relaxing and all valves are closed, so the pressure and tension drops very rapidly as the volume of the ventricles does not change; the residual volume of blood in the LV is approximately 40-50 ml (Cosin Aguilar et al., 2009).

Rapid Filling Phase (Rapid Inflow): In the rapid filling phase, ventricular pressure decreases below atrial, the atrioventricular valves open and filling occurs rapidly from 50 to 85 ml (Sherwood, 2012).

Reduced Filling Phase (Diastasis): It is the longest phase of the cardiac cycle in which the left ventricle continues to fill with blood and expands slowly until nearly full (Sembulingam & Sembulingam, 2002). The typical amount of blood in the LV after filling is approximately 110-120 ml. As the ventricle fills, the intraventricular pressure increases, slowing the filling rate (Levy et al., 2007).

1.4 Myocardium contraction

The myocardium consists of muscle fibers held together by collagen fibers (Figure 1.6). The muscle fibers, or myocytes, make up approximately 70% of the myocardial volume. The network of collagen fibers accounts for only about 1.5% of the myocardium (LeGrice et al., 1995; Stevens & Hunter, 2003; Aaronson et al., 2012).

The muscle fiber actually consists of a bundle of several hundred smaller fibers called myofibrils. As seen in Figure 1.7, the muscle fibers themselves make up larger units called fascicles. Numerous fascicles, in turn, are bound together by fascia to form a section of muscle. There are approximately one hundred fibers in a fascicle, and each muscle fiber contains between one thousand and two thousand myofibrils. When viewed under an electron microscope, it is visible that each myofibril is primarily composed of two kinds of filaments (thick and thin) organized into regular, repeating sub-units. These sub-units are called sarcomeres (the function units of contraction) (Davies et al., 2004).
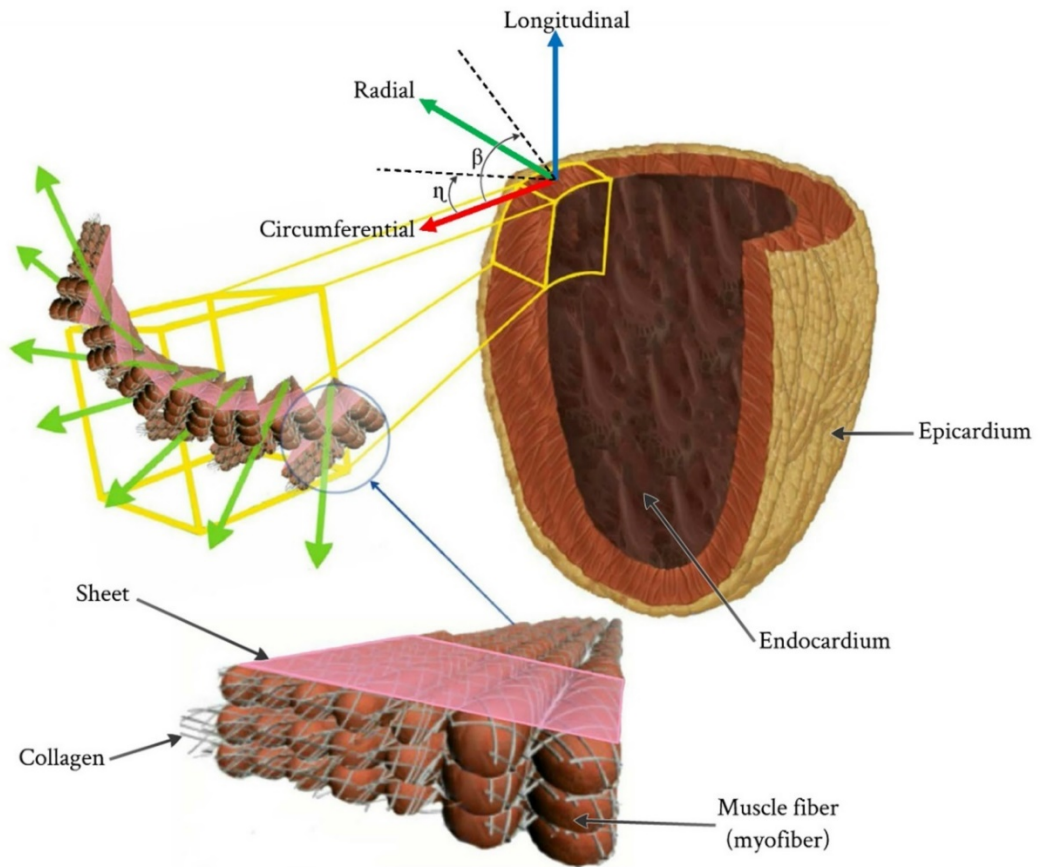
Figure 1.6: Schematic of fibrous sheet structure of cardiac tissue. The myocardium is composed of muscle fibers bound together by a mesh of collagen fibers
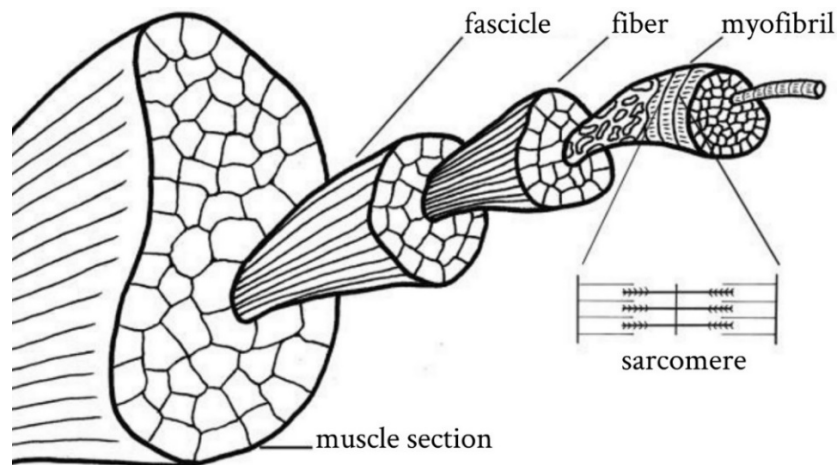
Figure 1.7: Step dissection of muscle tissue, showing a sample muscle section, fascicle, muscle fiber, myofibril, and sarcomere (Davies et al., 2004)

Thick filaments are made of hundreds of molecules of the protein myosin. At the molecular level, a thick filament is a shaft of myosin molecules arranged in a cylinder. Thin filaments are approximately half the diameter of thick filaments, and primarily contain the protein actin. The thin filaments look like two strands of pearls twisted around each other (Figure 1.8 and 1.9).
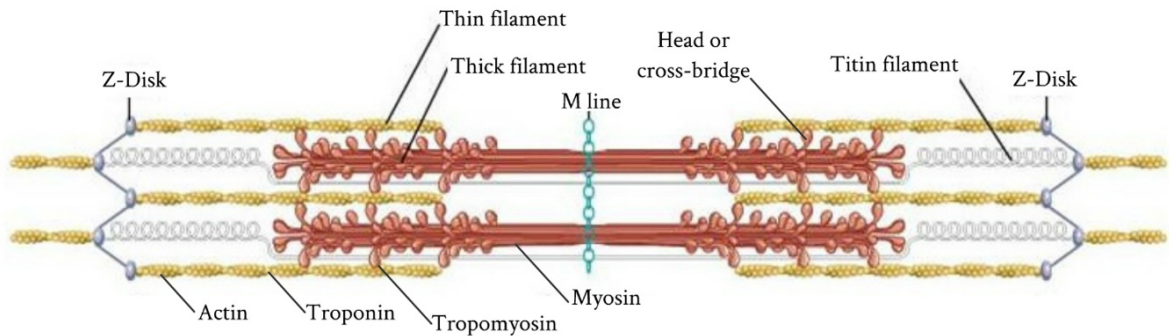
Figure 1.8: Real sarcomere (Sherwood, 2012)
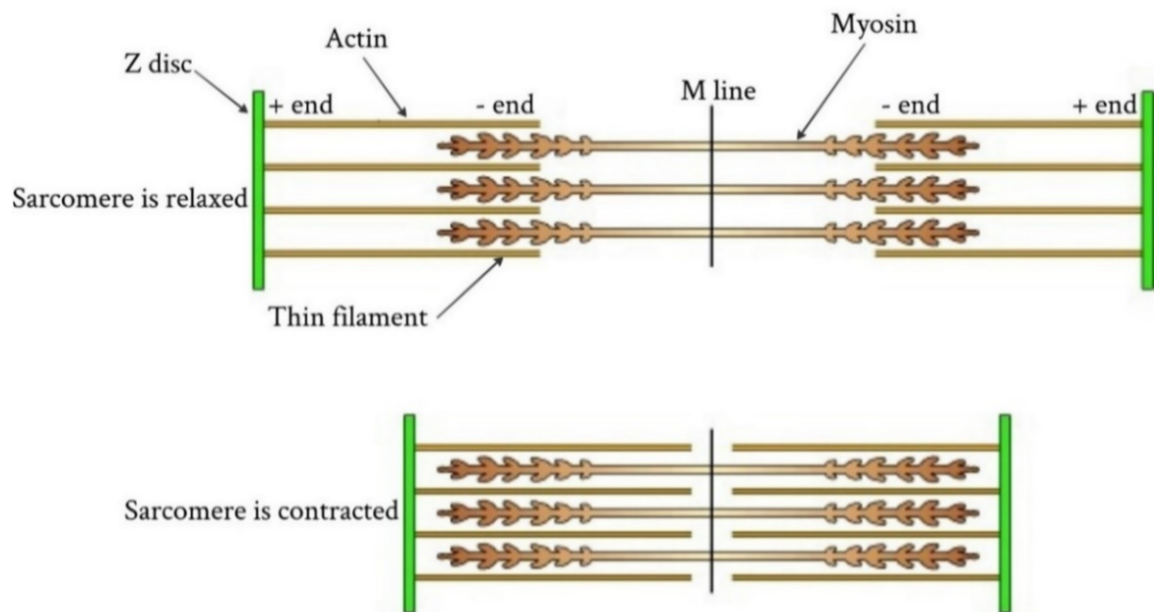
Figure 1.9: The sarcomere -- the contractile mechanism of muscle (Koeppen & Stanton, 2009)

In order for the muscle to contract, the thick and thin filaments must slide past each other, moving Z disks from either end of the sarcomere closer to each other. During this shortening of sarcomeres, there is no change in the length of either thick or thin filaments (Figure 1.8 and Figure 1.9). This is the sliding-filament mechanism of muscle contraction. A sarcomere shortens when myosin heads and thick filaments form a cross-bridge with actin molecules and thin filament. Cross-bridge formation is initiated when calcium ions released from the sarcoplasmic reticulum bind to troponin. This binding causes troponin to change shape (Figure 1.10). Tropomyosin moves away from the myosin binding sites on actin allowing the myosin head to bind to actin and form a cross-bridge. Also note that the myosin head must be activated before the cross-bridge cycle can begin. This occurs when adenosine triphosphate (ATP) binds to the myosin head and is hydrolyzed to adenosine diphosphate (ADP) and inorganic phosphate (P). The energy liberated from the hydrolysis of ATP activates the myosin head, forcing it into a cocked position (Clark, 2005; Plowman & Smith, 2013)
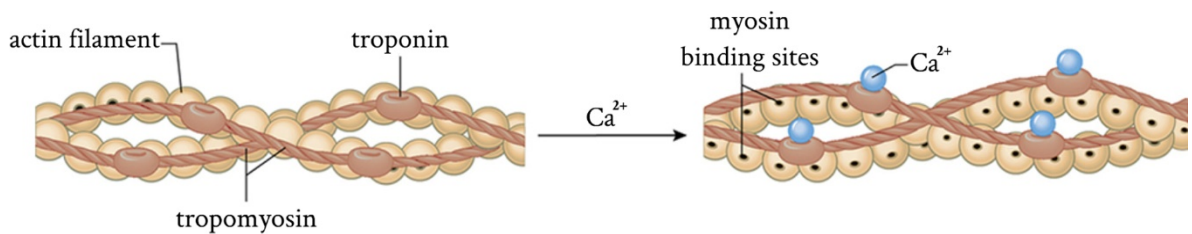
Figure 1.10: Troponin changes shape and pulls tropomyosin out of the myosin head binging sites (Widmaier, 2013)

Cross-bridge cycle may be divided into four steps (Figure 1.11):

1. Cross-bridge formation
2. The power stroke
3. Cross-bridge detachment
4. Reactivation of myosin head
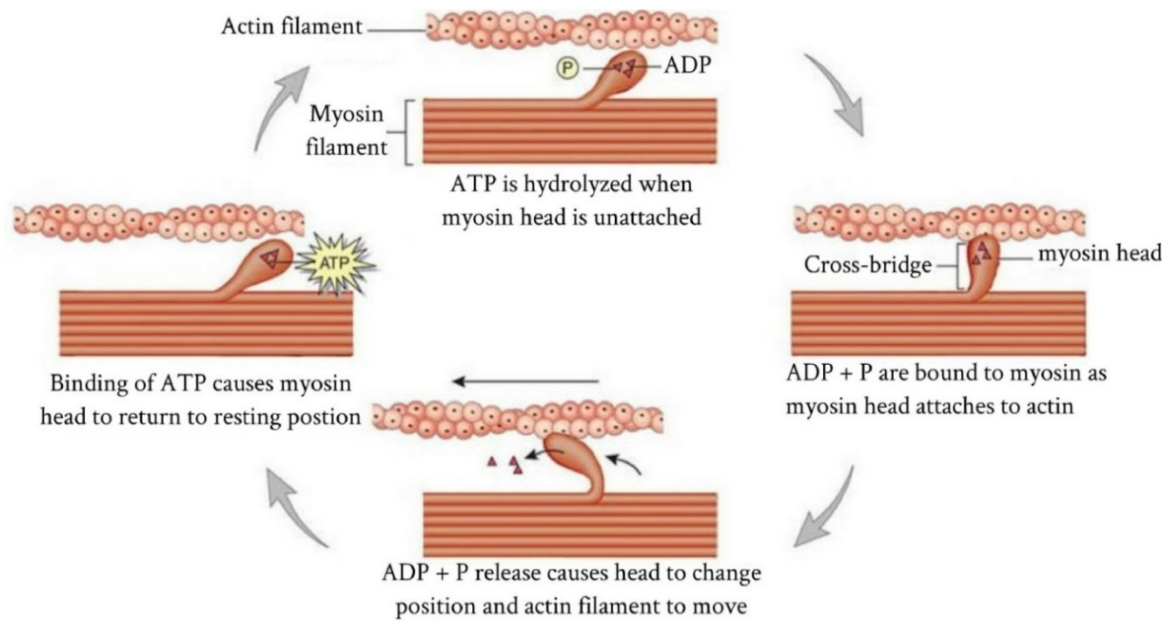
Figure 1.11: The cross-bridge cycle: how muscle fibers contract (Widmaier, 2013)

The first step in the cross-bridge cycle is the binding of the activated myosin head with actin, and releasing inorganic phosphate (P) to form a cross-bridge. The second step is the power stroke. In this phase, ATP is released and the activated myosin head pivots, sliding the thin filament toward the center of the sarcomere. The third step entails the dissociation of myosin and actin. When another ATP binds to the myosin head, the link between the myosin head and actin weakens and the myosin head detaches. The fourth step is the activation of the myosin head. During this step, ATP is hydrolyzed to ADP and inorganic phosphate (P). The energy released during hydrolysis reactivates the myosin head returning it to the cocked position (Chandler & Brown, 2008; Katz, 2011).

As long as the binding sites on actin remain exposed, the cross-bridge cycle will repeat; as the cycle repeats the thin filaments are pulled toward each other and the sarcomere shortens. This shortening causes the whole cardiac muscle to contract. The cross-bridge cycle ends when calcium ions are actively transported back into the sarcoplasmic reticulum. Troponin

returns to its original shape allowing tropomyosin to glide over and cover the myosin binding sites on actin (Sherwood, 2012).

1.5   Heart diseases

Heart disease is a broad term used to describe a wide range of diseases affecting the heart. Most people think there is only one reason for heart disease but in fact, there are several causes potentially affecting the function of the heart, with over 50 different types of heart disease. Some of the more common heart diseases are described below:

Coronary Artery Disease (CAD): CAD is the leading cause of mortality in the United States, accounting for more than 250,000 deaths annually (Bogaert et al., 2005; Rao & Thanikachalam, 2005). CAD occurs due to the narrowing of the coronary artery that supplies blood and oxygen to the heart muscle. As we get older, the lining of the heart artery gets damaged and thickened due to the accumulation of "plaque," which is a combination of fatty material, cholesterol, and other substances. This slow process is known as "Atherosclerosis" and can sometimes cause cracks or fissures in the coronary artery. Consequently, the blood cells called "Platelets" stack onto the damaged area and start the formation of blood clots that prevent blood flow to the heart muscle, which is necessary for survival (Figure 1.12). In an effort to compensate for the final functional myocytes, left ventricle remodeling may occur where the heart enlarges and expands along with increased thinning of the heart wall, causing adverse geometric and functional changes; if left untreated, this may lead to heart failure (Pfeffer & Braunwald, 1990; Sutton & Sharpe, 2000).
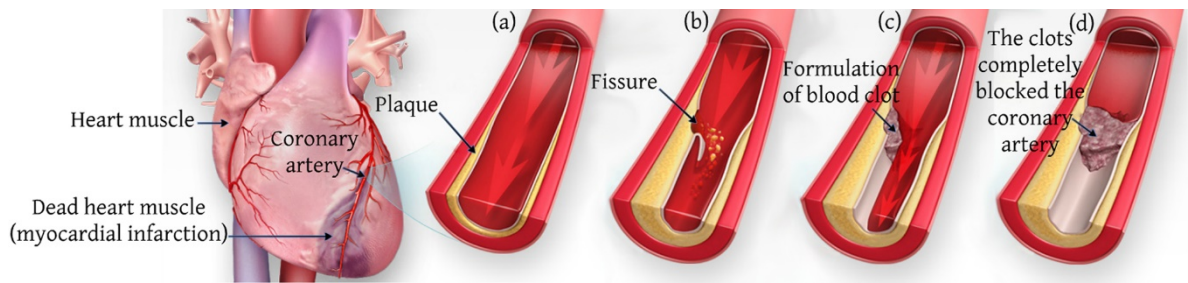
Figure 1.12: Progression of heart attack. (a) Plaque buildup in the walls of the coronary artery; (b) Plaque becomes unstable and ruptures; (c) Platelets stack on the damaged area and start forming blood clots; (d) Clot completely blocks the coronary artery resulting in the death of all muscle tissue below the blockage (American Heart Association, 2013)

Myocardial infarction (MI) and Ischemia: MI often entails myocardial cell death owing to a number of reasons. Most commonly, myocardial infarction occurs when normal blood flow to the heart decreases (Figure 1.12). Reduced blood flow usually results from a thrombus in the coronary artery (Gaasch et al., 1985; Anversa & Sonnenblick, 1990; Yusuf et al., 2004).

Hypertrophy (Hypertrophic Cardiomyopathy): This is when the chamber muscle tissue enlarges due to one of several different causes (Figure 1.13). The most common cause is high blood pressure, something that requires the heart muscle to work harder. As the workload increases, the chamber walls grow thicker, lose elasticity and may eventually fail to pump with as much force as that of a healthy heart (Alpert, 1971; Katholi & Couri, 2011).

Dilated (Congestive) Cardiomyopathy: A weakness in the heart walls causes them to enlarge (Figure 1.13). In some cases, it prevents the heart from relaxing and filling with blood as it should. Over time, it can affect the whole heart (Fuster et al., 1981; Wheeler et al., 2009).
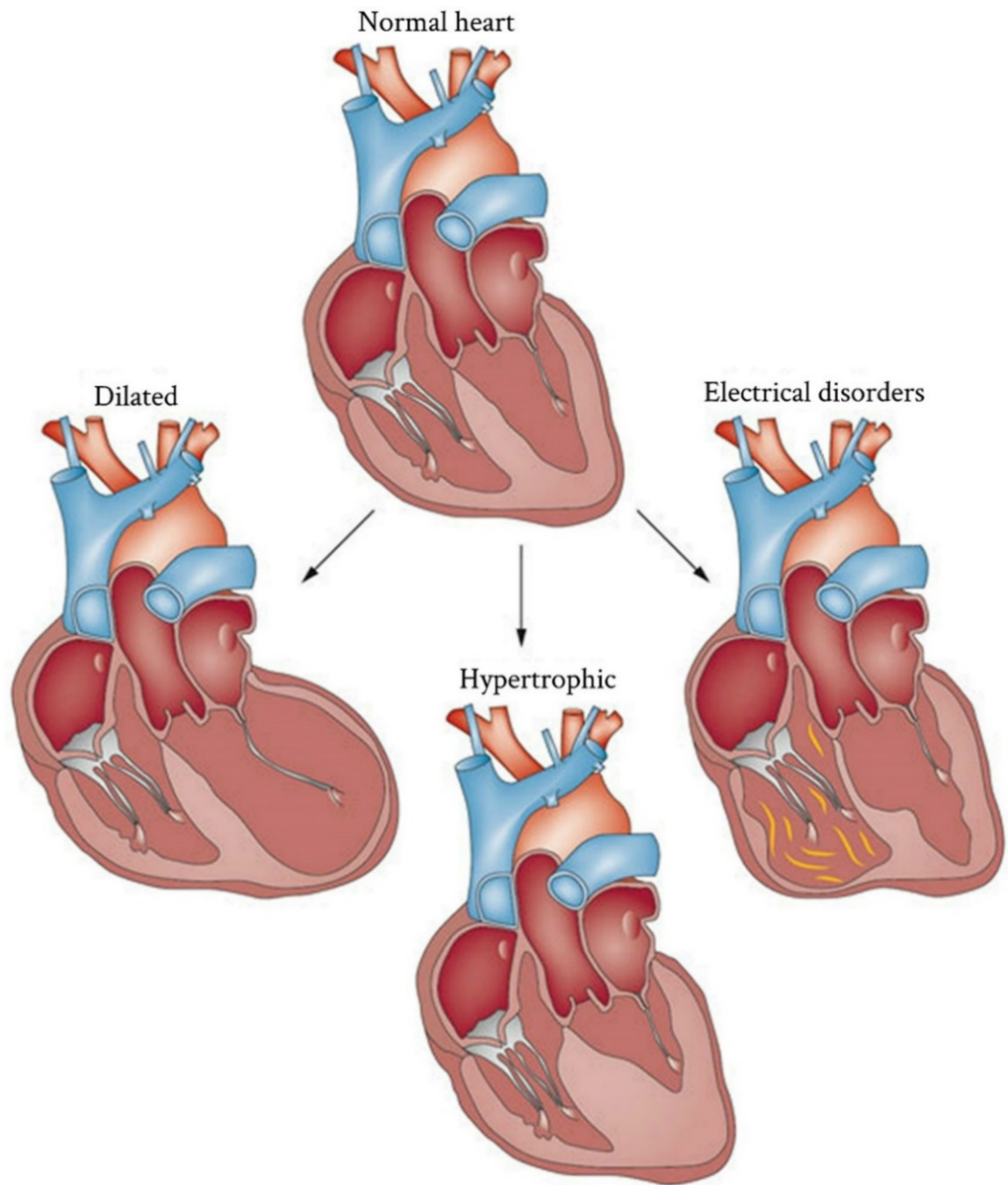
Figure 1.13: Illustration of the differences between a normal heart, hypertrophic cardiomyopathy, dilated cardiomyopathy, and with electrical disorders (arrhythmogenic right ventricular cardiomyopathy) (American Heart Association, 2013)

Electrical disorders: Include abnormal heart impulse rhythm and can be caused by problems with the heart's electrical system (Figure 1.13). The electrical impulses may happen too fast, too slowly, or erratically (tachycardia, bradycardia and arrhythmia) causing the heart to beat too fast, too slowly, or erratically (Farwell & Gollob, 2007).

Carditis: This condition entails heart tissue inflammation and it is categorized into three different disorders, depending on where the inflammation occurs (Figure 1.14). Endocarditis refers to inflammation of the heart's inner tissue layer (endocardium), myocarditis refers to inflammation of the heart muscle, and pericarditis refers to inflammation of the sac that holds the heart (pericardium) (Steere et al., 1980; Carter et al., 2004).

Valvular Disease: Damage occurs to one or more of the four cardiac valves, namely mitral, pulmonary, tricuspid, and aortic. The most common types of valve disease are valvular stenosis and valvular insufficiency (Bekeredjian & Grayburn, 2005; Henein, 2008). In valvular stenosis, the valve opening is smaller than normal due to stiff or fused leaflets, causing the heart to work very hard to pump the blood through it and thus causing heart failure (Figure 1.15). In valvular insufficiency, the valve is unable to close effectively, meaning that blood will be able to flow backwards. Both these conditions may lead to compensation by the heart chambers, which in turn could possibly lead to other conditions affecting the heart.

(a)

Pericardium surrounds heart

Pericardium cavity filled with fluid

Outer layer of pericardium (pulled back to show inner layer)

Two layers of pericardium

(b)

Inflamed and thickened layers of pericardium rub against each other and the heart
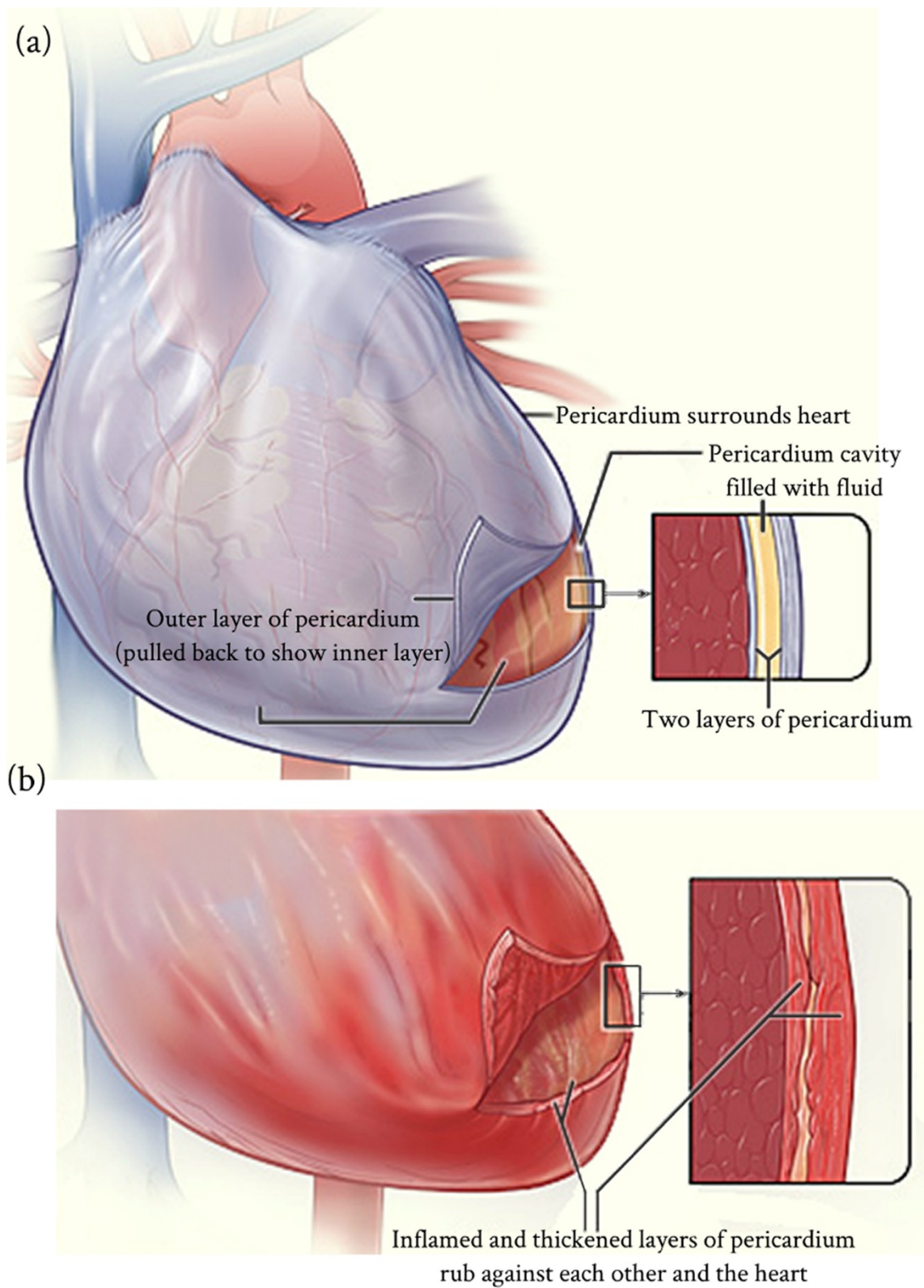
Figure 1.14: (a) Normal heart and pericardium; (b) Heart with pericarditis (inflamed pericardium) (Bonow et al., 2011)
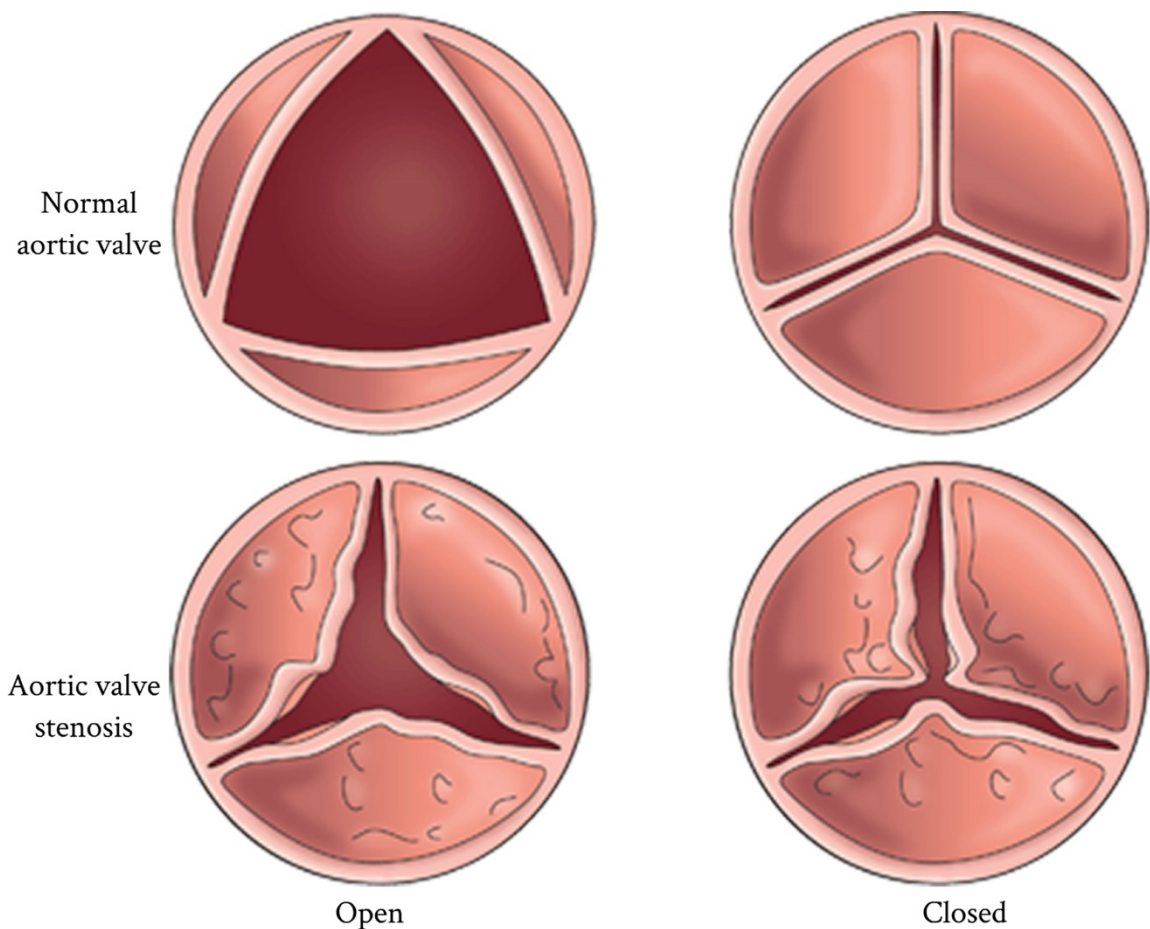
Figure 1.15: Aortic valve in normal and stenosis states (Otto & Bonow, 2013)

1.6 Myocardium bulk modulus

One of the tools with the potential to facilitate the early detection of human heart failure is to understand the mechanical behavior of the LV in normal and diseased states. Then there would be continuous interest in determining the material properties of the myocardium by mechanically testing excised strips from it. These strips, under prescribed homogeneous loading conditions, produce stress-strain relationships. These tests were originally done uniaxially, but more recently, biaxial tests have also been performed. A uniaxial test is used to define passive stress-strain relationships in the fiber's direction (Kohl et al., 2011). It is a very useful test in determining the general characteristics of the behavior of cardiac tissue in

both healthy and diseased states, but is not sufficient to provide a unique description of the myocardium's three-dimensional (3D) constitutive behavior. Due to the incompressibility of cardiac tissue, biaxial tests can be used to determine certain multidimensional stress-strain relationships for the fibers and cross-fibers (Fung & Cowin, 1994). Despite the frequent assumption that human myocardial tissue is incompressible, the fact remains that all myocardial tissue has some degree of compressibility. Furthermore, the subject on the compressibility of myocardium tissue is raised as a result of systolic intra- and extra-vascular blood displacements (Yin et al., 1996). Consequently, it is evident that myocardium tissue compressibility changes during the cardiac cycle.

The information embodied in the myocardial tissue bulk modulus adds further insight to the mechanical nature of the soft tissue. Bulk modulus is very important as a standalone parameter and as additional information to shear/Young's modulus. Precise myocardial bulk modulus values are especially required to improve the accuracy of finite element (FE) simulation for human heart modeling. In the last several decades, publications related to cardiac modeling have addressed the myocardial bulk modulus from many different perspectives. The published myocardial bulk modulus values recorded by researchers who were interested in simulating LV performance during the diastolic phase are quite small, for instance 28kPa (Bettendorff-Bakman et al., 2006) and 160kPa (Veress et al., 2005). This may be attributed to small changes in ventricular wall volume. Some studies evaluated the bulk modulus under the assumption that during the rapid filling phase, the volume change of the ventricular wall should be less than 10%. Additionally, relatively high bulk modulus values were used by researchers who analyzed the systolic phase, e.g., 380kPa (Shim et al., 2012), 600kPa (Dorri et al., 2006), and 25MPa (Marchesseau et al., 2012). High values for the bulk modulus during the systolic phase are due to the systolic intra- and extra-vascular

blood displacements that give rise to tissue compressibility. A mean, constant value for myocardial bulk modulus was assumed during each cardiac phase.

Despite the widespread use of uniaxial and biaxial tests for determining myocardial characteristics, there are four major problems that arise from these kinds of studies (Yettram & Beecham, 1998; Périé et al., 2013):

1. Tests were carried out on non-human tissue, and as a result may not be directly applicable to humans.

2. The properties may not be directly relevant to FE heart models due to the myocardium's heterogeneous behavior.

3. The myocardium's mechanical properties change drastically immediately after death.

4. There is variation in the mechanical property values according to experimental loading conditions.

All the above limitations prompt researchers to find alternate ways of running experiments, without having to excise samples from the myocardium. Hence, a group of researchers have moved toward using MRI and FE or mathematical methods to determine mechanical properties *in vivo* (Augenstein et al., 2006; Wang et al., 2009). Others have applied scanning acoustic microscopy with high frequency ultrasound to measure the bulk modulus and describe the mechanical properties of the myocardium (Dent et al., 2000). However, most bulk modulus experimental values obtained from these studies are very high ($\approx$ 3GPa) and cannot be used directly in FE modeling.

1.7   Problem statement

With heart disease being such a major health problem as well as a large financial strain on healthcare, it is no wonder that over recent years, cardiology has featured prominently as a medical research field. It is in the hopes of better understanding the functions of the heart and the effect diseases have, that research has continued. Greater knowledge may enable earlier disease detection and medical intervention at less advanced stages. Research may also pave the way towards more effective treatment.

The heart is extremely complicated in terms of its structure and function. It would be a grave mistake to model it purely from a mechanical point of view without an appreciation of its complex biological nature. Therefore, this research has aimed to model the behavior of the human heart muscle including an accurate description of both muscle fiber orientation and material properties.

For many years, researchers have attempted to determine the material properties of myocardium involving precise measurement of the ventricles of animals. Only a few have used data gathered from human subjects, since this data is usually hard to come by and is often severely limited in terms of quality and quantity. The research introduced a novel method to determine the material properties of beating human heart, and in particular the myocardial bulk modulus.

1.8   Study objectives

The first main objective of this research is to develop a 3D model of the LV, which is the main pumping chamber and most common site for heart disease, based on an accurate description of both muscle fiber orientation and material characteristics. The proposed model is used to study the effects of myocardial fiber architecture on LV mechanics.

The second objective, and to overcome the above shortcomings in determining live tissue properties, an inverse FE procedure using the ANSYS® computer code approach is suggested to determine, *in vivo,* the myocardial tissue bulk modulus during the cardiac cycle. The proposed inverse technique is based on published, experimentally measured LV pressure-volume curves. By using published LV experimental data as output, the bulk modulus versus time curve is traced with an inverse technique. The recurring changes of myocardial tissue bulk modulus in the LV wall during a cardiac cycle result in a highly efficient global function of the normal heart. Therefore, the myocardial bulk modulus can be effectively used as a diagnostic tool of heart ejection fraction.

1.9   Thesis outline

The first chapter of this dissertation concerns the physiology and architecture of the heart. Basic concepts of the heart's anatomy and functions are initially presented. Then the cardiac cycle, myocardial contraction process, and heart diseases are outlined.

In order to understand the evolution of the ventricle mechanics model developed in the dissertation, a brief history of cardiac modeling research is presented in chapter two. Ventricle model development has ranged from thin walled to thick walled and FE models. Moreover, the mechanical behavior of cardiac tissue is modeled using a variety of material response functions, from a simple phenomenological description to a biophysical representation based on the microscopic myocardial architecture. Following some historical remarks, the aim of the present work and study plan are presented.

In chapter three, the heart tissue is studied from a continuum mechanics point of view. Selected elements of continuum mechanics are outlined. The approach for LV motion formulation and material behavior of the myocardium tissue are discussed.

The implementation of an FE model of the LV is shown in chapter four. To this end, a thick-walled ellipsoid truncated at two-thirds of the major axis is chosen for modeling a human LV. Appropriate boundary conditions are also imposed, and the constitutive behavior including detailed information about fiber orientation patterns is prescribed. A new approach using a direct FE method of studying the effect of myocardial fiber architecture on LV mechanics is presented. Moreover, a novel approach using the inverse FE method to determine, in *vivo*, the myocardial bulk modulus during a cardiac cycle is introduced. This chapter plays a central role in the dissertation; however, since the procedures are based on a simplified geometry, there is still margin for improvement with respect to accuracy and completeness of fiber orientation and material properties. At the end of this chapter, the merits and limitation of the proposed FE model are discussed.

The results of FE implementation are discussed in chapter five. In particular, the sensitivity of LV mechanics, such as mesh density, myofiber volume fraction, myofiber orientation, and different constitutive models is presented using the direct FE method. Besides, determining the human myocardial bulk modulus and the correlation between LV repolarization and myocardium tissue compressibility are described using the inverse FE method. A balanced discussion taking into account work from other groups is provided in chapter six.

Finally, based on the results and discussion presented in chapters five and six, the conclusions and recommendations are drawn in chapter seven.

CHAPTER 2:REVIEW OF CARDIAC MODELING RESEARCH

2.1   Introduction

The heart has always been recognized as the most important organ in the body. Even at the beginnings of human civilization, the heart was considered by many cultures to contain magical powers and often symbolized life itself. It is therefore hardly surprising that there has been a great deal of interest in its structure and function. Even with all the technological advances from different aspects, it remains impossible to understand the heart completely. This is not due to a lack of quality research but owing to the complexity of the heart. Simplified models can be useful to aid comprehend the behavior of the heart, to identify the symptoms of heart failure and be able to study quantities that cannot be measured clinically or in experimental settings, such as mechanical stress through the heart wall.

Cardiac research started in the days of early anatomists. In the 15th century, Leonardo Da Vinci, whose Mona Lisa painting is the most famous in the world, described the movement of the heart wall by using metal pins implanted through an animal's chest wall (Keele, 1951). This was an early attempt at describing and understanding the heart's movement, in a limited way. Now with advancements in instruments, heart muscle properties can be precisely measured to provide the necessary information and comprehend the heart's behavior.

2.2   The development of thin walled models

(Woods, 1892) made the first attempt to create a mathematical model of the LV using Laplace's law for the evolution of wall tension in the heart. This model approximates myocardial tension to be proportional to the product of pressure and radius. Sixty years later by (Burch et al., 1952), who employed a spherical model to study the effects of various pressures and ventricular volumes on ventricle performance, as well as the effects of the

structural arrangement of muscular fibers and manner of contraction. Five years later (Burton, 1957) demonstrated via Laplace's law the importance of ventricle size and shape on its performance. Assuming an ellipsoidal geometry, this type of analysis was refined by (Sandler & Dodge, 1963), who investigated the role of ventricular pressure, volume and shape in determining stress and tension within the LV wall during the cardiac cycle. These forces were calculated by using Laplace's law LV dimensions, as determined from biplane angiocardiograms in human subjects with heart disease. A number of other authors utilized this model to analyze human and animal patient data. (Wong & Rautaharju, 1968) and (Ghista & Sandler, 1969) developed thick shell theories. Their analyses yielded nonlinear stress distributions through the wall thickness, but it was not possible for Laplace's law to predict results. However, their assumptions with regard to the LV's deformation behavior are restricted. In addition, in the development of Laplace's law their theories neglected the effect of transverse normal stress (radial stress) and transverse shear deformation, which are significant for the LV. (Mirsky, 1969) presented a system of different equations for the stress equilibrium in the LV wall assuming an ellipsoidal geometry. His analysis of the stresses in the ventricular wall indicates that maximum stresses occur at the inner layers and decrease to a minimum at the epicardial surface -- a result partially validated experimentally.

2.3 The development of thick walled models

(Wong & Rautaharju, 1968) developed a formula that allows stress distribution calculations for either a spherical thick shell, or an ellipsoidal shell, or a paraboloid of revolution. Their analyses overcame the shortcomings of Laplace's formula for a thin wall, which is an ill-defined and practically meaningless quantity in a structure like the human LV. The formula can be used for any of three configurations by varying certain parameters according to known

or assumed heart dimensions. This model is similar to that previously used by (Sandler & Dodge, 1963), except that the stresses are allowed to vary through the wall's thickness.

Despite inclusion in earlier models, bending and shear were still mostly not included. (Streeter et al., 1970) proposed an analysis of stress in the LV wall based on the realistic assumption that the myocardium is essentially composed of fiber elements that carry only axial tension and vary in orientation through the wall. The geometry based on that obtained from ten dogs rapidly fixed in *situ* at the end of diastole and end of systole.

(Ghista & Sandler, 1970) developed a simple model to predict the oxygen consumption rate of a healthy LV. The geometry of this model was obtained by cineangiocardiography and the LV chamber pressure was obtained by means of fluid-filled catheters subsequent to retrograde or transeptal catheterization.

(Wong, 1973) produced a thick-walled ellipsoidal shell with non-uniform wall thickness LV model. This model served to compute the sarcomere lengths at various wall layers during the diastole. This method gives passive and active fiber tension as separate quantities within each fiber and is used to analyze isovolumetric contraction, which assumes the myocardium is homogenous, isotropic and viscoelastic. The fiber orientations obtained from (Streeter Jr et al., 1969) and myocardium were modeled using Hill's model and Huxley's sliding filament theory (Hill, 1938; Haselgrove & Huxley, 1973).

(Tözeren, 1983) came up with a cylindrical model of LV to estimate the local stresses and deformations that occur during the cardiac cycle. The LV presented as thick hollow tube composed of solid fibers embedded in an inviscid fluid matrix. It was concluded that wall thickness and fiber orientation distribution hardly affect the pressure-volume relation in the

diastole. In the systole, the pumping efficiency was shown to increase with increasing thickness of the modeled LV and with increasing contractility of the heart muscle fibers.

(Phillips & Petrofsky, 1984) calculated the active systolic elastic moduli for the circumferential and longitudinal LV axes by using contractile filament stress and fiber strain. Compressive strains were introduced into the model, which generated the fiber stresses. These stresses and strains then helped calculate the active systolic elastic moduli for the circumferential and longitudinal LV axes. These material property parameters were determined at four points during cardiac systole. The data obtained from thirty-nine patients with various pathological conditions was evaluated using pressure and volume data acquired from single-plane cineangiography. The results indicate that the active moduli exponentially decrease during cardiac systole.

(Kim et al., 1985) developed a mathematical method of estimating the local epicardial deformation, wall thickness, and regional circumferential and longitudinal wall stress using biplane coronary cineangiography for four dogs and a normal patient. In this method, the motion images of the coronary artery bifurcation points were the local markers and the accuracy of using these was compared with the more invasive method of using implanted lead beads. The estimation results validate this analysis compared to the experimental results based on the implanted lead beads. The main advantages of this method are that it can evaluate the wall stress and wall deformation together with blood vessel conditions and it is far safer than implanting lead beads.

2.4   The development of finite element models

(Janz & Grimm, 1972) were the first group of researchers who attempted to create an FE model to analyze the mechanical behavior of a rat heart LV. The ventricle was modeled as a

heterogeneous, linearly elastic, thick-walled solid of revolution. The geometric data applied was obtained from heart cross-sections of adult Sprague-Dawley albino male rats.

(Hamid & Ghista, 1974) developed an FE model of the LV to predict the stresses through the wall chamber and aortic valve. The element type utilized in this model was developed by (Zienkiewicz, 1971). The 20-noded isoparametric brick element is ideally suited for LV modeling. The model geometry was obtained by cineangiocardiographic imaging at mid-ejection.

(Nikravesh et al., 1981) developed a new FE model that obtains much better reconstructions than offered by single or even bi-plane cineangiography. Besides, this method adds wall thickness, something partially lacking in cineangiography. However, FE reconstructions indicate that no analysis was performed on the FE meshes obtained.

(Yettram et al., 1983) presented an FE model to study the effect of myocardial fiber architecture on the behavior of the human LV during diastole. The myocardium has a complex anisotropic fiber structure. Variations were made to both fiber orientation and the ratio of elastic moduli along and across the fibers. The results signify that at least in diastole, when the LV is considered to be a passive structure under the action of internal blood pressure, the effect of the real fiber arrangement is generally a reduction of deformation as well as direct stresses. In spite of fiber angle changes across the wall, the analyses correctly predicted the lack of LV rotation about the long axis.

(Horowitz et al., 1986) introduced an FE technique for simulating an entire cardiac cycle. Time-sequential canine heart data obtained by dynamic computerized tomography served to initiate the simulation as well as to provide real data for result evaluation. The model had two element types: the "Truss" element to simulate the anisotropic nature of the myocardium

with varying fiber angles, and a basic 20-noded isoparametric brick element to form the basic structure. The simulation allowed for the evaluation of time-varying stress and strain distributions in the ventricle wall and active forces prevailing in the myocardial fibers.

(McPherson et al., 1987) developed a type of LV geometry FE analysis using 3D echocardiographic reconstructions to study the effect of acute myocardial ischemia on the myocardial elastic modulus. The data was collected from six open-chest dogs before and after coronary occlusion using the data acquisition and reconstruction method proposed by (Nikravesh et al., 1981). In the FE analysis after coronary occlusion, two analyses were performed: one utilizing the control elastic modulus for all LV segments and one in which ischemic (dyskinetic) segments were assigned a higher elastic modulus. It was concluded that the myocardial diastolic elastic modulus was increased by ischemia and this approach may facilitate the clinical assessment of intrinsic muscle stiffness.

(Bovendeerd et al., 1991) proposed another FE model of the LV based on the same geometric data as (Huyghe et al., 1991). This model was meant to study the mechanics of the ischemic LV during the cardiac cycle. The muscle fiber stiffness was assumed twice that in the fiber direction than in the cross-fiber direction. The results show that global deformation was asymmetric with respect to the ischemic region. It was deduced that the ischemic LV pressure was about 12% lower, the ejection volume was 20% lower and aortic flow reduced compared to a simulation without ischemic LV pressure.

(Fann et al., 1991) evaluated 2D subepicardial and subendocardial deformations in the LV's anterior, lateral, and posterior regions in a closed-chest, conscious dog heart. Eight dogs underwent the placement of 22 radiopaque markers into in the LV myocardium. These were located at the anterior, lateral and posterior subepicardial and subendocardial, mid-ventricle level. Eight hours later, biplane videofluoroscopy was performed. It appeared that

circumferential shortening occurred in all layers and regions; similarly, longitudinal shortening occurred in all layers except that of the posterior endocardium.

(Bovendeerd et al., 1992) investigated the dependence of local LV wall mechanics on myocardial muscle fiber orientation using an FE model described by (Huyghe et al., 1991). They considered an anisotropic model with the active and passive components of myocardial tissue, dependence of active stress on time, strain and strain rate, activation sequence of the LV wall and aortic afterload. The muscle fiber angle distribution through the myocardium varied in order to make the active muscle stress homogeneous throughout the myocardium layers. The muscle fiber angle is defined as the angle between the muscle fiber direction and local circumferential direction, otherwise known as the helix angle. The transmural variation of the helix angle assumed was from +60˚ at the endocardium through to 0˚ in the mid-wall layers to -60˚ at the epicardium. The active muscle fiber stresses at the equatorial region were 110 kPa, 30 kPa and 40 kPa in the respective myocardium layers from the endocardium to the epicardium. It was concluded that the distribution of active muscle fiber stress and muscle fiber strain across the LV wall is very sensitive to transmural distribution of the helix fiber angle. However, the problem with this approach is that no consideration is give to the effect that geometry may play on stress distribution. The LV is never stress-free, so there are stress changes and no absolute stresses are implied.

(Hashima et al., 1993) developed a new means of studying the non-uniform mechanical function that occurs in normal and ischemic ventricle myocardium. An array of 25 lead markers was sewn onto the epicardium of the LV's anterior free wall in an open-chest, anesthetized canine preparation. Bi-plane cineangiography was used to track the position of the markers before and during induced ischaemia. The strains during the cardiac cycle were

calculated using marker triplets. Large stain gradients were observed across the infarct regions.

Subsequently, (Bovendeerd et al., 1994) investigated the influence of fiber direction variations on the distribution of stress and strain in the LV wall using an FE model described by (Huyghe et al., 1991) to simulate LV mechanics. An additional angle to helix fiber angle, the transverse fiber angle, was employed to model the continuous course of the muscle fibers between the inner and outer layers of the ventricle wall. This angle is defined as the angle between the circumferential direction and fiber path projection onto the plane perpendicular to the local longitudinal direction, whereas the helix fiber angle is defined as the angle between the local circumferential direction and fiber path projection onto the plane perpendicular to the local radial direction. Three model runs were carried out: the first run had the transverse fiber angle always at zero and the helix fiber angle at -60º at the epicardium, 0º at the mid-wall and +60º at the endocardium. The second run had the same angles except the helix fiber angle at the mid-wall was +15º. The third run had the same angles as the second except the transverse fiber angle was at a maximum at the mid-wall and zero at the endocardium and epicardium. It was found that the changes in fiber orientation hardly affected the pressure-volume relation of the LV but significantly affected the spatial distribution of the local ventricle wall stresses and strains.

(Van Campen et al., 1994) compared the two-phase axisymmetric porous medium non-linear FE model by (Huyghe et al., 1991) with the 3D-FE model by (Bovendeerd et al., 1994), and predicted outcome from canine experiments. In the axisymmetric porous medium non-linear FE model, the two-phase approach led to transmural/intramural intramyocardial pressure gradients, which was qualitatively consistent with experimental data. This model also qualitatively correctly predicted myocardium stiffening due to an increase in intracoronary

blood volume. Finally, the quasi-linear viscoelasticity approach led to the experimentally observed effects of hysteresis in the pressure-volume curve and of residual stress. The 3D model by (Bovendeerd et al., 1994) shows that regional distributions of local ventricle wall stresses are very sensitive to the spatial distribution of muscle fiber orientation. On the other hand, the change in LV pressure and aortic flow is hardly affected by a change in the spatial distributions of helix and transverse fiber angles. Important aspects of the mechanics of a beating LV are predicted by this model; the influence of muscle fiber orientation on ventricle mechanics, redistribution of intracoronary blood in the ventricle wall during the cardiac cycle, viscoelastic behavior of myocardial tissue, and regional decrease of myocardial perfusion, result in the formation of an ischemic region.

(Taber et al., 1996) explored the effects of various anatomical and mechanical features on the torsion behavior of the LV. They used two theoretical models to study the mechanics of this phenomenon: a compressible cylinder and an incompressible ellipsoid of revolution. The analyses of both models account for large-strain passive and active material behavior, with a muscle fiber angle that varies linearly from endocardium to epicardium. A comparison of theoretical and published experimental results by (Beyar et al., 1989) for a normal LV showed qualitative agreement in the dynamic pattern of torsion during the cardiac cycle. The models indicated that relative to the end of diastole, the peak twist occurs near the end of the diastole and depends on myocardial compressibility, muscle fiber angle, contractility, and ventricle geometry. It is also worth noting that twist increases with increasing compressibility, contractility, and ventricle wall thickness, while it decreases with increasing cavity volume.

(Schmid et al., 1997) developed an FE method for the human left and right ventricles to study the anisotropic structure of the myocardium. Magnetic Resonant Imaging (MRI)

produced the geometry of a human heart while the anisotropic structure of the myocardium had two basic sources: first, a common band-like structure of both ventricles introduced a global anisotropy, and second, the muscle fiber arrangement within the band caused intrinsic local anisotropy. According to the results, the variation in muscle fiber arrangement affected the global cardiac performance.

(Yettram & Beecham, 1998) described a computer method for determining a long-fiber to cross-fiber elastic modulus ratio in ventricle myocardium by using an FE model and matching cavity volume and ventricle length against valves derived from cineangiographic and pressure data. The results obtained in the work show that using FE modeling has at least the potential to determine overall transversely isotropic mechanical properties of the heart's LV myocardium.

(Usyk et al., 2000) proposed 3D FE model to investigate the effect of laminar orthotropic myofiber architecture on regional stress and strain in a canine LV at the end of diastole and end of systole. The geometry of the canine LV was represented by a truncated ellipsoid of revolution. The focus, inner and outer surface dimensions of the LV wall were calculated from experimental data. The results indicated that the passive material changes had little effect on systolic LV strains. Incorporating a significant component of active stress transverse to the muscle fibers greatly improved the agreement between measured and modeled transverse end-systolic shear strains.

(LeGrice et al., 2001) described a computer model (Auckland heart model) for a detailed and realistic representation of important ventricular anatomy aspects. The model is based on an extensive anatomic dataset collected systematically by the researchers and others over more than a decade. It includes preliminary descriptions of the Purkinje fiber network, coronary vessels and collagen organization. A number of research groups on integrative studies of

cardiac electrical and mechanical functions have used this model. However, the model is limited in important ways. One pertains to the geometry and muscular architecture of the atrial chambers, the second is the distribution and characteristics of the transmural penetration of Purkinje fibers, and finally, the coronary circulation architecture within the myocardium.

(Kerckhoffs et al., 2003) provided new insight into the interpretation of cardiac deformation towards various forms of cardiac pathology by using a 3D FE model of an LV. Myocardium material was considered anisotropic, nonlinearly elastic and time dependent. They assumed that the delay between depolarization and the onset of crossbridge formation was the same for all myofibers. The simulation results showed that the LV mechanics with unphysiological synchronous depolarization myofiber strain were more homogeneous and more physiologic. It was found that the delay between depolarization and onset of crossbridge formation is distributed such that contraction is more synchronous than depolarization. It should be noted that the variations in depolarization timing caused larger relative changes in the distribution of myofiber strain than for myofiber stress.

(Smaill et al., 2004) developed an FE model of a ventricle to study normal electrical activation and re-entrant arrhythmia. The model was based on the actual 3D microstructure of a transmural LV segment and can predict that cleavage planes between muscle layers may give rise to non-uniform, anisotropic electrical propagation and also provide a substrate for myocardial bulk resetting during defibrillation. The results indicate that the spread of electrical activation from an ectopic stimulus is slow in the direction perpendicular to cleavage planes, and this could contribute to the formation of macroscopic re-entrant electrical circuits, particularly in an ischemic heart. It was concluded that the structure

discontinuities in the ventricle's myocardium might play a role in the initiation of re-entrant arrhythmia and future studies that address this hypothesis should be carried out.

(Xia et al., 2005) analyzed the cardiac ventricle wall motion based on a 3D electromechanical biventricular model with realistic geometric shape and fiber structure, which couples the electrical and mechanical properties of the heart. They concluded that the inclusion of heart motion in the model had a significant effect on the simulation electrocardiogram (ECG) signal, particularly in the ST segment and T-wave regions. The simulation results are in good accord with results obtained from the Magnetic Resonant Tagging (MRT) technique. The study suggests that the electromechanical biventricular model might be a useful tool to assess the mechanical function of two ventricles and to study body surface potential in a more realistic way.

(Bettendorff-Bakman et al., 2006) developed a 3D FE model of the human left and right ventricles using realistic geometry and taking into account the nonlinear mechanical tissue. They investigated to what extent ventricular pressure causes the rapid and large increase of internal volume of both ventricles that occurs during the rapid filling phase in a healthy human heart. They also analyzed the influence of cardiac tissue viscoelasticity on the mechanical behavior of the heart during the first third of the passive diastole. The results were compared with the filling phase of the human LV as extrapolated from measurements by (Nonogi et al., 1988). In conclusion, the ventricle pressure measured during rapid filling could not be the sole cause of the rise in observed ventricle volume, while the influence of tissue viscoelasticity should not be disregarded in ventricle mechanics under normal physiological conditions.

In 2006, (Dorri et al., 2006)proposed an FE method based on realistic geometry obtained from MRI to simulate the 3D deformations of human LV myocardium due to contractile

fiber forces at the end of systole. The model was considered anisotropic and the fiber structure of the myocardial tissue was included in the form of a fiber orientation vector field, as reconstructed from the measured fiber trajectories in a postmortem human heart. The contraction was modeled by an additive second Piola-Kirchhoff active stress tensor. In this study, the researchers attempted to determine an LV deformation pattern by inverting the modeling process, i.e. extrapolating stresses from deformations rather than determining deformations from assumed fiber stresses. The results signify that the principal and normal strains are in good agreement with MRI measurements. It was concluded that systolic deformation measurement might provide useful diagnostic information.

In the same year, (Ubbink et al., 2006) investigated to what extent strain computed with a 3D FE model by (Kerckhoffs et al., 2003) matched strain determined experimentally. Discrepancies between the model-computed and experimentally measured deformation of a healthy LV wall are related to the choice of myofiber orientation in the model. Finally, they compared myocardial wall strain measured in three healthy subjects using MRT. Wall strain was computed with the model for various settings of myofiber orientation. They deduced that the presented FE model could accurately simulate circumferential strain, but failed to accurately simulate circumferential-radial shear strain. The time course of circumferential-radial shear strain seemed very sensitive to the choice of myofiber orientation, in particular to the choice of transverse angle. It is worth mentioning that the discrepancies between circumferential-radial shear strain in the model and experiment significantly reduced when the transverse angle increased by 25%.

(Bettendorff-Bakman et al., 2008) presented two models to study the mechanism of ventricular aspiration during the rapid filling phase. The first was an FE model of the two human ventricles, derived from MRI measurements taken at the end of systole in a healthy

human individual; the second was an ellipsoidal FE model of the LV. The internal volume of both models for the left and right ventricles was about 50 ml. This study was performed under the assumption of linear elasticity allowing for large deformations and taking into account the effective compressibility of the myocardium due to intramural fluid flow. The myocardium was assumed to behave like a homogenous, isotropic material and it was claimed that anisotropy is not considered of decisive importance based on a previous publication by (Bovendeerd et al., 1994) and (Vetter & McCulloch, 2000). The results were compared with measurements by (Nonogi et al., 1988) relating to the rapid filling phase of the human LV. Apparently, ventricular aspiration plays a key role in the ventricle filling process under normal physiological conditions.

(Niederer & Smith, 2009) developed a multi-scale biophysical electro-mechanics model of a rat LV. They integrated a wide range of experimental data into a common and consistent modeling framework to investigate how feedback loops regulate heart contraction. The results showed that the length-dependent Ca_{50} and filament overlap, which makes up the Frank-Starling Law, seemed to be the dominant regulators of efficient work transduction. Analyzing the fiber velocity field in the absence of the Frank-Starling mechanisms showed that the decreased efficiency in the transduction of work in the absence of filament overlap effects was caused by increased post systolic shortening, whereas the decreased efficiency in the absence of length-dependent Ca_{50} was caused by an inversion in the regional strain distribution. Finally, it was concluded that the feedback from muscle length on tension generation at the cellular level is an important control mechanism of the efficiency with which the heart muscle contracts at whole organ level.

(Göktepe & Kuhl, 2010) presented a fully implicit, entirely FE-based approach to the strongly coupled non-linear problem of cardiac electro-mechanics. The intrinsic coupling

arises from both the excitation-induced contraction of cardiac cells and the deformation-induced generation of current due to the opening of ion channels. The suggested unified algorithmic formulation was thoroughly set out with complete particulars of the weak formulation, consistent linearization, and discretization. It was concluded that the inherent anisotropic microstructure of cardiac tissue is reflected in the model by means of the modern notions of coordinate-free representation of anisotropy in terms of structural tensors. This concerns not only the passive and active non-linear stress response but also the deformation-dependent conduction tensor.

(Göktepe et al., 2011) developed a 3D FE biventricular heart method to simulate the passive response of myocardium tissue, particularly when coupled with active cardiomyocytes contraction and electric excitation. The myocardium was assumed as a convex model and anisotropic hyperelastic material that accounts for the local orthotropic microstructure of cardiac muscle. The parameters employed in the numerical analysis were identified by solving an optimization problem based on six simple shear experiments on explanted cardiac tissue. Important features were combined in this model, such that it is not based on the individual Green Lagrange strain tensor components, but is entirely invariant-based. The model is not only isotropic, but also fully orthotropic, and it is characterized in terms of only eight parameters that provide a clear physical interpretation.

(Bagnoli et al., 2011) developed an FE model of the human LV to analyze the twisting behavior of cardiac and investigate the influence of various biomechanical parameters on cardiac kinematics. The model was a thick-walled ellipsoid composed of nine concentric layers with internal volume of about 43ml. The myocardium was assumed to be linear-elastic isotropic, embedded in incompressible liquid with arrays of reinforcement bars oriented to reproduce the globally anisotropic behavior of cardiac tissue. The ventricle model was

combined with simple lumped-parameter hydraulic circuits reproducing preload and afterload. The simulation results were in good agreement with experimental data and confirmed the importance of symmetric transmural patterns for fiber orientation.

(Wang et al., 2012) developed a realistic 3D FE model of the human LV derived from non-invasive imaging data to investigate this model's sensitivity to small changes in constitutive parameters and changes in fiber distribution during the diastole phase. They also made comparisons between their model and similar models with experimental data, and demonstrated qualitative and quantitative differences in stress and strain distributions. In the framework of (Holzapfel & Ogden, 2009), the LV myocardium was treated as an inhomogeneous, thick-walled, nonlinearly elastic, incompressible material with fiber-reinforced myocardium tissue microstructure by expressing the strain-energy functional using fiber-based material invariants. In the incompressible case, their strain-energy functional had eight material parameters with relatively physical meanings. By employing three independently developed sets of constitutive parameters, it was found that the structure-based constitutive law employed here is relatively insensitive to small parameterization errors. The end-diastolic pressure-volume relationship of the model prediction was in good agreement with experimental data derived from human hearts. It was also found that changes in sheet orientation had relatively little impact on the model results, whereas changes in fiber angle distribution dramatically altered the stress and strain distributions. This highlights the importance of using a realistic fiber structure, especially in pathological conditions that involve pathophysiological remodeling of fiber orientation. It should be noted that a large difference was observed in the stress and strain predictions generated by the different constitutive models, even in cases in which the material parameters were fitted to the same experimental data.

An excellent introduction and more comprehensive reviews on FE-based research can be found in works by (Vinson, 1977), (Grewal, 1988), (Beecham, 1997), and (Zhong et al., 2012).

2.5   Aim of the present work

The aim of the present work is to create and develop a 3D FE model of the human LV that provides realistic descriptions of both muscle fiber orientation and material characteristics based on experimental data documented in literature. This model was used to study the sensitivity of LV mechanics and determine the bulk modulus (k) of human myocardium. The virtual model can help medical students understand the sensitivity of cardiac parameters on human LV function and measure quantities that can otherwise not be measured in clinical or experimental setting.

2.6   Study plan

It is clear that the heart is extremely complicated in terms of structure and function. It would be a grave mistake to model it purely from a mechanical point of view without some appreciation of its complex biological nature. For this reason, the key objective of this study plan is to develop an efficient, robust, modular, and unified FE approach to accurately describe the LV myocardium.

For many years, researchers have attempted to analyze and quantify the behavior of the human heart, and particularly the left ventricle (LV). Some have worked with a simplified geometry of LV, spheres, ellipses of revolution and general ellipsoids using a theoretical approach. Others have done experimental work involving precise measurements of animal ventricles, most commonly of dogs or pigs. Only a few have used data gathered from human subjects since this sort of information is usually hard to come by and it is often severely

limited in terms of quality and quantity. The attempts made to overcome the inadequacies of experimental data form a basis of this study.

Several developed LV constitutive models include the following: active and passive material properties of the myocardium, a realistic description of muscle fiber orientation, forces exerted upon the heart from outside (e.g., the lungs, diaphragm and chest wall) and the action of blood within the heart chambers. The best model that mimics human LV behavior is selected from several developed models.

Following best model selection, two FE analyses are presented. The first FE analysis is done directly and is aimed at studying the effects of myocardial fiber architecture and material properties on LV mechanics during the cardiac cycle. The second FE analysis is done inversely, whereby an iteration of FE simulation was performed to find the myocardium bulk modulus that gives the best fit between the computed and experimentally measured LV internal cavity volumes. Finally, this study gives another example of FE's role in helping with accurate diagnosis and more effective human heart disease treatment.

CHAPTER 3:PROBLEM FORMULATION OF LEFT VENTRICLE MOTION

3.1 Introduction

In continuum mechanics, materials may have shape deformations depending on the applied loads, material properties, and original shapes. To study the mechanics of a beating heart, a heart model can be loaded with (physiological) cavity pressure. It is possible to examine a heart model's deformation under cavity pressure by solving equilibrium equations to find the deformed state where the applied load is balanced by internal wall stresses. A constitutive relation can give the relation between deformation and stress in the material (the heart model) and the material is characterized by a material law. The resulting equations and domain for solving these are too complex to allow analytical solving and therefore the FE method is used.

3.2 Dynamic equilibrium equation of left ventricle

By applying a pressure load on the endocardial surface, a heart model deforms until it reaches a new equilibrium state. To identify the heart model deformation it is necessary to consider the change in material length, i.e. the material line segment dX in the undeformed heart model must be reconfigured (due to applied load) into dx in the deformed heart model. This deformation is quantified by the deformation gradient tensor $\boldsymbol{F}$, which is defined in standard finite deformation theory by Equation (3.1):

$$dx = \boldsymbol{F}dX \tag{3.1}$$

Some equations that describe the constitutive law for myocardial tissue have been proposed based on the hyperelastic material theory. It postulates the existence of strain energy

potential **W** that does not depend on the material's deformation history but rather on the right Cauchy-Green deformation tensor **C**. A measure of the deformation is defined as follows:

$$\mathbf{C} = \mathbf{F}^T \mathbf{F} = \left\{ \frac{\partial x_k}{\partial X_M} \frac{\partial x_k}{\partial X_N} \right\} \tag{3.2}$$

Equation (3.2) defines Green's deformation tensor or the right Cauchy-Green deformation tensor (Atkin & Fox, 1980), which indicates how each component of the undeformed line segment dX contributes to the squared length of the deformed line segment dx.

In materials undergoing large deformations, it is necessary to define stress tensors and the way they enter into the governing equations. Stress is defined as the force per unit area on an infinitesimally small plane surface. The quantities of force and area can be referred either to the reference (undeformed) or deformed configurations, leading to three important ways of representing stress in a deforming body: using Cauchy, and the first or second Piola-Kirchhoff stress tensors.

The components of the second Piola-Kirchhoff stress tensor are given by the derivatives of $W(\mathbf{C})$ with respect to the components of **C**. As **C** depends only on a material coordinate system, rigid body movement has no influence on the strain energy. Thus the axiom of objectivity, which requires the constitutive law to be invariant with respect to rigid motion of the spatial frame of reference, is satisfied (Fedorov et al., 2010).

The constitutive law for myocardial tissue has three features: high nonlinearity, anisotropy, and dependence on excitation. To describe the myocardial tissue anisotropy (Humphrey et al., 1990a, 1990b) defined W, as a function of the vector defining the preferred direction of muscle fibers. Developing Humphrey's model (Lin & Yin, 1998) proposed a new constitutive equation, which described the changes in the stress-strain behavior caused by

excitation. They divided W into two components: a passive component (W_{pass}) and an active component (W_{act}). (Watanabe et al., 2004) defined the coefficient of W_{act} as a function of the excitation rate. Using W, the mixed variational form of the governing equation for nearly incompressible hyperelastic materials is:

$$\int_V \{\tilde{\rho}\,\ddot{u} \cdot \delta u + (\partial W / \partial C_{ij} + \lambda\,\partial \Psi / \partial C_{ij})\delta C_{ij}\}\,dV = \int_S \tilde{t}\,\ddot{u} \cdot \delta u \; dS \qquad (3.3)$$

$$\int_V \delta\lambda \cdot (\Psi - \lambda/\alpha)\,dV = 0 \qquad (3.4)$$

Equation (3.3) is the form of the dynamic equilibrium equation with the constraint of slight compressibility. Here, V denotes the initial material configuration; ρ is the nominal mass density; $\ddot{u}$ is the acceleration vector; δu is the variation of the displacement vector u; C_{ij} is the ij-th component of C; λ is the Lagrange multiplier that corresponds to the negative half of hydrostatic pressure; Ψ is a function to describe volume change; δC_{ij} is the variation of C_{ij} due to δu; and S is the surface on V where the nominal traction force vector is applied. Equation (3.4) is the form of the slight compressibility constraint. Here $\delta\lambda$ denotes the variation in λ and α is a large value corresponding to the bulk modulus. As excitation rate changes, W changes, causing a shift in the stress-strain relationship, leading to breaking of the equilibrium states described in Equations (3.3) and (3.4). To recover the equilibrium states, the muscle deforms.

3.3 Linear momentum

Liner momentum balance for a body is a generalization of Newton's second law for a particle. Malvern produced this generalization that Cauchy later wrote in terms of stress. The

principle of conserving linear momentum applied to a set of particles (or rigid body) can be stated as the time rate of (linear) momentum change of a collection of particles that equals the net force exerted on the collection. This is expressed mathematically by (Malvern, 1969) in Equation (3.5), where t is the traction vector (external surface forces per unit area), b represents the body forces (per unit mass), and the rate of momentum change is written in terms of the material derivative (d/dt) and the velocity vector v.

$$\int_S t \, dS + \int_V \rho \, b \, dV = \frac{d}{dt} \int_V \rho \, v \, dV$$

(3.5)

Cauchy's formula is substituted into Equation (3.5) to form Equation (3.6), which is appropriate for a material with constant density. Here σ^{ij} are components of the Cauchy stress tensor and are physical stresses ($t \, dS = \sigma^{ij} \hat{n}_i \, dS$), since i_j are unit vectors. Note that Equation (3.6) is written in component form, where the body force and velocity vectors have components $b = b^j i_j$ and $v = v^j i_j$, respectively.

$$\int_S \sigma^{ij} \hat{n}_i \, dS + \int_V \rho \left(b^j - \frac{dv^j}{dt} \right) dV = 0$$

(3.6)

Applying the divergence theorem to Equation (3.6) yields Equation (3.7), where $f^i = \frac{dv^i}{dt}$ are components of the acceleration vector.

$$\int_V \left[\frac{\partial \sigma^{ij}}{\partial x_i} + \rho \, b^i - \rho \, f^i \right] dV = 0$$

(3.7)

If Equation (3.7) is to be valid for arbitrary volumes, the integrand must vanish. It is assumed here that the integrand is continuous. This produces Equation (3.8), which is the component form of Cauchy's first law of motion for rectangular Cartesian coordinates.

$$\frac{\partial \sigma^{ij}}{\partial x_i} + \rho\, b^i \;=\; \rho\, f^i \tag{3.8}$$

It is often convenient to express Cauchy's first law of motion in terms of the second Piola-Kirchhoff stress components, as in Equation (3.9).

$$\frac{\partial}{\partial X_M}\left(T^{MN}\frac{\partial x_j}{\partial X_N}\right) + \rho_o b^i \;=\; \rho_o f^i \tag{3.9}$$

The conservation of linear momentum in the absence of body forces is:

$$\frac{\partial}{\partial X_M}\left(T^{MN}\frac{\partial x_j}{\partial X_N}\right) = 0 \tag{3.10}$$

where T is the second Piola-Kirchhoff stress tensor, X is the coordinate in the undeformed and x in the deformed body.

3.4 Angular momentum

The principle of angular momentum conservation states that the time rate of change in the total momentum for a continuum is equal to the vector sum of the moments of external forces acting on the continuum (Reddy, 2008). Angular momentum conservation is satisfied by requiring the second Piola-Kirchhoff stress tensor to be symmetric:

$$T^{MN} \;=\; T^{NM} \tag{3.11}$$

The second Piola-Kirchhoff stress tensor is used rather than Cauchy stress because it refers all stress back to a known reference state instead of the unknown deformed state.

3.5   Boundary conditions (essential and forced)

There are two types of boundary conditions: essential (*displacement*) and forced (*natural*).

Essential boundary conditions: For most of the actual simulations, the displacement describes the support or constraints on the solid, and hence the prescribed displacement values are often zero. The LV heart chamber can be modeled in isolation using a free body diagram, but the displacement boundary conditions just below the valves must be specified.

Forced boundary conditions: There are two types of forced (natural) boundary conditions on force boundaries (endocardial and epicardial surfaces): force generated by internal blood pressure induced in the LV cavity onto the endocardium surface and force generated by the external surface pressure from surrounding organs onto the epicardium.

Now consider a body of volume V and surface S loaded by a surface traction s, which is in equilibrium with the internal stress vector t. If the body is subjected to an arbitrarily small displacement δu that satisfies compatibility and any displacement boundary conditions specified on S (where δu must be zero), then the principle of virtual work can be expressed in the form of Equation (3.12) (Hughes, 1994).

$$\int_{S_2} s \, \delta u \, dS = \int_{S} t \, \delta u \, dS \tag{3.12}$$

where S_2 is the portion of the boundary that is not subjected to displacement boundary conditions.

The virtual displacements may be resolved into components $\delta u = \delta u_j i_j$. Cauchy's formula $(t \, dS = \sigma^{ij} \hat{n}_i \, dS)$ is then substituted into Equation (3.12) to yield Equation 3.13).

$$\int_{S_2} s \, \delta u dS = \int_S \sigma^{ij} \hat{n}_i \, \delta u_j \, dS \tag{3.13}$$

The right-hand-side surface integral in Equation 3.13) is transformed into a volume integral using Gauss' theorem (Fung, 1965) to give Equation 3.14).

$$\int_{S_2} s \, \delta u \, dS = \int_V \left[\frac{\partial \sigma^{ij}}{\partial x_i} \delta u_j + \sigma^{ij} \frac{\partial \delta u_j}{\partial x_i} \right] dV \tag{3.14}$$

Cauchy's first law of motion (Equation (3.8)) is substituted into the volume integral in Equation (3.14) to give Equation 3.15). Moreover, Equation 3.15) is expressed in terms of the second Piola-Kirchhoff stress tensor, as written in Equation (3.16).

$$\int_V \sigma^{ij} \frac{\partial \delta u_j}{\partial x_i} dV = \int_V \rho \left(b^i - f^i \right) \delta u_j \, dV + \int_{S_2} s \, \delta u \, dS \tag{3.15}$$

$$\int_V T^{MN} \frac{1}{J} \frac{\partial x_j}{\partial X_M} \frac{\partial \delta u_j}{\partial X_N} dV = \int_V \rho \left(b^i - f^i \right) \delta u_j \, dV + \int_{S_2} s \, \delta u \, dS \tag{3.16}$$

All terms in Equation (3.16) have now been defined apart from the right-hand side integral involving the surface traction vector *s*. If external surface pressures are applied, this integral must be evaluated for those boundary portions that sustain the loads. In the absence of boundary pressures, this term vanishes.

Consider a deforming surface with unit normal $\hat{n} = \hat{n}_j i_j$. If the surface is loaded by a pressure, $P_{(appl)}$ (a physical stress), then the surface traction vector has components s = $P_{(appl)} \hat{n}_j i_j$ and the right-hand side surface integral of Equation (3.16) is evaluated using Equation (3.17).

$$\int_{S_2} s \, \delta u \, dS = \int_{S_2} P_{(appl)} \, \hat{n}_j \delta u_j \, dS \tag{3.17}$$

This surface integral is then substituted into Equation (3.16) to yield the governing equations for finite deformation elasticity with respect to rectangular Cartesian coordinates given in Equation 3.18).

$$\int_V T^{MN} \frac{1}{J} \frac{\partial x_j}{\partial X_M} \frac{\partial \delta u_j}{\partial X_N} dV = \int_V \rho \left(b^i - f^i \right) \delta u_j \, dV + \int_{S_2} P_{(appl)} \, \hat{n}_j \delta u_j \, dS \tag{3.18}$$

It remains to solve Equation 3.18) in terms of the unknown virtual displacement δu_j, subject to any displacement boundary conditions. For geometrically simple bodies with straightforward material behavior, Equation3.18) can be used in its present form.

3.6 Finite element formulation

The heart of any finite element formulation is the element stiffness description. The finite element formulation and equations governing the model dynamics are derived from the Lagrangian equations of motion (Zienkiewicz & Taylor, 2000).

$$\dot{u} + k \left(u - u_0 \right) = P \tag{3.19}$$

where u and u_0 is the displacement vector in the deformed and undeformed body respectively; k is the finite element stiffness matrix; and P is the applied load vector.

The LV model stiffness matrix k is calculated by directly adding the element stiffness matrix k^e, where n is the number of elements in the LV model as:

$$k = \sum_{i=1}^{n} k_i^e \tag{3.20}$$

The element stiffness matrix k^e can be expressed as:

$$k^e = \int_{v^e} B^T \, D \, B \, dV \qquad (3.21)$$

where v^e is the element volume; B is the strain-displacement relation matrix; and D is the stress-strain relation matrix.

The strain-displacement relation matrix B is directly associated with the shape function and geometry of each element. The strain-displacement relation in terms of element nodal displacement can be expressed as:

$$\Delta\epsilon = B \, \Delta u \qquad (3.22)$$

where $\Delta\epsilon$ is the incremental strain vector and Δu is the incremental displacement vector.

The stress-strain relation in the element can be expressed as:

$$\Delta\sigma = D \, \Delta\epsilon \qquad (3.23)$$

where $\Delta\sigma$ is the incremental stress vector.

The vector of the applied load P acting on the LV model is given by:

$$P = P_{ma} + P_{bp} + P_{sp} \qquad (3.24)$$

where P_{ma} is the active force generated by the myocardium muscles; P_{bp} is the force generated by the blood pressure on the endocardium surface; and P_{sp} is the force generated by external pressure from surrounding organs onto the epicardium surface.

The active force generated by the myocardium muscles is expressed as:

$$P_{ma} = \sum_{v^e} N^T p_{ma} \; dV \tag{3.25}$$

where N is the element shape function.

The force P_{bP} generated by the blood pressure in the LV cavity can be expressed as:

$$P_{bp} = \sum_{s^{endo}} N^T p_{bp} \; dS \tag{3.26}$$

where s^{endo} is the surface area of elements on the endocardial surface.

The external surface force P_{sp} generated from the pressure of the surrounding organs:

$$P_{sp} = \sum_{s^{epi}} N^T p_{sp} \; dS \tag{3.27}$$

where s^{epi} is the surface area of the elements on the epicardial surface.

The LV model equilibrium is obtained when the following global energy functional is minimized:

$$E_g = E_{exf} + E_{def} \tag{3.28}$$

where E_{exf} is the energy due to the external forces and E_{def} is the deformation energy.

3.7   Basis functions for the element used

To analyze stress in a body undergoing large elastic deformations, the equations that govern finite deformation elasticity developed in previous sections must be solved. For materials with regular geometries and simple properties, this may be done analytically. However, for

most practical applications materials behave nonlinearly and assume complex shapes, like the heart muscle. Irregular domains may be discretized into a number of smaller regular elements, over which quantities of interest (for example the geometric coordinates of a point) are continuously approximated. The two main types of *basis functions* applied in this thesis, also known as *shape* or *interpolation functions*, are 20-node hexahedral and 15-node solid triangular basis functions. These are used to approximate quantities of interest (for instance geometric or solution variables) that vary over a particular domain. They consist of sets of polynomials of different degrees, depending on the desired approximation accuracy (generally the higher the degree, the better the approximation).

The 20-node hexahedral element is shown in Figure 3.1 and has twenty nodes located at the corners and mid-edges of the element. It has three translational degrees of freedom at each node. The shape function defining the geometry and variation of displacement is given as follows:

For corner nodes:

$$N_i = \frac{1}{8}(1 + rr_i)(1 + ss_i)(1 + tt_i)(rr_i + ss_i + tt_i - 1) \qquad i = 1, 2, \dots, 8 \tag{3.29}$$

where r, s, t are natural coordinates and, r_i, s_i, t_i are the natural coordinates' values for a node i.

For mid-side nodes:

$$N_i = \frac{1}{4}(1 - r^2)(1 + ss_i)(1 + tt_i) \qquad i = 9, 13, 15, 11 \tag{3.30}$$

$$N_i = \frac{1}{4}(1 - s^2)(1 + rr_i)(1 + tt_i) \qquad i = 10, 14, 16, 12 \tag{3.31}$$

$$N_i = \frac{1}{4}(1 - t^2)(1 + rr_i)(1 + ss_i) \qquad i = 18, 19, 20, 17 \tag{3.32}$$
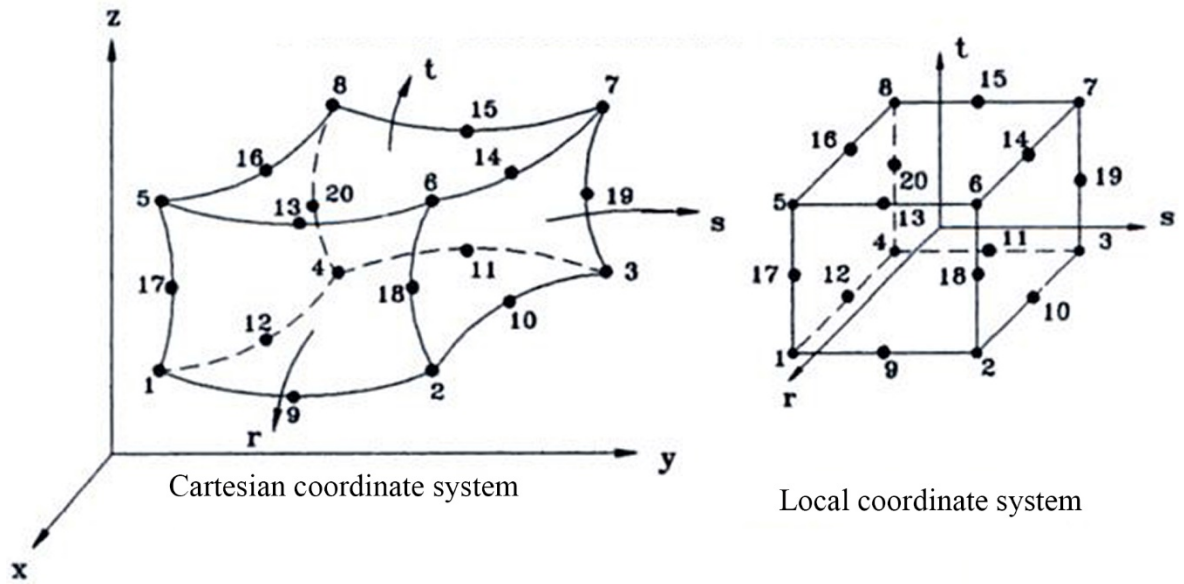
Figure 3.1: Twenty-node hexahedral element (Krishnamoorthy, 1995)

A 15-node solid triangular element is illustrated in Figure 3.2 and has fifteen nodes located at the element's corners and mid-edges. The shape function defining the geometry and variation of displacement is given as follows:

For corner nodes $L_1 = t_1 = 1$:

$$N_1 = \frac{1}{2}L_1(2L_1 - 1)(1 + t) - \frac{1}{2}L_1(1 - t^2) \tag{3.33}$$

For mid-edge triangle:

$$N_7 = 2L_1L_2(1 + t), \quad etc. \tag{3.34}$$

For mid-edge rectangle:

$$N_{10} = L_1(1 - t^2), \quad etc. \tag{3.35}$$
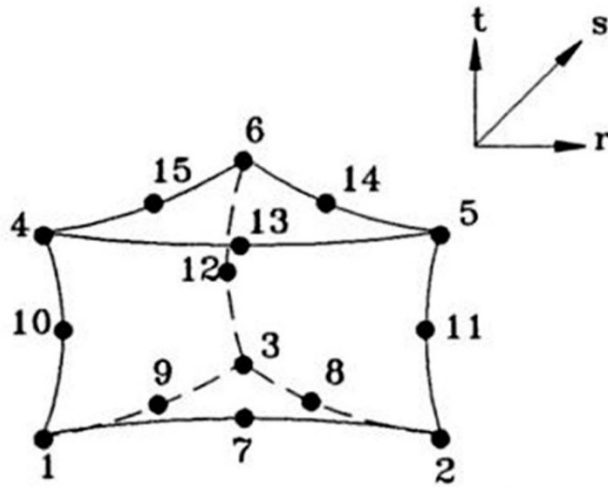
Figure 3.2: Fifteen-node solid triangular element (Krishnamoorthy, 1995)

3.8 Solution procedure

Essentially, FE software ANSYS was employed to solve the governing equations described from Section 3.2 to Section 3.7. These governing equations are based on the finite deformation theory. The basic steps involved in FE analysis are:

1. Create and discretized the LV domain into finite elements. In other words, subdivide the LV into nodes and elements.

2. Assume a shape function to represent the physical behavior of an element.

3. Develop equations for an element.

4. Assemble the elements to present the entire problem. Construct the global stiffness matrix.

5. Apply boundary conditions: initial conditions and loading.

6. Solve a set of nonlinear algebraic equations simultaneously to obtain displacement at different nodes.

The ANSYS program calculates the system stiffness matrix at each load step increment. If the displacements at the end of the increment satisfy the chosen tolerance, no recycling takes place. During recycling, the strains recovered from the previous iteration are used as estimated strains for stiffness evaluation. The system from Equation 3.36) becomes:

$$\frac{du}{dt} + k(u)\delta u = P - I(u) \tag{3.36}$$

where k (stiffness matrix) and I (vector of resorting loads corresponding to element internal loads) are functions of u (displacement). Suppose that the last obtained approximate solution is termed u^i, where i indicates the iteration number. Equation 3.36) may then be written as:

$$\frac{du}{dt} + k(u^i)\delta u = P - I(u^i) \tag{3.37}$$

The above equation is solved for . This concludes one iteration and no recycling takes place if convergence is satisfied. This convergence is known as displacement checking and it is defined as:

$$\frac{\|\delta u\|}{\|u - u_o\|} < TOL \tag{3.38}$$

where TOL is the relative displacement tolerance. If convergence is not satisfied, recycling occurs and the next appropriate solution is obtained:

$$u^{i+1} = u^i + \delta u^i \tag{3.39}$$

The solution converges rapidly if the total loads (internal and external) P are smooth functions of the generalized nodal displacement u and if the starting guesses u^o are not too far away from the actual solution.

3.9   Convergence criteria

For an incremental solution based on iterative methods, realistic criteria should be used to terminate the iteration. At the end of each iteration, the solution obtained should be checked to see whether it has converged within preset tolerance or whether the iteration is diverging. If the convergence tolerance is too loose, inaccurate results are obtained, and if the tolerance is too tight, a great deal of computational effort is spent to obtain needless accuracy. Similarly, an ineffective divergence check can terminate the iteration when the solution is not actually diverging or force the iteration to search for an unattainable solution.

In order to carry out a mesh sensitivity test, numerical simulations were performed by varying the number of elements in the LV wall. The mesh sensitivity was tested on the LV cavity volume and pressure variables by varying the number of elements. It was found that a computational domain of 22080 elements was sufficient for convergence. The simulation results did not show any difference when the convergence criterion set was changed from 10^{-5} to 10^{-6} (values of tolerance). Hence, the study was carried out with the convergence criteria of 10^{-5}.

CHAPTER 4:METHODOLOGY

4.1   Introduction

An FE analysis tool is necessary because the myocardium mechanics problem is complex and the corresponding analytical solution is not feasible otherwise. The most notable difficulty is with predicting the following parameters:

1. The globally anisotropic behavior of cardiac tissue due to the muscle fiber arrangement

2. Live tissue mechanical properties, such as myocardial tissue bulk modulus

Therefore, the desired FE analysis is supposed to assist to evaluate the myocardial tissue bulk modulus and study the effects of myocardial fiber architecture in LV function. This chapter thus explains myofiber structure and the procedure of creating an FE model suitable for solving these problems.

4.2   Model assumption

In this study, a model for the mechanical behavior of LV is proposed with less restrictive assumptions than those inherent in previous studies:

- The assumed geometry is ellipsoid truncated at two-thirds of the major axis. This simplified geometry is based on MRI clinical measurements (initial volume = 50ml).

- The myocardial fiber architecture was assumed to be layers of uniformly spaced reinforcement bars (rebar) within the continuum 3D elements; each layer was set parallel to two of the isoparametric directions in the element's local coordinate system.

- A uniform elastic foundation was assumed to mimic the influence of surrounding organs and tissue on heart deformation.

- The rate of myocardial Young's modulus change was assumed the same as that of LV internal cavity pressure multiple by constant value. This constant was calculated based on the hypothesis presented in section 4.6.

4.3 Left ventricle geometry and finite element model

A 3D FE model was built to simulate the deformation mechanics of the LV using ANSYS® commercial software. To simplify the analysis, the FE simulation model was represented by an ellipsoid truncated at two-thirds of the major axis including two sets of fibers (myocardial fibers bound by a mesh of collagen fibers) attached to each other to form a spatial network. The geometric parameters and dimensions of the LV model in the initial undeformed configuration (at hypothetical zero pressure applied inside the LV cavity) are shown in Figure 4.1.

The wall thickness of the LV model, in the reference unstressed state, was divided into seven equal-thickness layers. Figure 4.2a shows the initial shape of a typical FE mesh used for the present computations, while Figure 4.2b illustrates the end-diastolic deformed shape of the FE mesh. The LV model wall was discretized with a 20-node tetrahedral prism element, with the exception of the apical region that was meshed using a 15-node triangular prism element. The current FE mesh consists of 22,080 total elements and 29,777 nodes. This discretization of the current LV model is quite enough and any further mesh refinement shows very little improvement (Hassaballah et al., 2014). The LV blood cavity was modeled by the hydrostatic fluid 3D solid element, which is well suited for calculating fluid (blood) volume and pressure for coupled problems involving fluid-solid interaction. Hydrostatic fluid

elements were overlaid on the faces of the 3D solid element enclosing the fluid volume.
Figure 4.2c presents a section view of the FE mesh, clarifying the shape of the elements used
to model the LV internal cavity. Nine nodes define the hydrostatic fluid element: eight on
the internal LV cavity surface (endocardium) and the remaining, pressure node, at the base
center. This pressure node defines the LV pressure, which is assumed uniform through the
LV cavity; the predefined pressure value is automatically moved to the centroid of the fluid
volume. In all FE computations, the LV cavity and LV wall volumes were kept constant at
50ml and 73.6ml, respectively. The circumference of the LV internal cavity was divided into
48 equally spaced divisions, i.e. 48 elements along the circumferential direction.
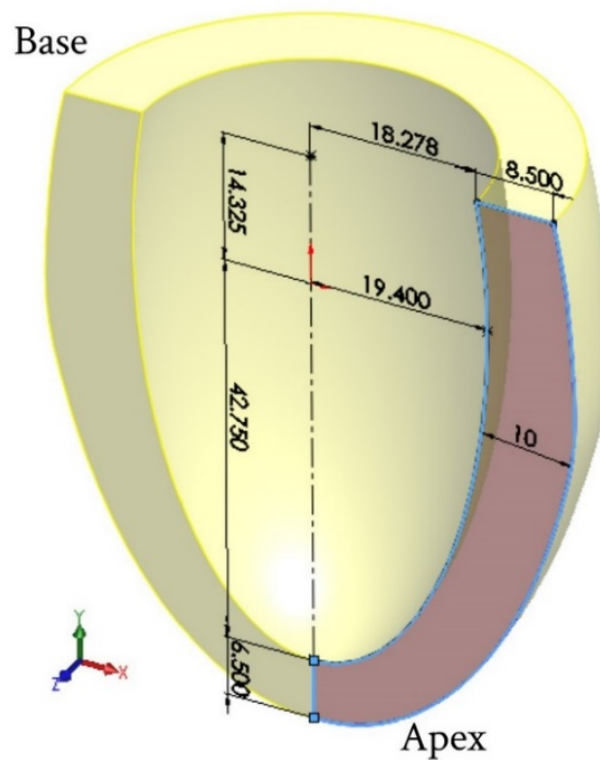
Figure 4.1: Geometric parameters of thick-walled ellipsoid truncated at two-thirds of the
major axis used to simulate the LV model (to clarify the half-solid model presented)
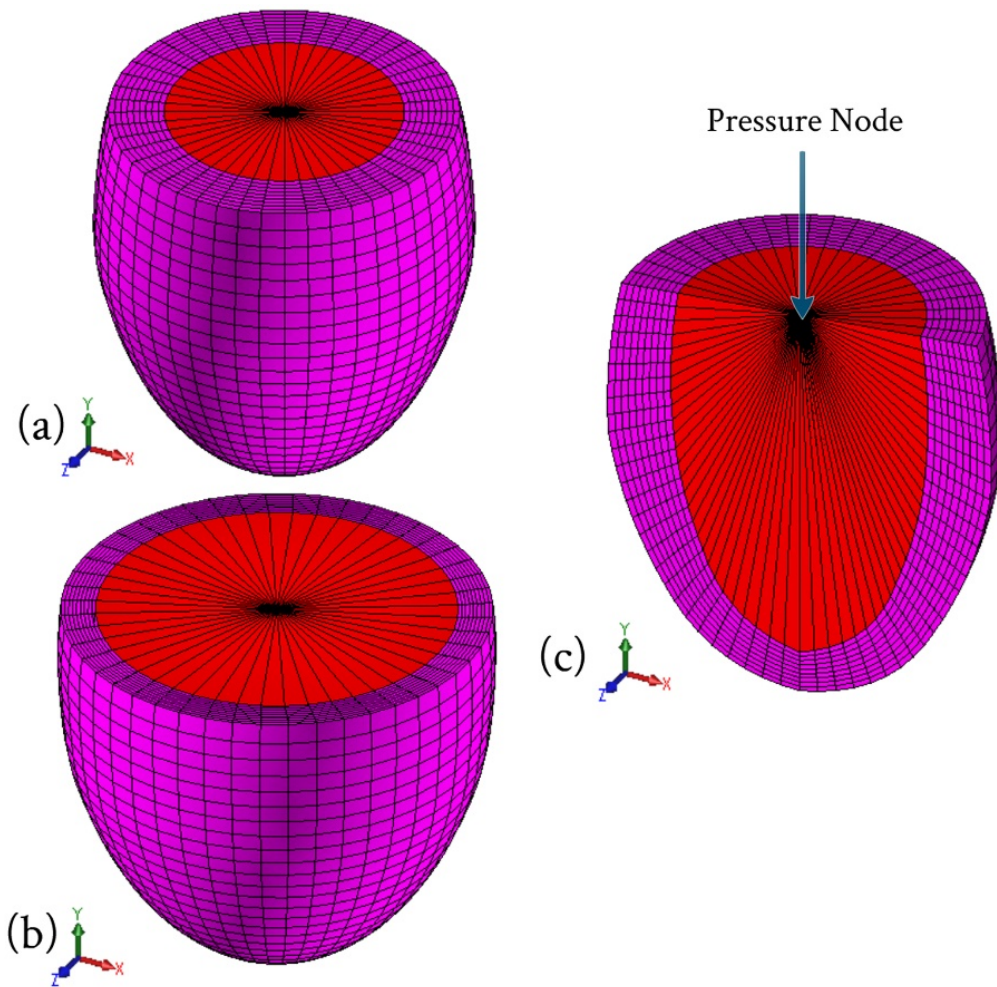
Figure 4.2: The left ventricular FE mesh (a) Initial shape of the FE mesh; (b) Deformed shape of the FE mesh at the LV end-diastole; (c) Section view in the FE mesh presenting the elements used to simulate the LV cavity

Two separate parallel sets of 3D fiber network contractile muscle fiber bundles (myofibers) bound by a mesh of collagen fibers were embedded within a continuum 3D solid element to reproduce the globally anisotropic behavior of cardiac tissue. Computationally, these fibers were modeled as layers of uniformly spaced reinforcement bars (rebar) within the continuum 3D elements; each layer was set to be parallel to two of the isoparametric directions in the element's local coordinate system.

The collagen fibers were arranged in the radial direction, while the myofibers' orientation changed with position within the LV wall. The 3D reinforcing element was used to simulate both myofibers and collagen fibers. The continuum 3D element is suitable for simulating reinforcing fibers with arbitrary orientations and to model myofiber force. The force is restricted in the fiber's direction only (uniaxial fiber tension). The reinforcing element was firmly attached to its base element, i.e. no relative movement between the reinforcing element and the base was allowed. FE computations were conducted with myofiber and collagen fiber volume fractions of 0.7 and 0.015, respectively (LeGrice et al., 1995; Stevens et al., 2003).

4.4 Material model

The myocardium tissue (matrix) is represented as an isotropic, slightly compressible hyperelastic material with relatively soft properties, using the energy function given by Equation 4.1).

$$W = \sum_{n=1}^{N} \frac{\mu_n}{\alpha_n} \left[J^{\frac{-\alpha_n}{3}} \left(\lambda_1^{\alpha_n} + \lambda_2^{\alpha_n} + \lambda_3^{\alpha_n} \right) - 3 \right] + 4.5K \left(J^{\frac{1}{3}} - 1 \right)^2 \tag{4.1}$$

where μ_n and α_n are material constants, K is the initial bulk modulus, and J is the volumetric ratio defined by $J = \lambda_1\lambda_2\lambda_3$, where λ_1, λ_2 and λ_3 are the principal stretch ratios.

Table 4.1 shows the Ogden parameters employed in the present study to simulate the material properties of myocardium tissue. The parameters were calculated through uniaxial and relaxation tests carried out by (Hassan et al., 2012). The collagen fiber behavior was represented by isotropic linear elastic with large displacements to simulate the large strains occurring in the collagen fiber during LV filling. Table 4.2 summarizes the material properties for collagen.

Table 4.1: Values of two-term Ogden parameters found by (Hassan et al., 2012)

Parameter	Value	Units
μ_1	0.22	MPa
μ_2	0.11	MPa
α_1	11.77	—
α_2	14.34	—

Table 4.2: Collagen material properties (Bagnoli et al., 2011)

Young's modulus, E (kPa)	Poisson's ratio, ν	Density, ρ (kg/m^3)
50	0.49	1000

4.5 Left ventricle myofiber architecture

Cardiac muscle tissue is composed of a helical network of muscle fibers oriented at different angles throughout the ventricle wall in the form of sheets separated by a complex structure of cleavage surfaces (Figure 1.6 andFigure 4.3) (Helm et al., 2005; Sengupta et al., 2006; Arts et al., 2012). This arrangement of muscle fibers is responsible for the orthotropic mechanical properties of cardiac muscle (Guccione et al., 2010). The alternating contraction and relaxation of cardiac muscle is the result of the shortening and stretching of the individual muscle, which cause efficient blood ejection (Streeter, 1979; Costa et al., 1999). In other words, fiber architecture is a key feature of the myocardium, where the fiber orientation plays a significant role in both systolic deformation and early diastolic function (Shapiro & Rademakers, 1997).
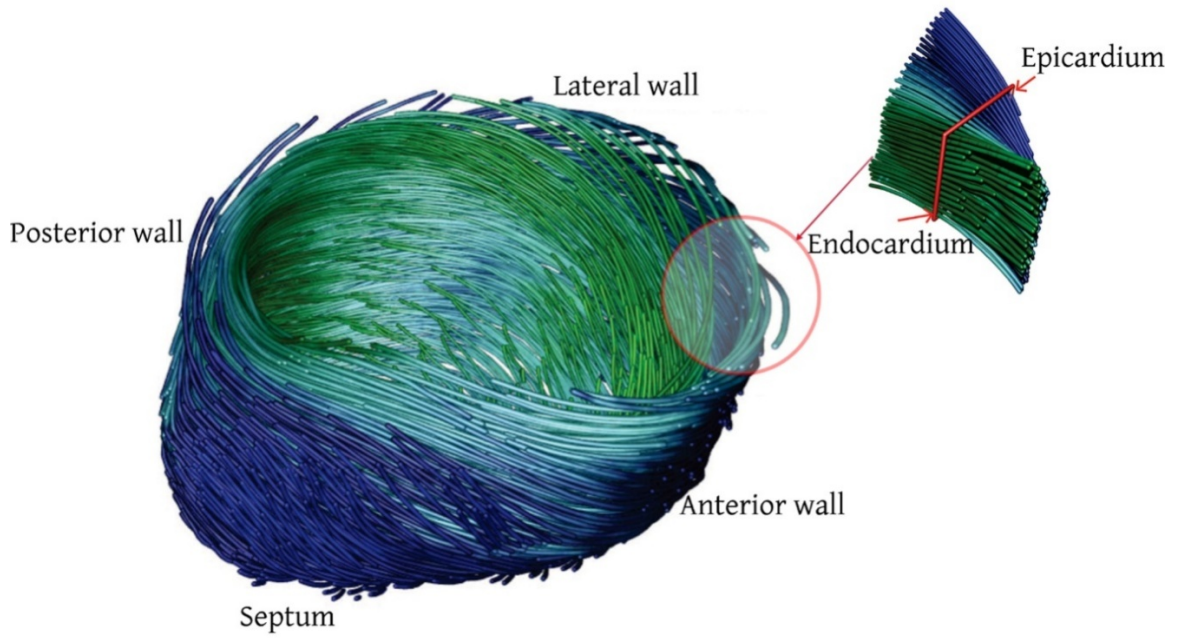
Figure 4.3: Visualization of the left ventricle's fiber structure. The color intensity depends on the inclination angle value. The dark blue and dark green represent larger angles for the epicardium and endocardium, respectively (Rohmer et al., 2006)

The LV fiber architecture can be described spatially by two inclination angles: the helix angle (β) and transverse angle (η) (Scollan et al., 1998). The helix angle (β) is defined as the angle between the local circumferential direction and the projection of the fiber path perpendicular to the local radial direction (Figure 4.4a and Figure 4.5b). The transverse angle (η) is defined as the angle between the local circumferential direction and the projection of the fiber path on the plane perpendicular to the local longitudinal direction (Figure 4.4a and Figure 4.5b) (Schmid et al., 1997).
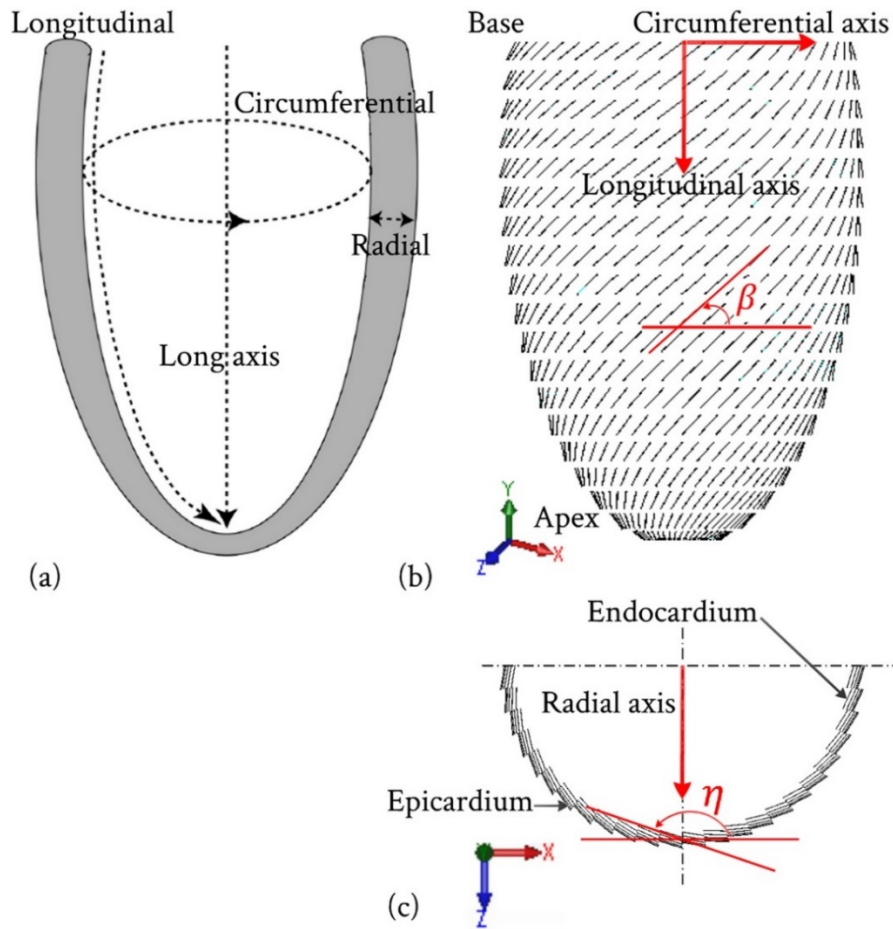
Figure 4.4: Fiber orientation angles (helix angle β and transverse angle η) with the cardiac mechanical coordinate LV axes (a) Radial, circumferential, longitudinal, and long axis directions; (b) Definition of helix angle (β); and (c) Definition of transverse angle (η)

With the recent advances in imaging technologies, fiber angle orientation can be measured via diffusion tensor magnetic resonance imaging (DT-MRI) (Lombaert et al., 2011; Lombaert et al., 2012; Yang et al., 2012). Previous studies have shown that the helix angle (β) varies continuously from approximately +60˚ at the endocardium (the inner heart layer) to -60˚ at the epicardium (the outermost heart layer), whereas the transverse angle (η) varies continuously from approximately +15˚ at the base to -15˚ at the apex (Figure 4.5) (Hsu et al., 1998; Geerts et al., 2002; Kerckhoffs et al., 2003; Chen et al., 2005).
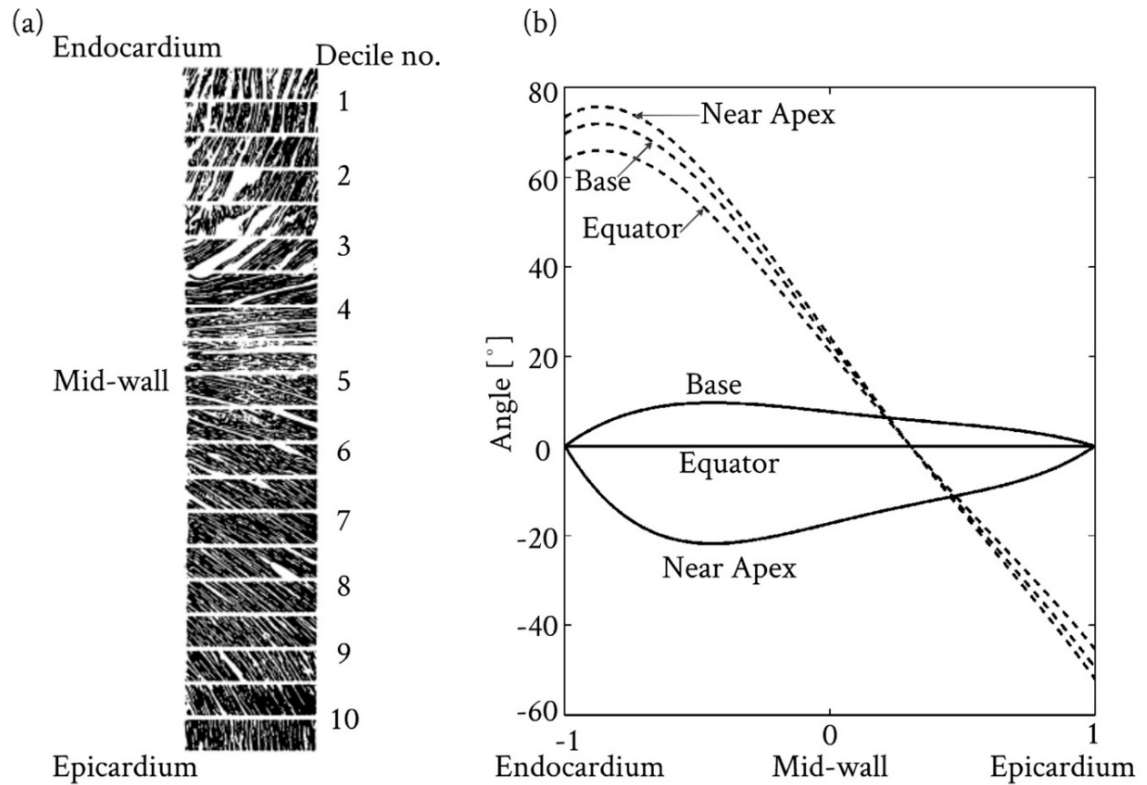
Figure 4.5: Fiber orientation within the myocardium (a) Slices taken at various depths through the wall (Streeter Jr et al., 1969); (b) Myofiber orientation as a function of transmural position at several longitudinal positions; helix angle (--) and transverse angle (-) are components of myofiber orientation (Kerckhoffs et al., 2003)

In this study, based on DT-MRI measurements done by (Rohmer et al., 2006) the corresponding variations in fiber helix angles (β) through the eight regions (Figure 4.6) are listed in Table 4.3. The helix angle (β) distribution varied smoothly across the LV wall thickness from a negative angle at the epicardium to a positive angle at the endocardium, respectively. The transverse angle (η) distribution was taken as a variable value in a linear manner from +15° at the base to the circumferential direction (η = 0°) in the equatorial region to -15° at the apex (Kerckhoffs et al., 2003). The collagen fibers are arranged in the radial directions.

Table 4.3: The corresponding fiber helix angle (β) variations through the eight regions

Left ventricle region	Variations in fiber helix angles (β)
Septum-basal region	-60˚: +40˚
Anterior-basal region	-40˚: +60˚
Lateral-basal region	-20˚: +50˚
Posterior-basal region	-20˚: +60˚
Septum-apical region	-50˚: +40˚
Anterior-apical region	-20˚: +60˚
Lateral-apical region	-20˚: +50˚
Posterior-apical region	-20˚: +60˚
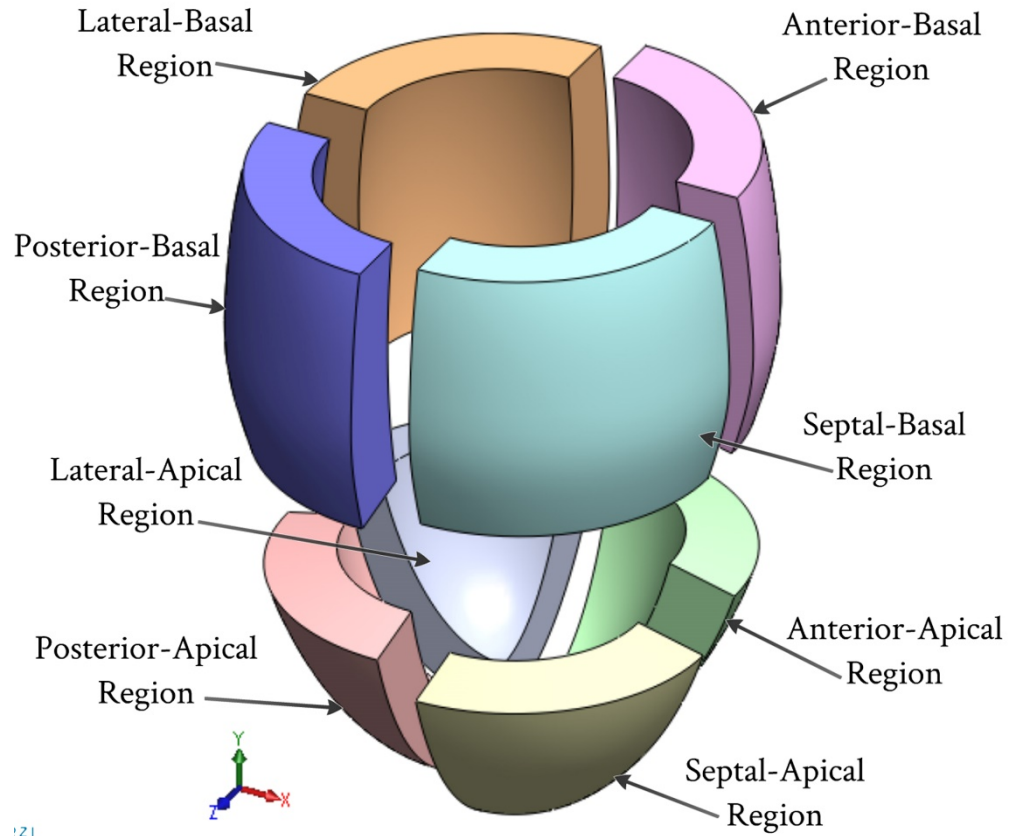
Figure 4.6: Eight LV regions used to clarify the helix angle (β)

4.6 Loading and boundary conditions

To demonstrate the performance of the proposed FE model, an LV pressure vs. time curve for a healthy human heart was used (Figure 4.7). This case was adapted from the experimental measurements performed by (Hall, 2011). The LV pressure vs. time curve in Figure 4.7 represents the FE model applied loads, while the accompanying LV internal cavity volumes were adopted as the FE model's target values.
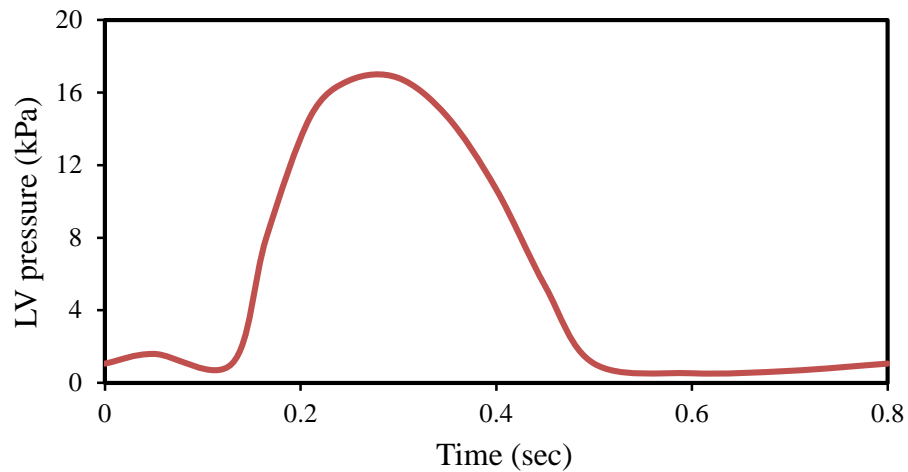
Figure 4.7: Measured LV pressures during one cardiac cycle starting from atrial systole

The surrounding organs (lungs, ribcage, and diaphragm) affect the heart's external surface. In order to simulate the boundary conditions imposed by these surrounding organs and tissues, an elastic foundation 3D structural surface effect element with stiffness $K_f = 0.02$kPa was used (Bettendorff-Bakman et al., 2006, 2008). Due to the lack of information on the influence of surrounding organs and tissue on heart deformation, a uniform elastic foundation was assumed.

To prevent rigid body motion of the model, the degrees of freedom for all nodes at the base were suppressed in the longitudinal direction (UY=0). To avoid possible excessive deformations of FE mesh elements, the pressure node was fixed laterally (UX=UZ=0) (Figure 4.8).
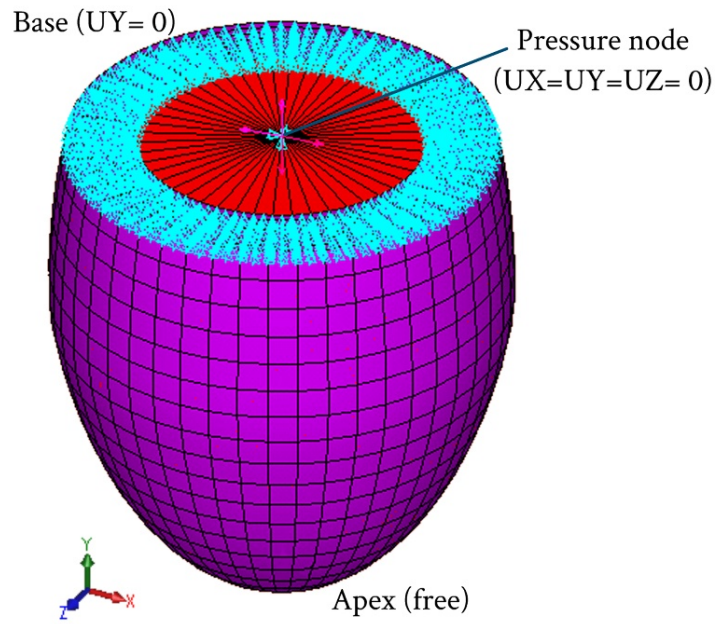
Figure 4.8: The boundary conditions of the LV model (UY = 0 for nodes at the base of the LV and UX = UZ = 0 for the pressure node)

4.7   Myocardium active and passive material properties

The LV pressure response to volume changes during the ejection phase relies on the active elastance property activated by muscle action. During the systolic phase, the muscle generates adequate contractile force (muscle active force) to provide sufficient LV pressure to open the aortic valve and pump an appropriate volume of blood (ZHONG et al., 2007). At the beginning of the isovolumic contraction, the LV's internal cavity pressure increases rapidly and the peak pressure and consequently muscle contraction force continually increase to sustain the increasing LV pressure. Both LV pressure and muscle contraction force increase simultaneously until a peak is reached. During cardiac cycle, the LV wall is subjected to dual forces: the active force generated by the myocardium muscle and the force generated by the blood pressure in the LV cavity. The active muscle force is not only

governed by myocardial passive properties but also depend mainly on the myocardium's active elastance operating throughout the cardiac cycle.

In this study we suggest a simple method to calculate the active myofiber elastance properties taking into consideration that the maximum myofiber Young's modulus value does not exceed 0.5MPa (Watanabe et al., 2006; Venugopal et al., 2012). The active myofiber elastic properties during the cardiac cycle can be simply calculated by multiplying the LV pressure value (given in Figure 4.7) with a constant value of 29.5, i.e. the value of active myofiber Young's modulus depending linearly on the intracavital pressure. This constant value of 0.5 (maximum myofiber Young's modulus) is divided by the maximum LV pressure value. The computation of active myofiber Young's modulus based on the above-calculated constant represents the present study hypothesis. Figure 4.9 shows the calculated active myofiber Young's modulus vs. time during one cardiac cycle. The time-dependent calculated values of active myofiber Young's modulus are applied to the FE model in order to calculate the contraction force in the myocardial wall.
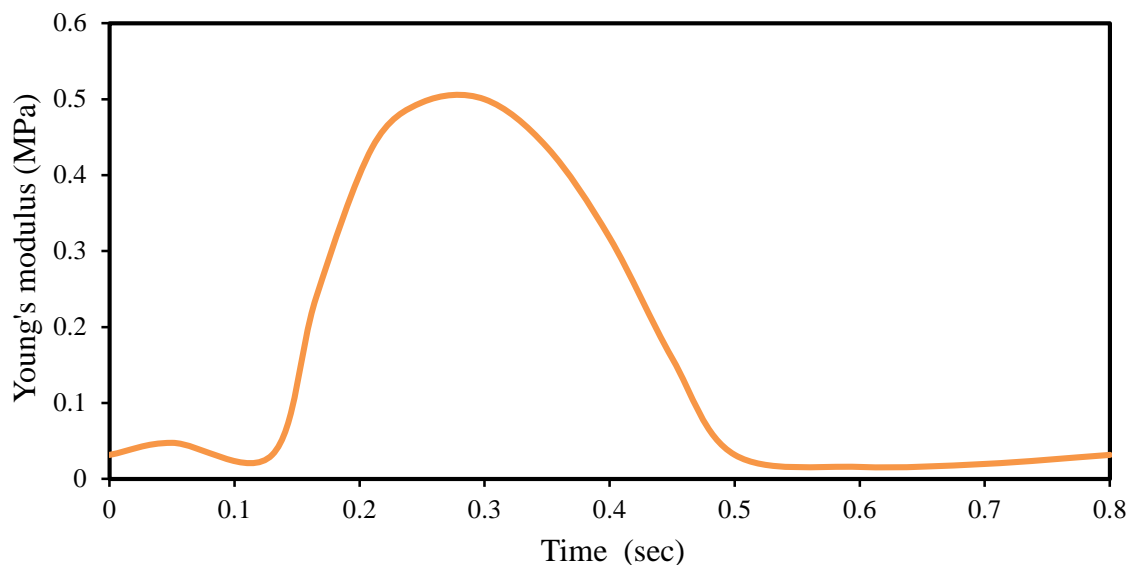
Figure 4.9: Calculated active myofiber Young's modulus (myocardial stiffness) during one cardiac cycle

4.8 Direct and inverse finite element methods

Usually, FE analysis can be done directly when the input parameters, such as LV geometry, LV internal cavity pressure and myocardium tissue properties are known. Once the model is constructed, the desired outputs including deformation behavior, LV cavity volume, LV wall stresses and strains can be predicted from the model. However, it is not uncommon in reality for some or all output values to be known from experiments beforehand, while some of the input parameters still need to be determined. This requires doing the FE analysis inversely, where FE simulation iteration is performed to find the material properties that give the best fit between the computed and experimentally measured LV internal cavity volumes. An inverse FE approach is a complex engineering process that can determine the unknown causes of known consequences. This approach has the advantage that determining the dynamic properties is measured non-invasively.

Direct FE method: The direct method regarding computer-assisted FE analysis explains the steps to follow to mimic muscle contractions (systole) and expansions (diastole). Figure 4.10 shows the direct FE computation sequence procedures for human LV and provides a reliable description of both muscle fiber orientation and material characteristics based on experimental data documented in the literature. This method helps explore the influences of different mesh densities, constitutive models, orientations, and fiber volume fractions.

Inverse FE method: Figure 4.11 represents the inverse FE computation sequence procedure for myocardial bulk modulus identification. The myocardial tissue bulk modulus, as the required output, is inversely identified. The LV pressure vs. time curve is shown in Figure 4.7 as the inputs are applied on the internal LV cavity surface (endocardium) via the pressure node of the hydrostatic fluid element (Figure 4.2). The other passive material properties of myocardium tissue (section 2.4) are fixed as material constants. The calculated

active myofiber Young's modulus (Figure 4.8) is used to simulate the muscle active contraction force generated through the LV wall during the cardiac cycle.

An initial guessed value of tissue compressibility for the myocardium was then applied, and by successive computations, it was refined until the calculated LV cavity volume matched the measured volume. Iterative FE computation for the LV cavity volume during the cardiac cycle was carried out. At the end of each computation step, the FE-predicted LV cavity volume was compared with the measured value. The computation ended if the relative error between the computed and measured values was $\leq 1\%$. For this calculation, the total computation time for each run was about 1000s using PC Intel Core i7 (2.93 GHz with RAM 2.00GB). At the start of all FE computations, the LV wall was initially assumed stress-free (LV cavity pressure equaled zero).
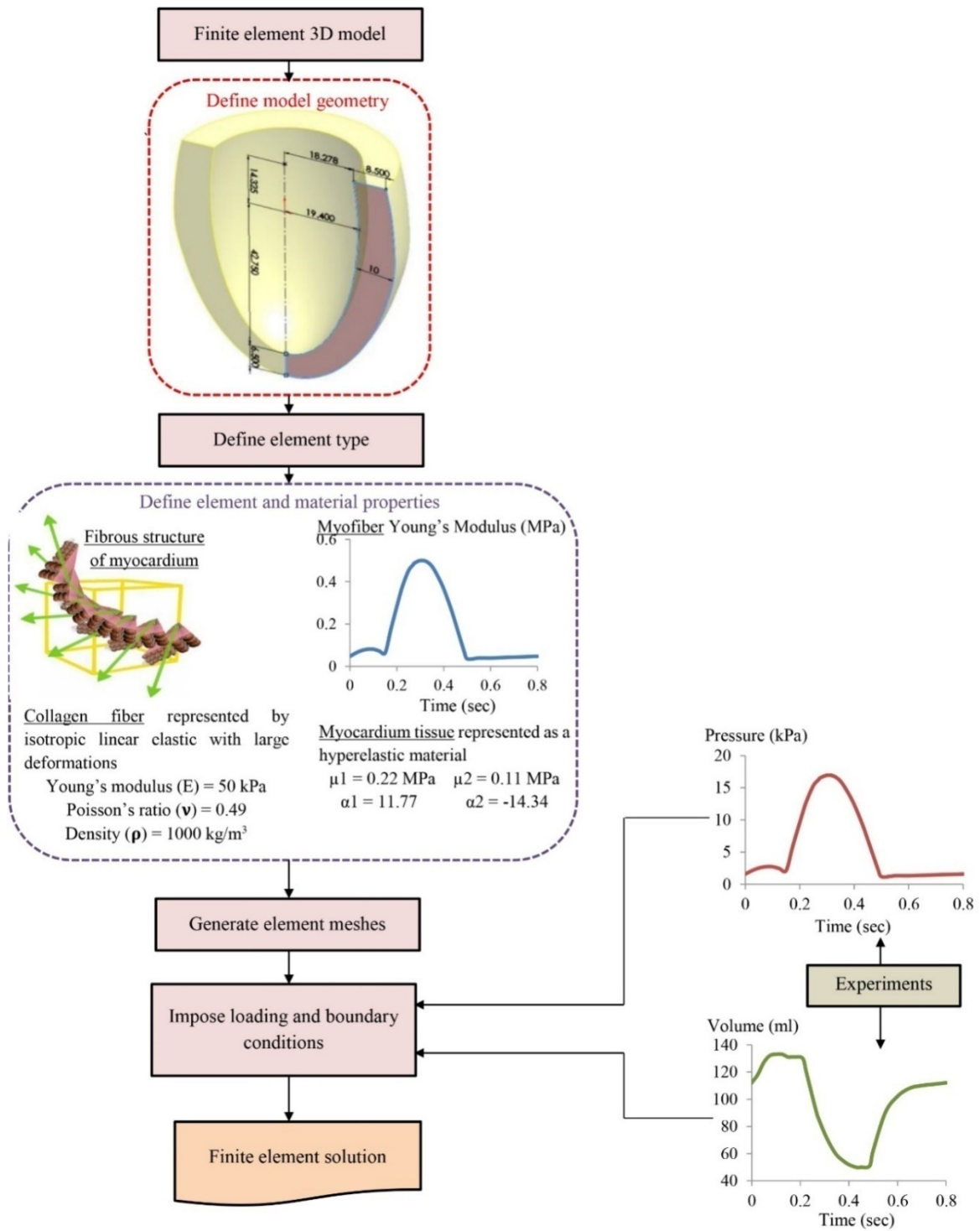
Figure 4.10: Flowchart of direct finite element method
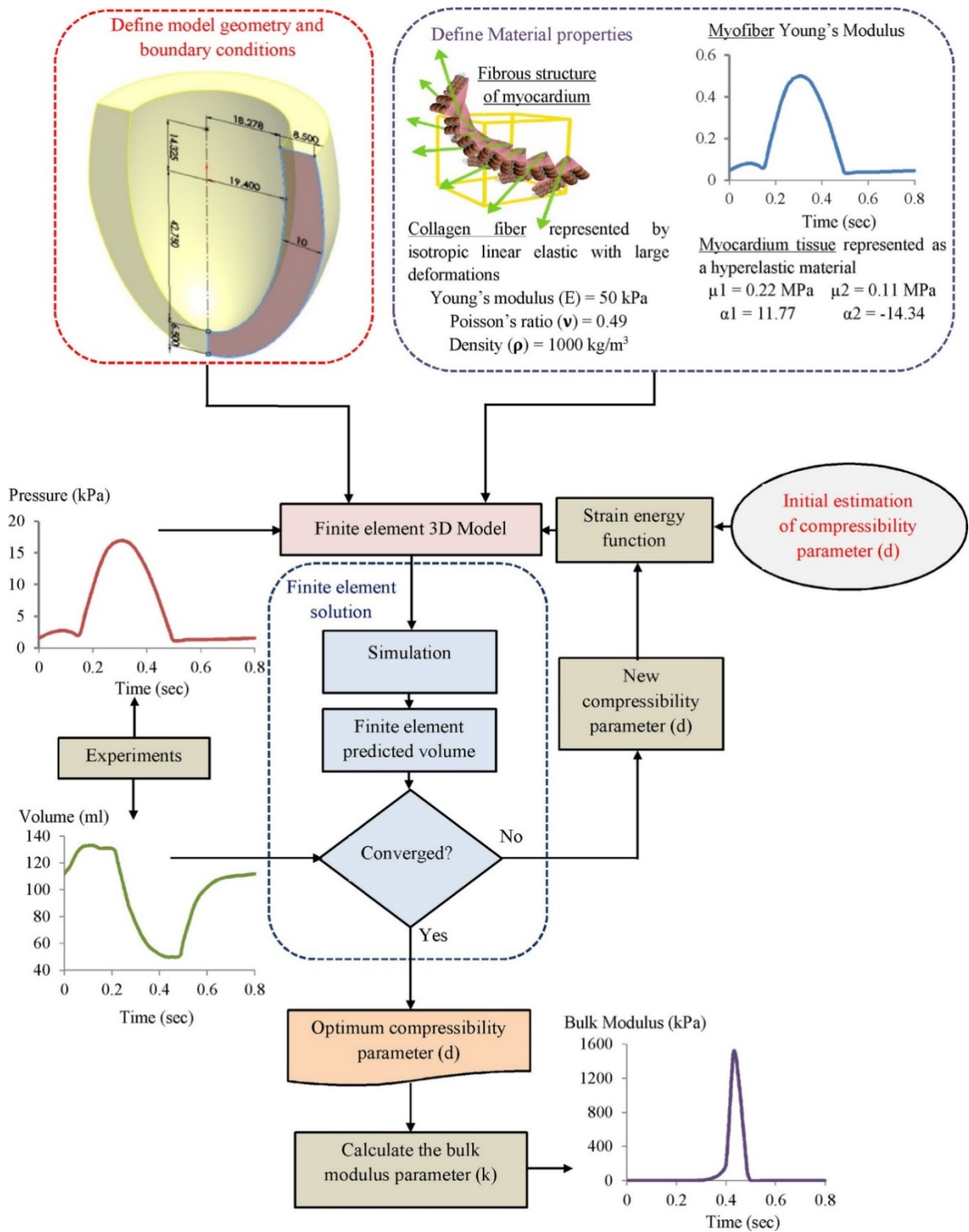
Figure 4.11: Flowchart of the inverse FE computation sequence for LV tissue bulk-modulus identification

4.9   Finite element models' merits and limitations

The direct FE model is presented in a sensitivity study of cardiac mechanics with respect to myocardial fiber architecture. In particular, we explore the influence of various mesh densities, constitutive models, orientations, and fiber volume fractions. This valuable study informs future modeling efforts. Meanwhile, an inverse FE model with the ability to determine the myocardial tissue bulk modulus during a cardiac cycle is presented. The advantages of both proposed methods include:

1. Slightly compressible hyperelastic tissue properties.

2. Realistic boundary conditions based on MRI observations.

3. Myofiber orientation simulated based on data obtained from MRI.

4. The effect of interaction between blood and internal LV wall cavity.

5. The effect of surrounding organs and tissues on heart deformation.

However, these models are limited in important ways, including:

1. Simplified LV geometry.

2. Incomplete understanding of some heart diseases.

3. The models' inability to study the effects of electrical activation, blood flow, porous medium and cardiac metabolism.

4. The measured data taken for a healthy human heart "ideal proband."

5. More realistic mechanical properties of LV tissue are still needed.

These limitations and weaknesses can serve as a basis for future model improvements.

CHAPTER 5: FINITE ELEMENT SIMULATION RESULTS

5.1 Introduction

The current chapter introduces the simulation results of different mesh densities to help choose the FE model most suitable to complete the proposed study. The remainder of the chapter contains the simulation results for two different FE approaches of the human LV. The first approach is aimed to study the effects of myocardial fiber architecture on LV function using the direct FE method. The influence of different myofiber volume fractions and various sets of myofiber orientation on LV function is especially assessed (see sections 5.3 and 5.4). The stress and deformation pattern of the LV model at the end of diastole is also provided using the direct FE method in section 5.5. The second approach is intended to determine, in *vivo*, the myocardial tissue bulk modulus during a cardiac cycle using the inverse FE method. Therefore, the simulation results of myocardial tissue compressibility and hence the bulk modulus ($Compressiblity = \frac{1}{Bulk\ modulus}$) are presented in sections 5.6 and 5.7, respectively.

5.2 Mesh size sensitivity analysis

FE discretization using fine meshes gives results that are more accurate; however, the resulting model can become excessively large, increasing solution and processing time. There is often a tradeoff between the accuracy resulting from a refined model versus the time it takes for analysis and data processing. Therefore, it is advantageous to perform mesh sensitivity analyses to select an adequate yet reasonable level of mesh refinement capable of predicting various response parameters. Four different FE mesh configurations with 3, 5, 7 and 9 layers (one element per layer) through the wall thickness were utilized for this purpose. The 2 myofiber inclination angles, namely helix angle (β) and transverse angle (η) vary

continuously across the LV wall thickness, which is divided throughout the layers (Figure 5.1).
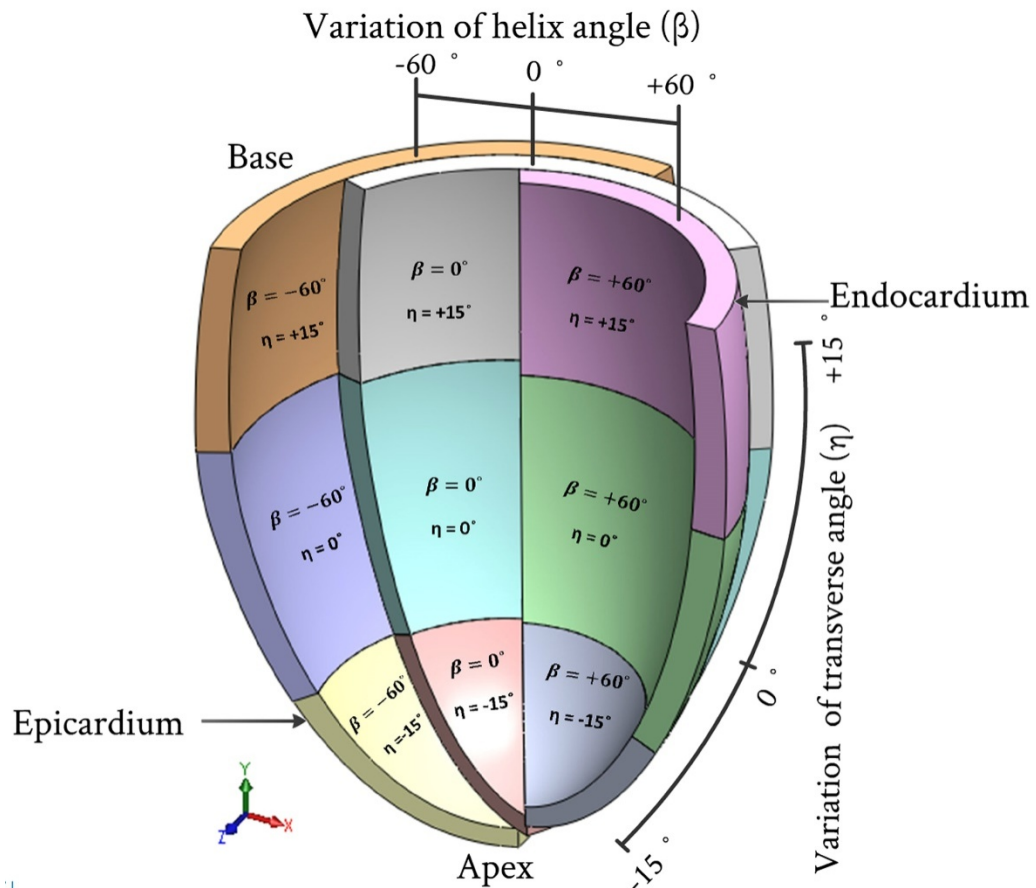
Figure 5.1: Variations in helix angle (β) and transverse angle (η) through the LV wall thickness (for simplicity a 3-layer model is presented)

Figure 5.2 shows a comparison of the obtained FE results for pressure-volume (PV) loops using four different mesh densities. Table 5.1 summarizes the effect of mesh size on time required for solution and maximum error of LV internal cavity volume. The maximum differences in LV internal volumes among 7 layers and 9 layers through the wall thickness mesh was less than 2% ($\approx$1.8%). Furthermore, mesh refinement increased the computation time and may produce a negligible difference in results. Therefore, the mesh density of 22,080 elements (7 layers through wall thickness mesh) would be adequate from the viewpoints of efficiency, computational time costs, mesh distortion, and accuracy.
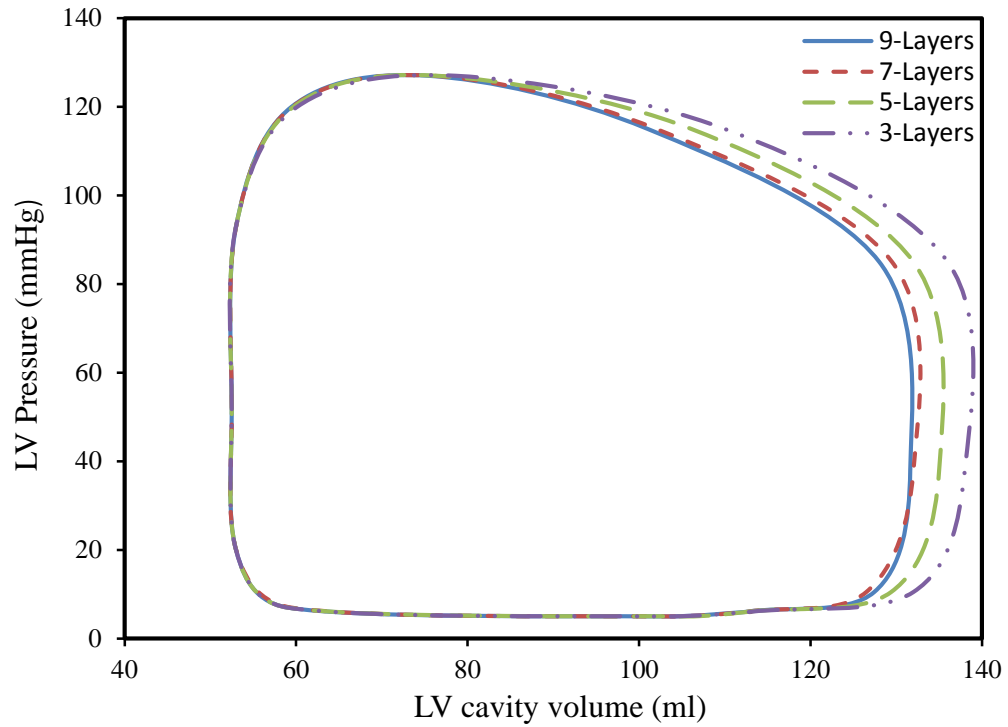
Figure 5.2: Comparison for PV loops obtained from FE simulation using different mesh sizes

Table 5.1: Comparison of mesh size sensitivity

Model	No. of elements	Time required to solve (min)	Maximum error on LV cavity (%)
3-Layers	8064	6	7
5-Layers	11521	11	5.1
7-Layers	22080	18.5	2.9
9-Layers	28388	30	1.1

5.3   Effect of myofiber volume fraction

To investigate the effect of total myofiber volume fraction $\varnothing_{tot}$ on cardiac cycle behavior, LV simulation models with different sets of values for $\varnothing_{tot}$ were performed. A parametric study on the effects of $\varnothing_{tot}$ with the values of 60%, 70%, 80%, and 90% was done. Figure 5.3 and Figure 5.4 display comparisons of the obtained FE results for the LV internal volumes versus time and PV loops using the adopted values of myofiber volume fractions. It is evident that the corresponding ejection fractions (EF) when using LV models with $\varnothing_{tot}$ of 60%, 70%, 80%, and 90% were 50%, 52%, 54% and 57% respectively. Clearly, the EF decreased with decreasing $\varnothing_{tot}$. Finally, the above results confirm that myocardial infarction, which causes damage to the myocardium with a decreasing total number of effective myofibers, impairs the heart's ability to eject blood and therefore diminishes EF.
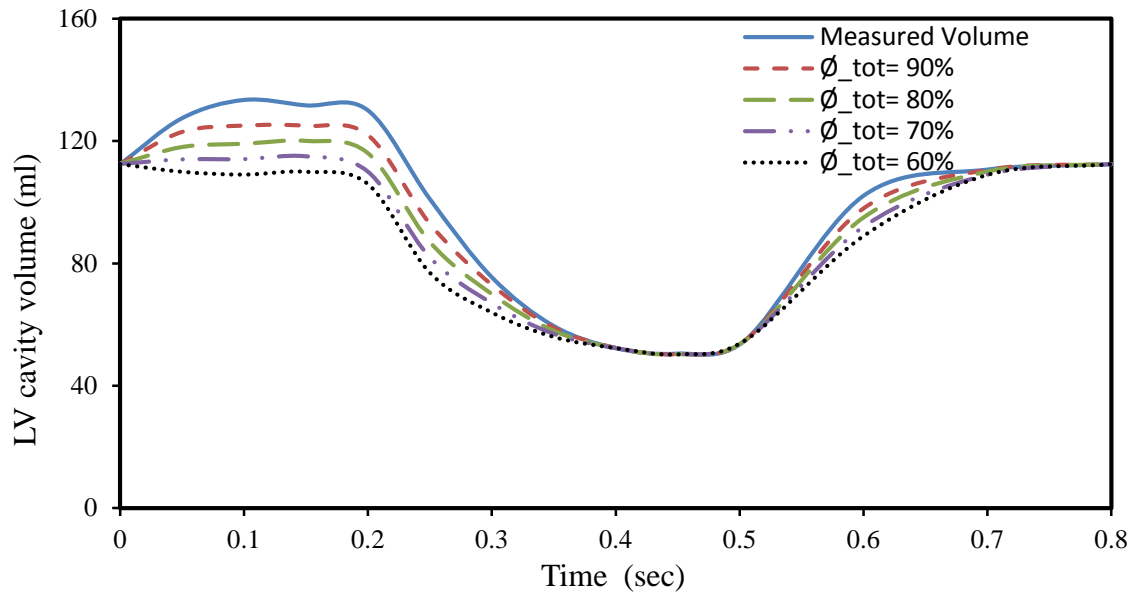
Figure 5.3: Comparison between the LV volumes obtained from FE simulation for using different total myofiber volume fractions $\varnothing_{tot}$
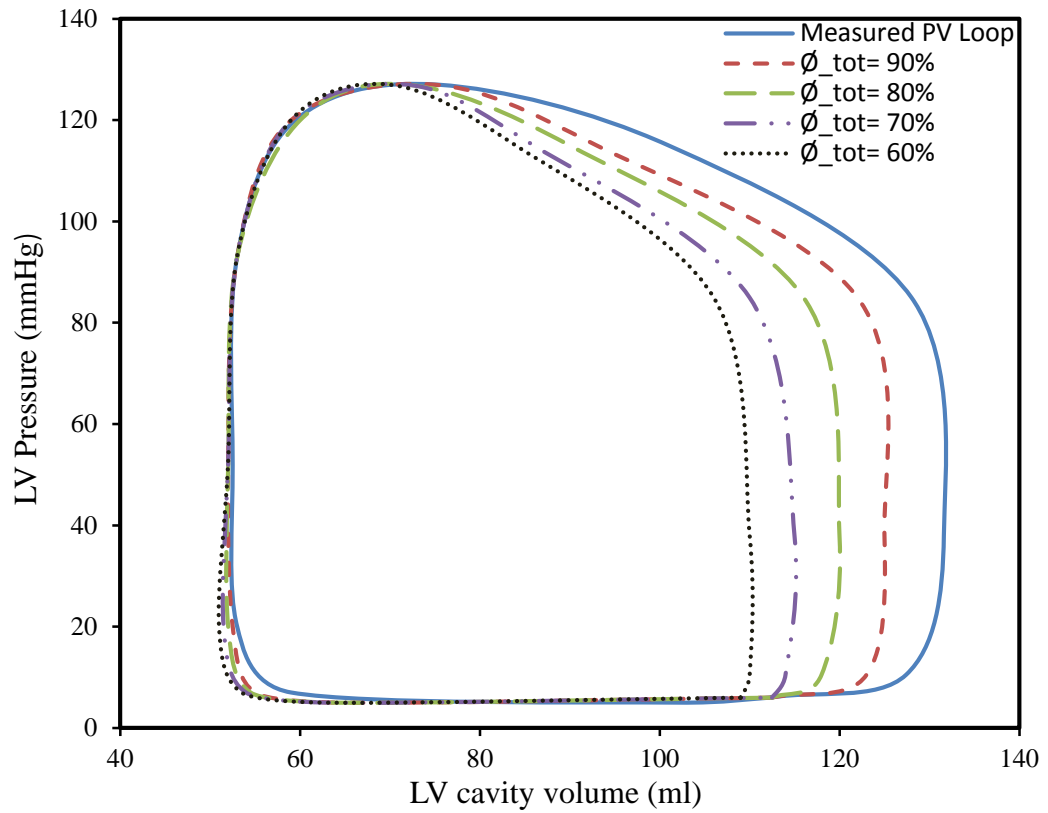
Figure 5.4: Comparison between PV loops obtained from FE simulation when using different total myofiber volume fractions $\varnothing_{\text{tot}}$

5.4 Effect of myofiber orientations

To study the effect of transverse angle (η) on the volume-time response during the cardiac cycle, LV simulation models with diverse sets of values for η were performed. Four different sets were employed: the first set had transmural variation $\eta = -15^{\circ}$ at the apex through 0° at the equatorial level to $+15^{\circ}$ at the base, and the other three sets had constant values of $\eta = -15^{\circ}$, 0°, and $+15^{\circ}$ all throughout the LV wall. The FE analysis results for the LV internal volumes vs. time and PV loops are given in Figure 5.5 and Figure 5.6 respectively. The changes in myofiber orientation distribution for η hardly affect the LV's volume-time relation.
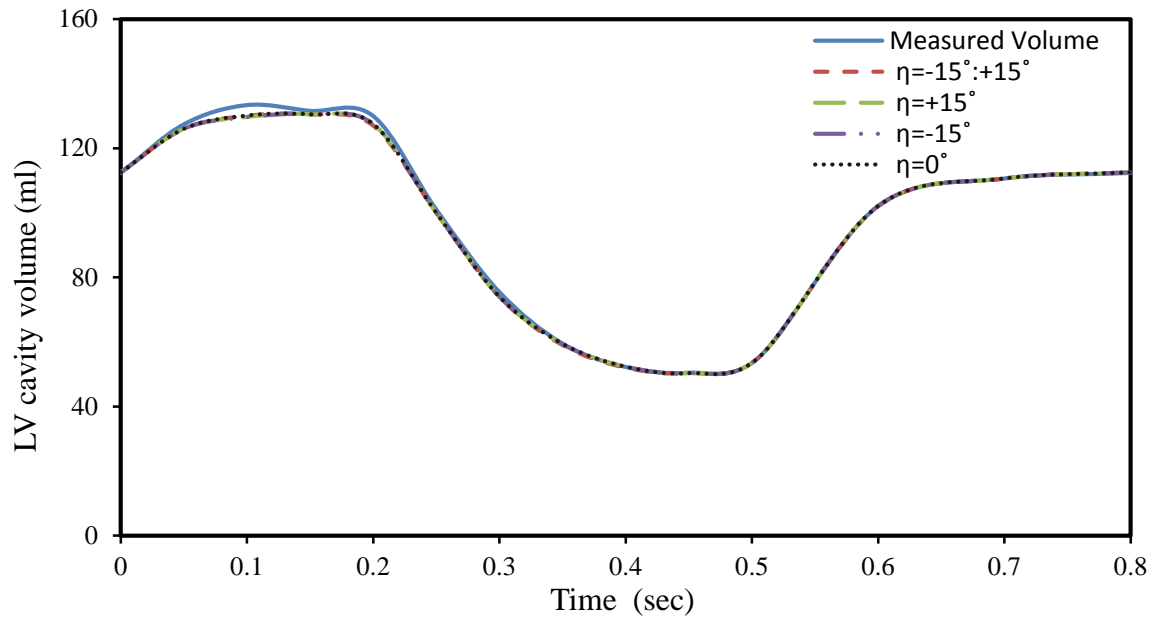
Figure 5.5: Comparison of LV internal volumes obtained from FE simulation using both constant and variable distributions of transverse angle (η)
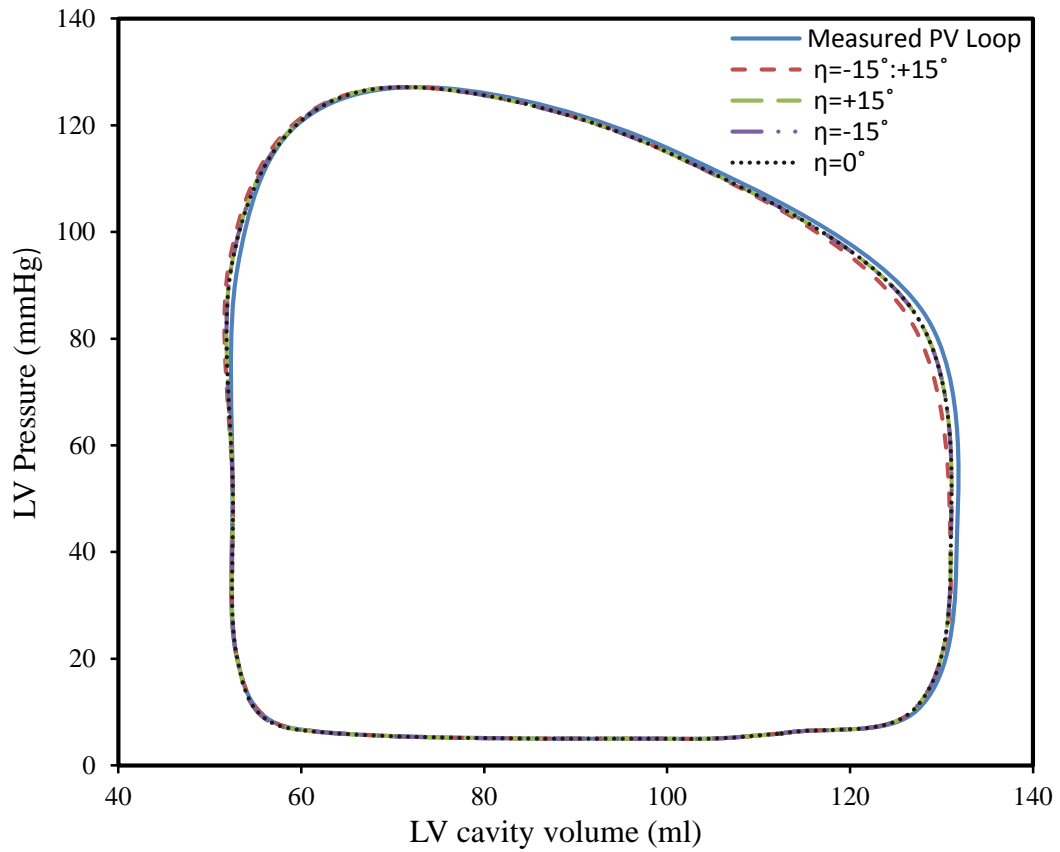
Figure 5.6: Comparison of PV loops obtained from FE simulation using both constant and variable distributions of transverse angle (η)

To examine the effect of helix angle (β) on the volume-time response during the cardiac cycle, LV simulation models using different sets of values for (β) were performed. Three sets of helix inclination angle (β) with constant values of β = -60°, 0°, and +60° all throughout the LV wall were used. The FE results for the LV internal volumes vs. time and PV loops are shown in Figure 5.7 and Figure 5.8 respectively. The obtained FE simulation results for all values of β yield realistic filling and contraction of the LV cavity, except for the first third of diastole and ejection for β = -60° and +60°, where the calculated internal LV volume is higher than experimental measurements. It is also noted that there is a slight difference between the obtained FE results for myofiber distribution (β) = -60° and +60°.
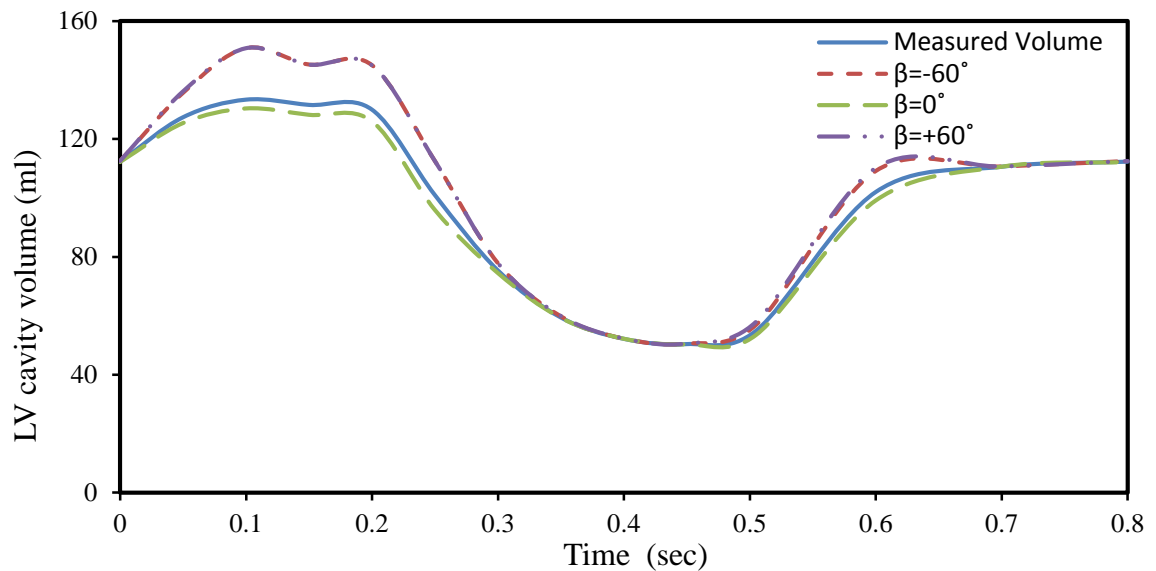
Figure 5.7: Comparison of LV internal volumes obtained from FE simulation using constant distribution of helix angles
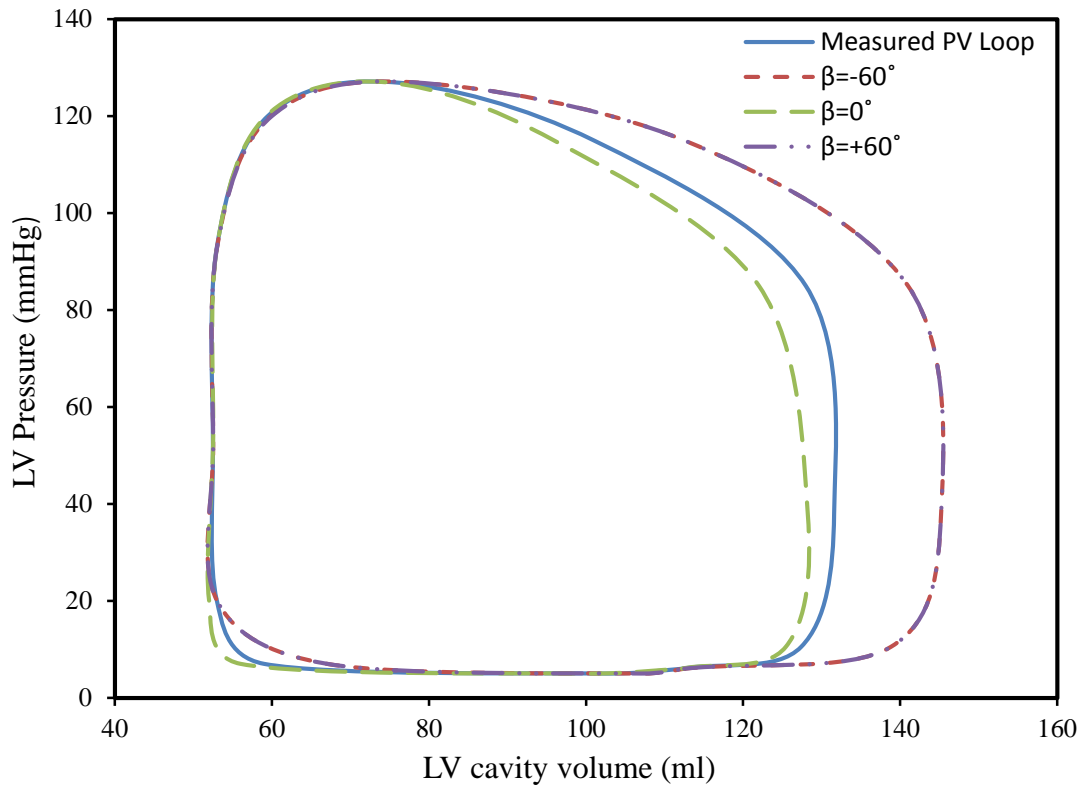
Figure 5.8: Comparison of PV loops obtained from FE simulation using constant distribution of helix angles

To study the effect of non-symmetric helix angle (β) distribution through the LV wall thickness on the volume-time response during the cardiac cycle, two asymmetric distributions (-30°: +60° and -60°: +30°) were used. In the first set, β varied from -30° at the epicardium through a variable angle in the mid-wall layers to +60° at the endocardium; in the second set β varied from -60° at the epicardium through a variable angle in the mid-wall layers to +30° at the endocardium. Figure 5.9 and Figure 5.10 illustrate the comparisons between FE results obtained in case of using the two asymmetric sets (-30°: +60° and -60°: +30°) with the results obtained by using a symmetric set (-60°: +60°). It can be seen that very similar FE results were obtained for both symmetric and asymmetric sets. The calculated values using both systems are also in good agreement with measurement results.
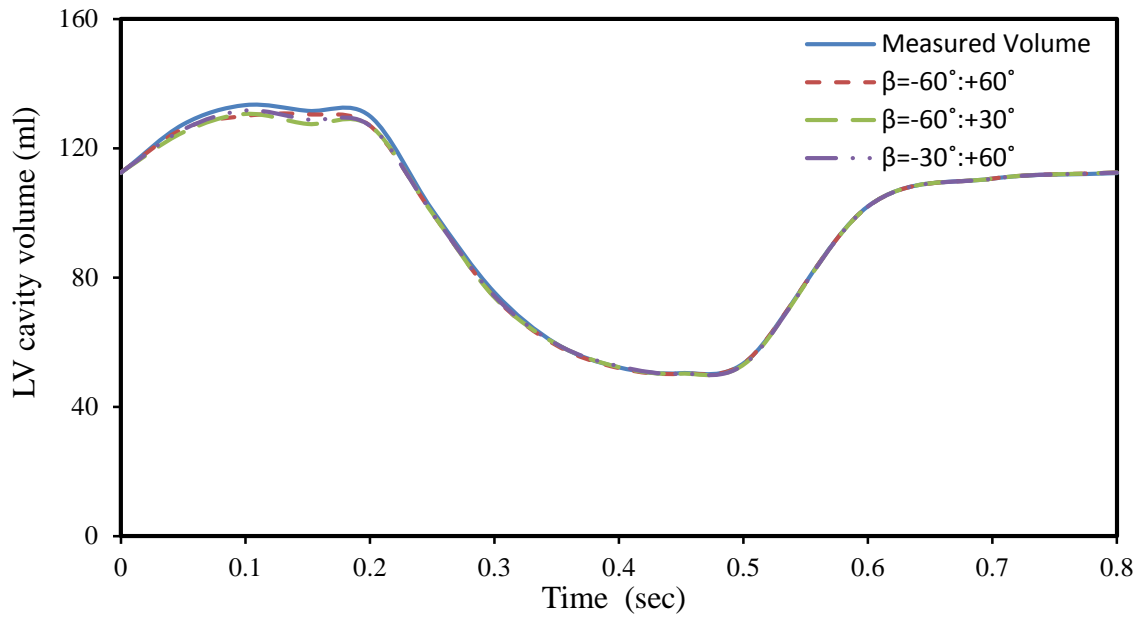
Figure 5.9: Comparison of LV internal volumes obtained from FE simulation using both symmetric and asymmetric helix angle (β) distributions
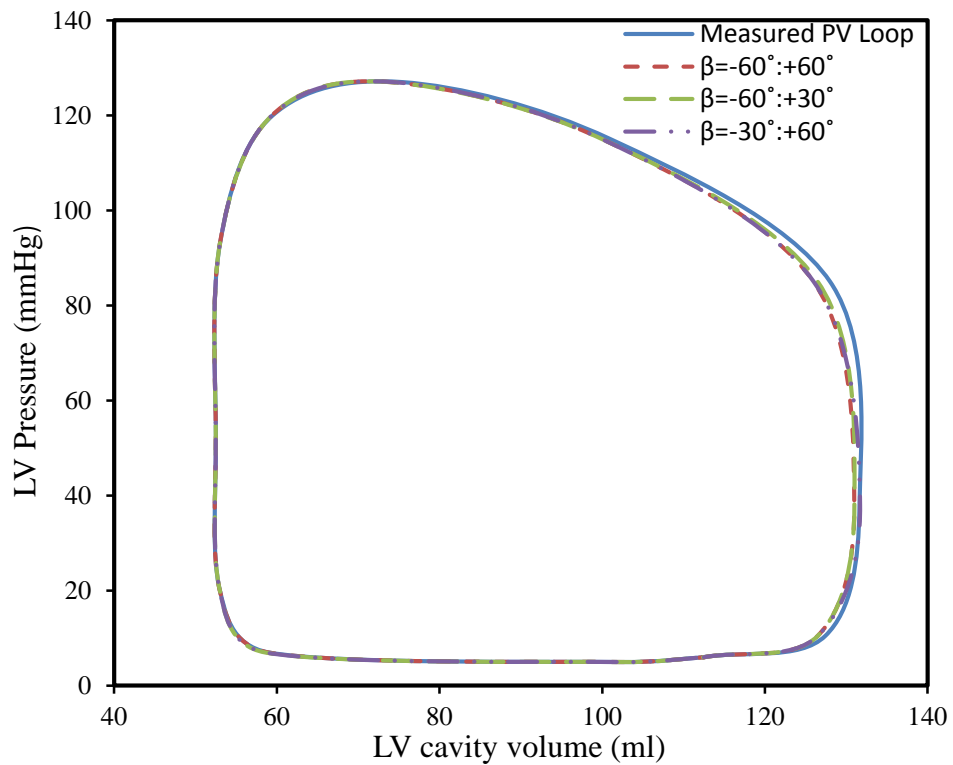
Figure 5.10: Comparison of LV internal volumes obtained from FE simulation using both symmetric and asymmetric helix angle (β) distributions

The effect of complex myofiber orientations based on DT-MRI measurements (Rohmer et al., 2006) on the volume-time response during the cardiac cycle was investigated. Myofibers without inclination angles (no spiral), i.e. longitudinal, radial and circumferential orientations, were also investigated. This means that the transmural myofibers aligned with the cardiac mechanical coordinate axis (Figure 4.4). Figure 5.11 and Figure 5.12 display comparisons between the obtained FEA results for the LV internal volumes vs. time and PV loops using complex myofiber orientations and myofiber without inclination. It is obvious that the oblique myofiber orientation (spiral shape) plays an important role in the cardiac cycle, i.e. fiber orientation greatly influences LV mechanics. In addition, the calculated FE results of LV volumes for longitudinal and radial myofiber orientation distributions were overestimated.
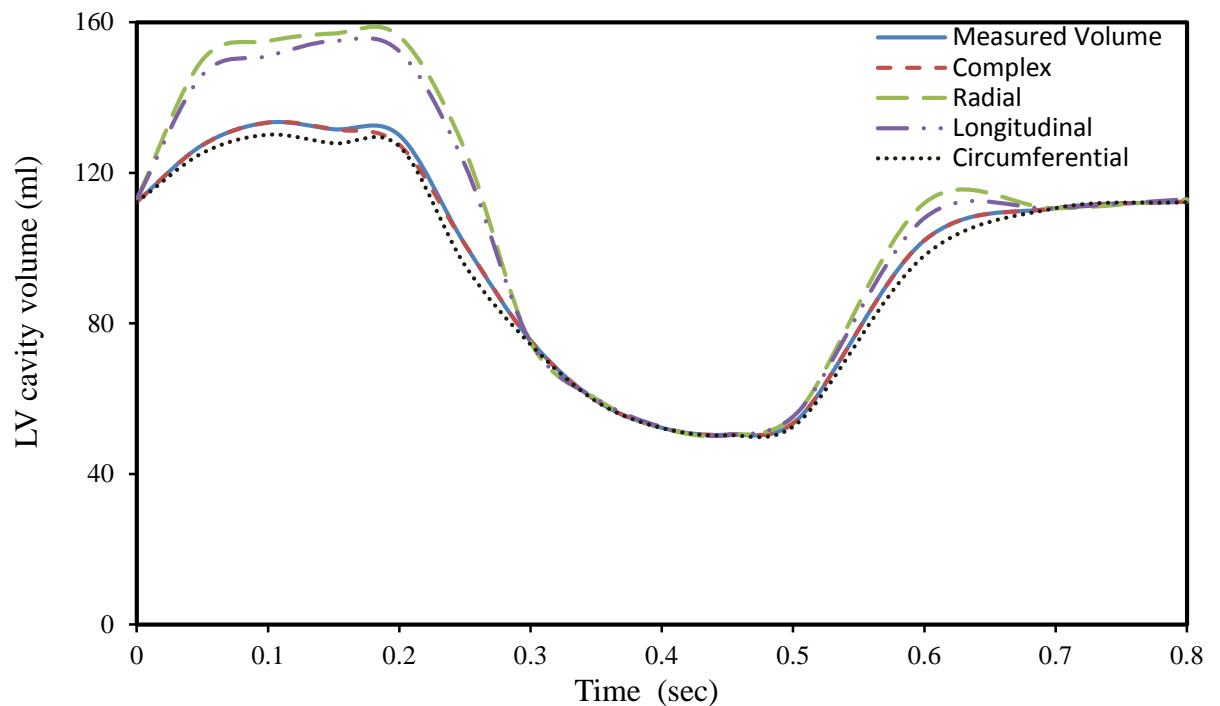
Figure 5.11: Comparison of LV internal volumes obtained from FE simulation using different myofiber orientations
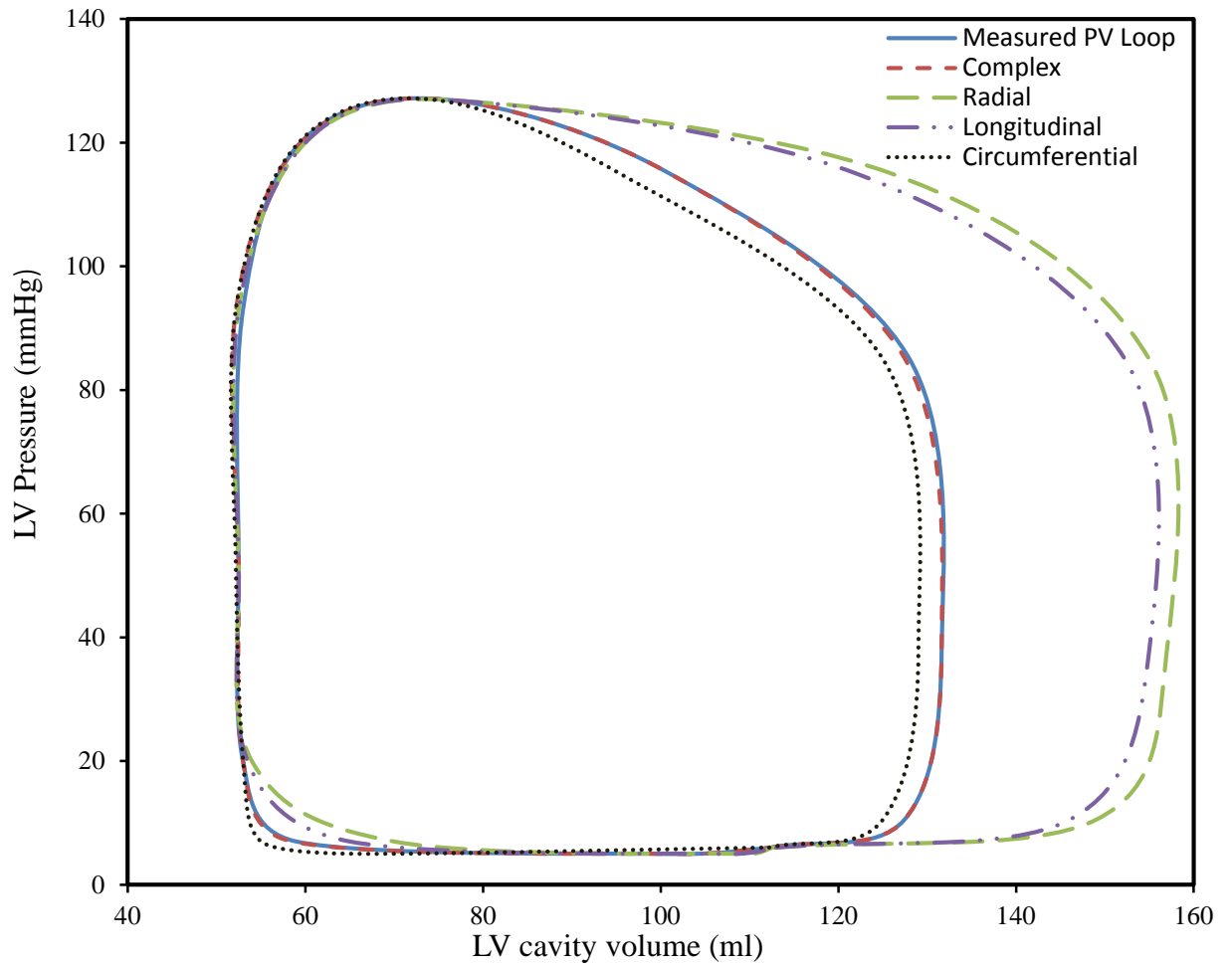
Figure 5.12: Comparison of PV loops obtained from FE simulation using different myofiber orientations

However, the FE results achieved for both complex myofiber and circumferential orientations are in good agreement with the actual measurements. This is in accord with the results achieved in R-squared analysis; the FE data outcome for complex myofiber fits well with the measured points (R-squared value of 74%). The calculated R-squared value for circumferential myofiber was 70%.

5.5   Stress and deformation pattern

Stress and deformation pattern results from FE analyses for the LV model at the end of diastole were evaluated with the distributions and variations of these values through the wall thickness. Figure 5.13(a-d) illustrates the distribution of displacement vector sum, von Mises total strain, von Mises stress, and the maximum shear stresses through the LV wall thickness at the end of diastole. It is visible that the largest value occurs on the endocardium side at the base of the LV wall. With the exception of shear stress the maximum value occurs near the apex, something attributed to apical torsion.

Total Displacement [mm]

12.3648	
11.2818	
10.1989	
9.1159	
8.03292	
6.94995	
5.86697	
4.78399	
3.70102	
2.61804	

Von Mises Total Strain

0.520187	
0.462388	
0.40459	
0.346791	
0.288993	
0.231194	
0.173396	
0.115597	
0.57799	
0	

Von Mises stress [N/mm²]

0.011546	
0.010434	
0.009322	
0.00821	
0.007098	
0.005986	
0.004875	
0.003763	
0.002651	
0.001539	

Shear Stress [N/mm²]

0.003782	
0.002942	
0.002101	
0.001261	
0.420E03	
-0.420E03	
-0.001261	
-0.002101	
-0.002942	
-0.003782	

(a)   (b)   (c)   (d)

Figure 5.13: The contour plots of the deformation and stress distribution through the LV wall at the end of diastole using linear elastic material model (a) displacement vector sum; (b) von Mises total strain; (c) von Mises total stress; and (d) XZ plane shear stress

5.6   Variations of tissue compressibility during one cardiac cycle

During a cardiac cycle, the myocardial wall tissue experiences successive active contraction and relaxation consequent to depolarization and repolarization, respectively. Due to the heart beating and the LV pressure dynamics response, a significant amount of energy is expended to compress the heart wall, essentially squeezing the myocardium cells closer together.

Figure 5.14 shows the FE results for the myocardial tissue compressibility variations throughout one cardiac cycle. It is noticed that the myocardium tissue is nearly incompressible for a short period of time, or about 0.16sec throughout the cardiac cycle (not exceeding 20% of total cardiac cycle time). The tissue exhibits incompressible behavior in the reduced ejection and isovolumic relaxation phases. It is additionally observed that myocardium tissue compressibility decreases rapidly at the beginning of the rapid ejection phase. Subsequently, myocardium tissue compressibility gradually increases in the rapid filling phase and remains nearly constant during reduced filling, followed by a further increase during atrial systole (roughly 30% increase of the maximum tissue compressibility). The difference between the maximum myocardial tissue compressibility of 3kPa^{-1} and minimum value of $\approx 0 \text{ kPa}^{-1}$ may be a good index for normal ventricular function. A decrease in this value means abnormal cardiac function occurrences, perhaps due to myocardial infarction or heart dysfunction. The myocardial tissue compressibility increases with decreasing ventricle contractile force. This leads to an increase in LV cavity size, meaning that the heart cannot pump blood efficiently and structural alterations of the myocardium occur (i.e. the heart is enlarged and its pumping ability is impaired). Hence, the myocardial tissue compressibility should be considered if myocardial performance, myocardial deformation, and heart wall stresses, response time is critical.
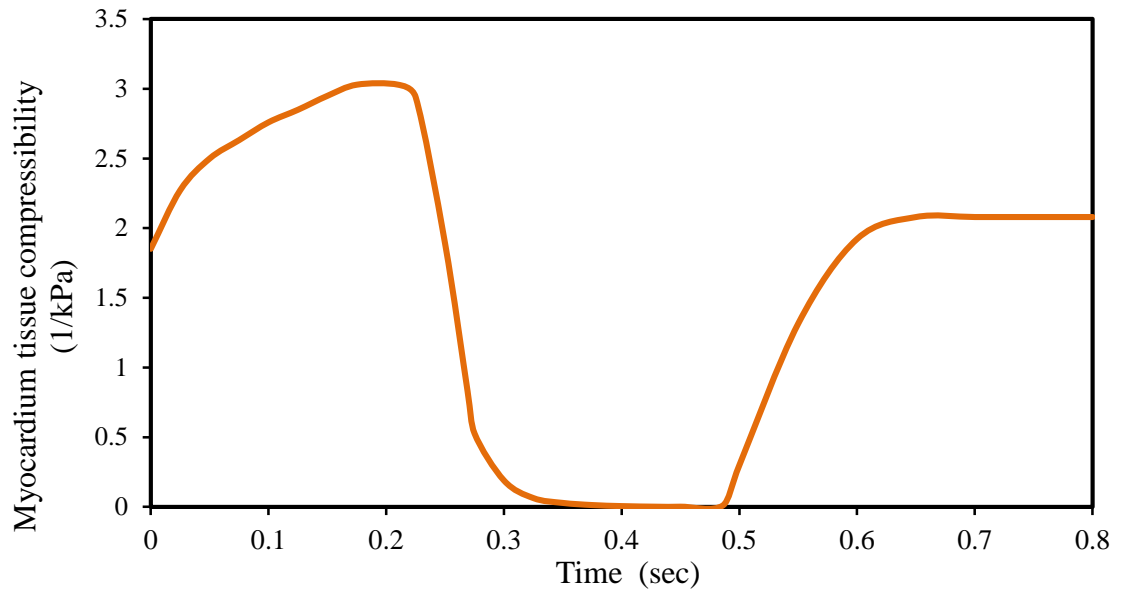
Figure 5.14: FE-computed myocardial tissue compressibility during one cardiac cycle vs. time

5.7 Variations of bulk modulus during one cardiac cycle

Figure 5.15b presents the FE results for the variations in myocardial bulk modulus during one cardiac cycle. Large variations occurred during the rapid ejection and isovolumic relaxation phases. The myocardial bulk modulus reached a maximum value at the end of ejection and began to decline at the beginning of isovolumic relaxation, i.e. the LV wall tissue was stiffened by contraction and softened by relaxation. Evidently, the myocardial bulk modulus increased exponentially during the ejection phase until a peak value, followed by a linear decrease in isovolumic relaxation phase (i.e. the myofibrils returned to their original length). The peak, bulk modulus value occurred at 0.43sec and the bulk modulus duration changed from 0.3sec to 0.5sec.
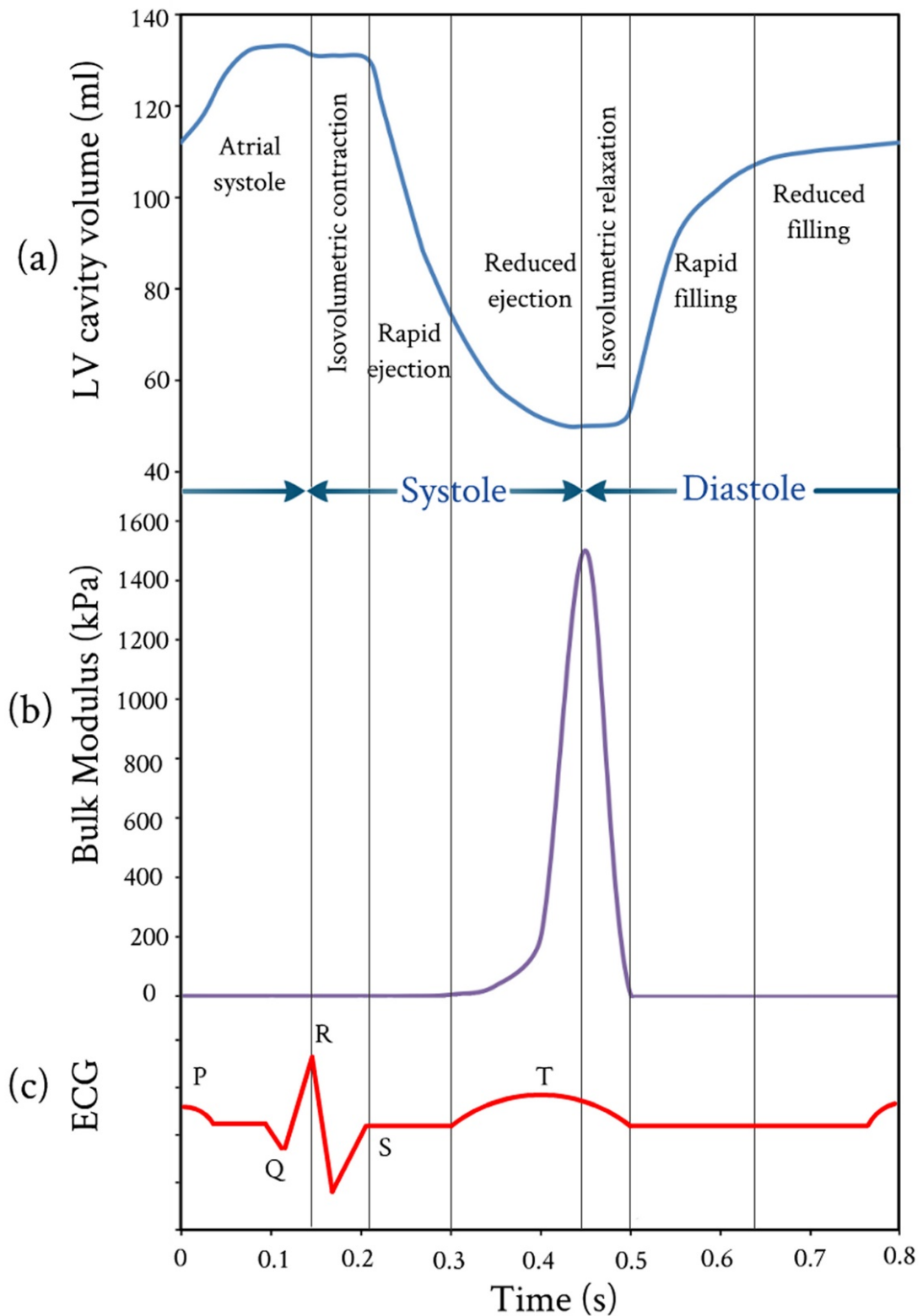
Figure 5.15: (a) FE-computed LV cavity ventricular volume; (b) FE-computed myocardial tissue bulk modulus during one cardiac cycle vs. time; (c) Accompanying ECG during one cardiac cycle vs. time

With regard to timing, the computed durations for bulk modulus changes were compared with the ECG for one cardiac cycle (Figure 5.15c). It is observed that the durations for the onset and ending of LV repolarization marked by T wave (on surface ECG) agree very well with the onset and ending durations of bulk modulus changes (Figure 5.15c). It is also clear that the onset and ending times of LV repolarization from 0.3sec to 0.5sec are sharply defined. Actually, the electrical signals were not included in the present FE analysis, but their impact partook in the present FE model by introducing myofiber active elastance. Figure 5.15a-c displays a good correlation (synchronization) between the instantaneous variation in myocardial tissue bulk modulus and the onset and ending of LV repolarization (T wave).

CHAPTER 6: DISCUSSION AND COMPARISONS

6.1   Introduction

The overarching aim of this work was to develop a 3D model of a beating LV based on an accurate description of both muscle fiber orientation and mechanical properties. The model served to study the influence of myofiber architecture on the mechanics of LV function (using the direct FE method) and to predict, in *vivo*, the myocardial bulk modulus during the various phases of the cardiac cycle (using the inverse finite element method).

The parametric study with the direct FE method showed that the myofiber architecture, particularly the myofiber volume fraction and myofiber orientation, significantly influences LV function mechanics and hence the orthotropic mechanical properties of cardiac muscle.

The inverse FE method demonstrated that the predicted myocardial bulk modulus may be used as a clinical diagnostic tool of heart diseases.

In order to present a more balanced discussion, this chapter provides comparisons between our work and experimental measurements or works from other groups on the proposed direct and inverse FE methods.

6.2   Comparison of internal cavity volume using different material models

In order to check the validity of our model, two different constitutive models were employed using the direct FE method. The first was the three-term Ogden model according to (Bettendorff-Bakman et al., 2006) (Table 6.1) and the second was the two-term Ogden model following (Ghaemi et al., 2009a; Ghaemi et al., 2009b) (Table 6.2).

Table 6.1: Three-term Ogden parameter values employed by (Bettendorff-Bakman et al., 2006)

Parameter	Value	Unit
μ_1	-0.03	kPa
μ_2	0.0014	kPa
μ_3	-0.05	kPa
α_1	-45	—
α_2	38.07	—
α_3	-14	—

Table 6.2: Two-term Ogden parameter values used by (Ghaemi et al., 2009a; Ghaemi et al., 2009b)

Parameter	Value	Unit
μ_1	9.99	kPa
μ_2	6.36	kPa
α_1	2.4	—
α_2	2.4	—

Figure 6.1 and Figure 6.2 provide comparisons between the calculated LV internal volumes versus time and PV loops using different material models. It is clear that the stroke volume (SV) values of the constitutive models obtained by (Bettendorff-Bakman et al., 2006) and (Ghaemi et al., 2009a; Ghaemi et al., 2009b) are small compared to the measured values. Also, it can be seen that the material parameters obtained from our model (Hassan et al., 2012) are in good agreement with the measurements.
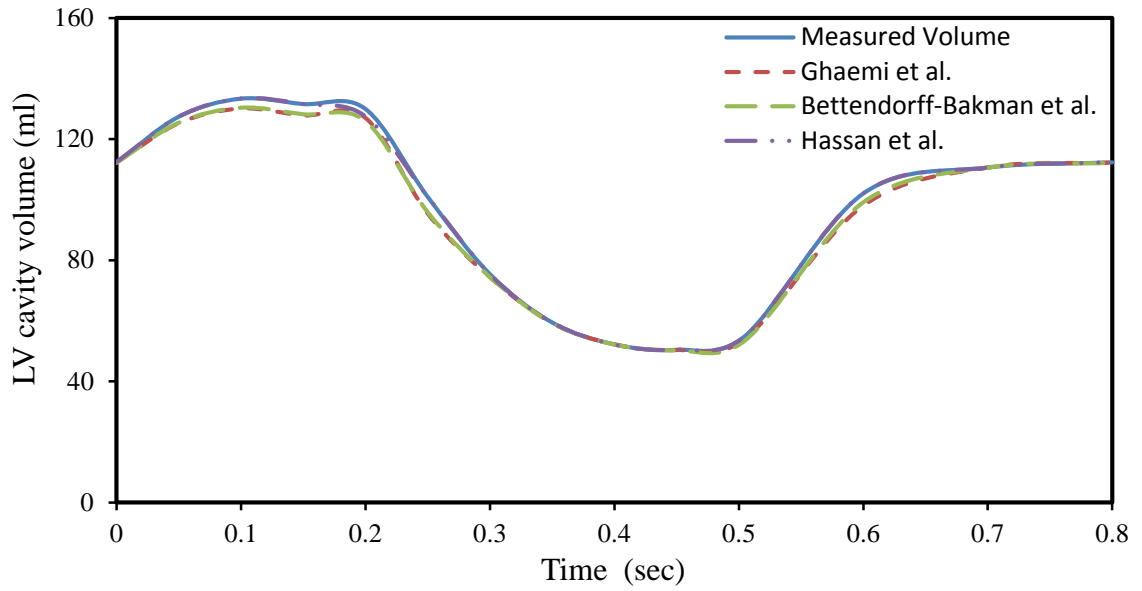
Figure 6.1: Comparison of LV internal volumes obtained from FE simulation using different constitutive models
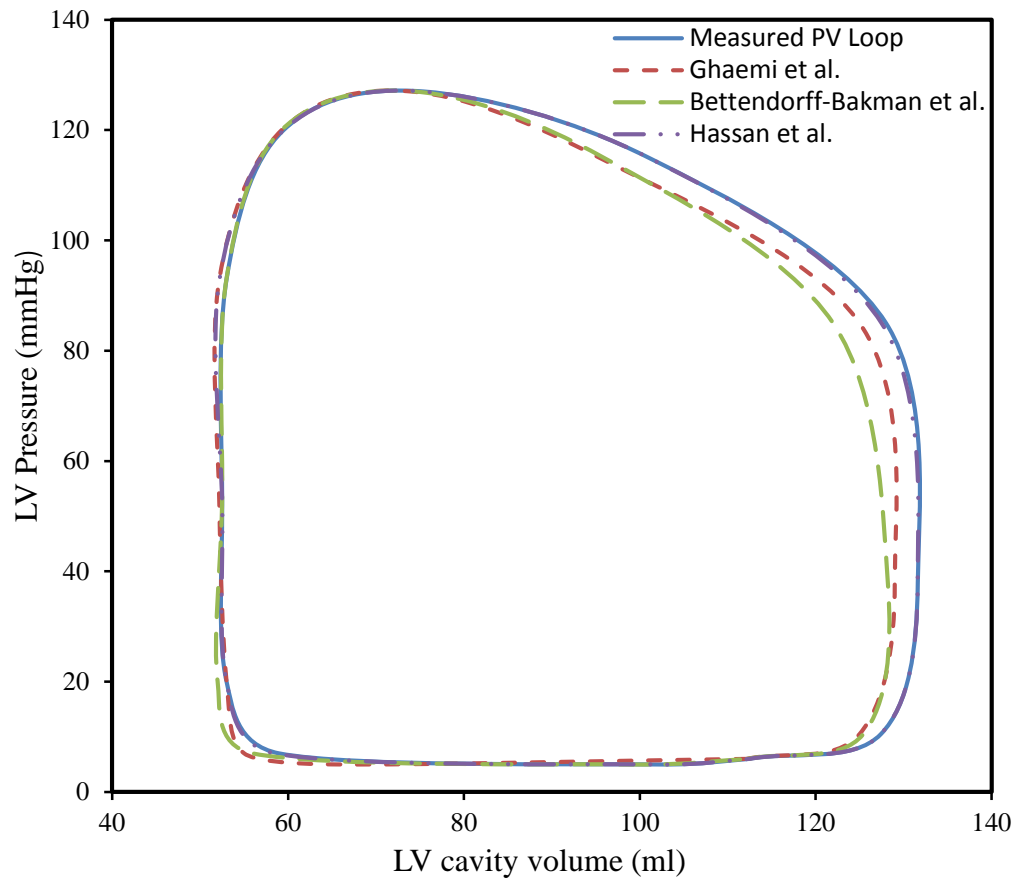
Figure 6.2: Comparison of PV loops obtained from FE simulation using different constitutive models

6.3   Comparison between inverse simulation and experimental cavity volumes

Figure 6.3 depicts the comparison between the predicted FE and experimentally measured LV cavity volumes using the inverse FE method. Obviously, the inverse FE model can accurately predict the change in LV cavity volume during a cardiac cycle. The LV volume change continuously throughout the cardiac cycle and the various events (cardiac cycle phases) can be predicted.
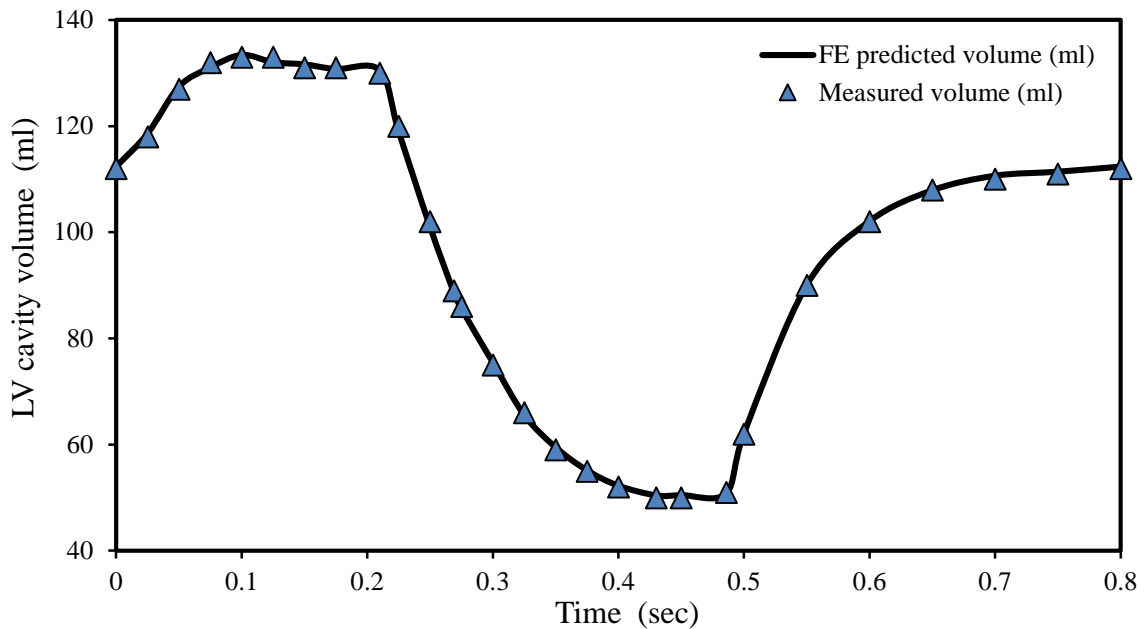
Figure 6.3: Comparison between the FE predicted LV cavity volume and experimentally measured data

The LV cavity volumes increased rapidly from 110ml to 130ml (end diastolic volume EDV = 130ml) shortly after the beginning of atrial systole phase until 0.1sec. Then the LV cavity volume remained constant during the isovolumic contraction phase until 0.21sec. Subsequently a sudden decrease in LV cavity volume is evident at the onset of the rapid ejection phase until 0.3sec, followed by a slight decrease during the reduced ejection phase until 0.43sec in the end systolic phase. The size of LV cavity volume at the moment was

equal to that at the end systolic volume (ESV = 50 ml). The LV cavity volume remained constant during the isovolumic relaxation phase until 0.5sec, followed by a rapid increase during the rapid filling phase until 0.65sec. Finally, the LV volume slightly increased during the reduced filling phase up to the end of the cardiac cycle.

6.4   Comparison between predicted FE bulk modulus and ejection fraction

The predicted myocardial bulk modulus (K) and ejection fraction (EF) were compared using the inverse FE method. Four different LV pressure-volume diagrams with different sets of physiological conditions were employed, as seen in Figure 6.4a, b. The initial LV cavity volumes of the models were 50ml, 50ml, 65ml, and 70ml for Model_1, Model_2, Model_3, and Model_4 respectively, while the LV wall thickness was kept constant as described in Figure 4.1. Figure 6.4c indicates the variations in predicted myocardial bulk modulus during one cardiac cycle. There is a discrepancy among the peak values of myocardial bulk moduli: 1500kPa, 2855kPa, 4760kPa, and 8000kPa, corresponding to ejection fractions of 61.5% (Hall, 2011), 58.3% (Klabunde, 2011), 56.3% (Courneya & Parker, 2010) and 53.6 % (Stouffer, 2011) respectively.

Figure 6.5 shows the variations in maximum bulk modulus versus ejection fraction. It is clear that the ejection fraction increased with decreasing peak myocardial bulk modulus values. Such decrease (i.e. increasing myocardial tissue compressibility) caused an increase in myocardial contraction, which led to an increased heart ejection fraction. Further studies are still required to verify the correlation among the myocardial tissue bulk modulus as a marker for heart function, strain and strain rate. Finally, the above results confirm the hypothesis in computing the active myofiber Young's modulus and inverse FE analysis usage to determine the myocardial tissue bulk modulus.
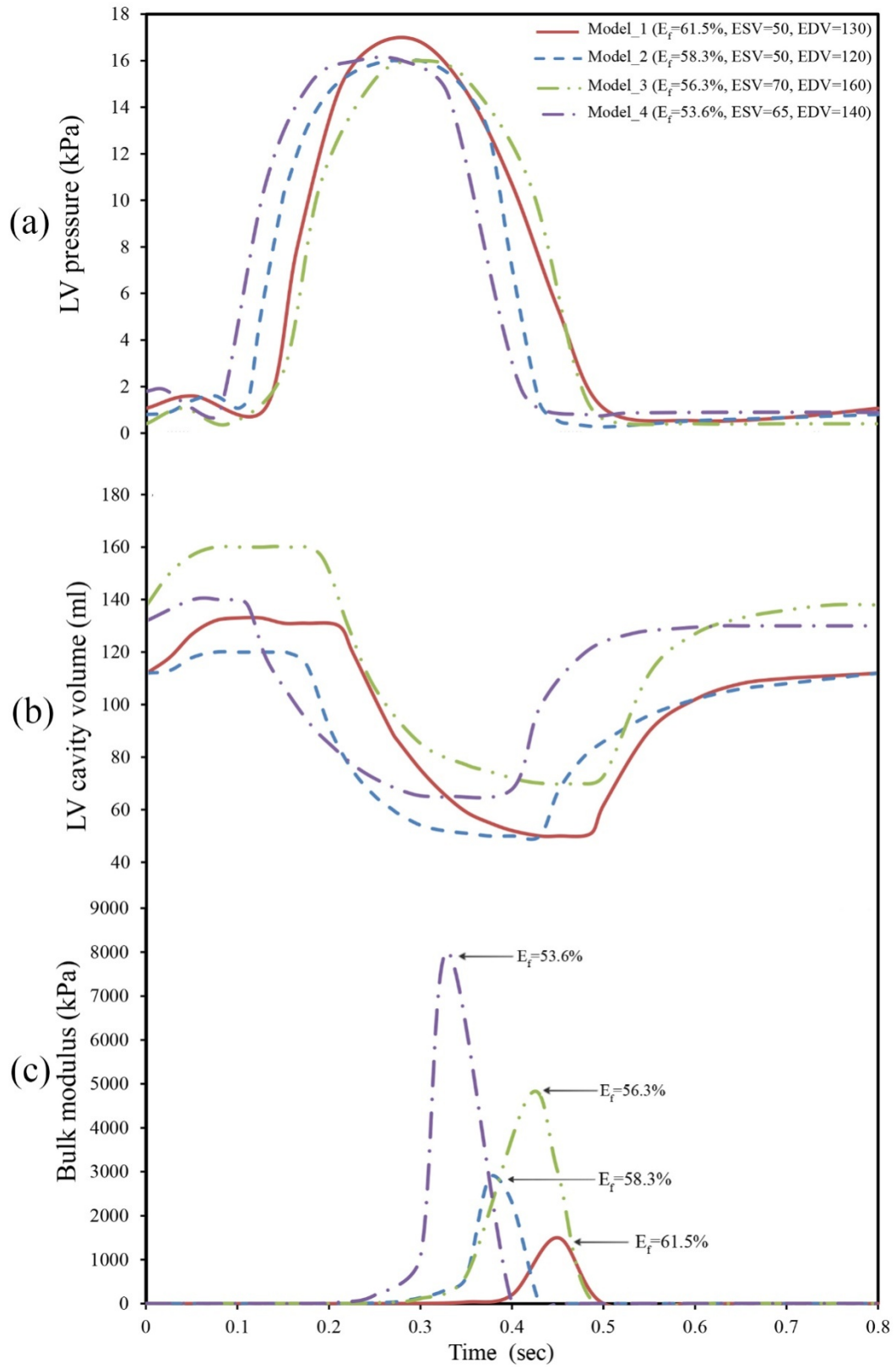
Figure 6.4: (a) Measured LV pressures vs. time for two different cardiac cycles; (b) Measured LV cavity volumes vs. time; (c) FE computed myocardial tissue bulk modulus vs. time
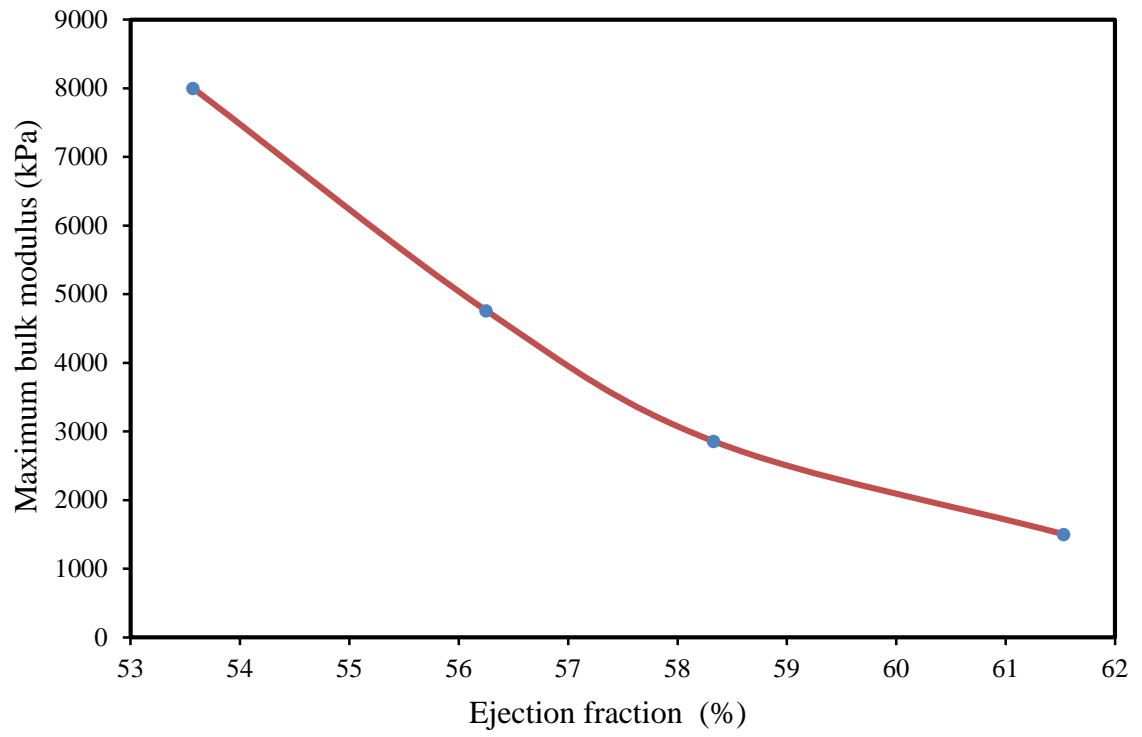
Figure 6.5: Comparison between the FE predicted maximum bulk modulus and ejection fraction

CHAPTER 7: CONCLUSIONS AND RECOMMENDATIONS

7.1   Conclusion

In the present study, the human LV wall was modeled as a thick-walled ellipsoid truncated at two-thirds of the major axis with spatial myofiber angle distribution. The ellipsoidal geometry was selected for modeling the human LV for it closely resembles real anatomical shape and is quite simple. The model was designed to present a sensitivity study of cardiac mechanics with respect to myocardial fiber architecture using a direct FE model of the human LV (Hassaballah et al., 2014). Meanwhile, an inverse FE model of a human LV was used to determine the myocardial bulk modulus during the cardiac cycle (Hassaballah et al., 2013). Based on the results and discussion presented in the preceding section, the following conclusions can be drawn:

1. The oblique orientation of myofibers plays an important role in both systolic deformation and early diastolic function.

2. The transverse angle (η) has little effect on the human LV function during the cardiac cycle.

3. The myofiber volume fraction and fiber orientation greatly influence LV mechanics during the cardiac cycle.

4. Simulation results are more sensitive to changes in helix angle (β) than to transverse angle (η) changes.

5. The myocardial bulk modulus can serve as a diagnostic tool (clinical indicator) of heart ejection fraction.

6. According to the simulation results, the present FE model is sensitive to the overall cardiac function parameters expressed in terms of LV pressure-volume variations during cardiac cycle and ejection fraction.

7. The calculations of active myofiber Young's modulus (myocardium's active properties) based on LV pressure proved to be correct.

7.2   Recommendation

Several areas still require further investigation and potential improvements, as follows:

1. It is vitally important to use MRI data including a reasonably accurate description of real geometry and myofiber orientation.

2. The data used in this analysis was taken assuming a healthy heart "ideal proband" and this is quite weak to draw any significant conclusions. It is necessary to establish a database with information from normal hearts at different developmental stages and from pathological hearts through disease progression.

3. The greatest challenge is to develop a model correlating cardiac function-electrical activation of the myocardium, soft tissue myocardial mechanics, ventricle fluid mechanics, and coronary flow.

REFERENCES

Aaronson, P. I., Ward, J. P., & Connolly, M. J. (2012). *The cardiovascular system at a glance*: Wiley. com.

Alpert, N. R. (1971). *Cardiac hypertrophy*: Academic Press.

American Heart Association, I. (2013). American Heart Association. *Risk factors and Coronary Heart Disease* from http://www.heart.org/HEARTORG/

Anversa, P., & Sonnenblick, E. H. (1990). Ischemic cardiomyopathy: pathophysiologic mechanisms. *Progress in Cardiovascular Diseases, 33*(1), 49.

Arts, T., Lumens, J., Kroon, W., & Delhaas, T. (2012). Control of Whole Heart Geometry by Intramyocardial Mechano-Feedback: A Model Study. *PLoS Comput Biol, 8*(2), e1002369. doi: 10.1371/journal.pcbi.1002369

Atkin, R. J., & Fox, N. (1980). *An introduction to the theory of elasticity* (Vol. 14): Longman London.

Augenstein, K. F., Cowan, B. R., LeGrice, I. J., & Young, A. A. (2006). Estimation of cardiac hyperelastic material properties from MRI tissue tagging and diffusion tensor imaging *Medical Image Computing and Computer-Assisted Intervention–MICCAI 2006* (pp. 628-635): Springer.

Bagnoli, P., Malagutti, N., Gastaldi, D., Marcelli, E., Lui, E., Cercenelli, L., Fumero, R. (2011). Computational finite element model of cardiac torsion. *International Journal of Artificial Organs, 34*(1), 44-53. doi: Doi 10.5301/Ijao.2011.6313

Beecham, M. (1997). Finite element analysis of the human left ventricle in diastole and systole *Brunel University School of Engineering and Design PhD Theses*.

Bekeredjian, R., & Grayburn, P. A. (2005). Valvular Heart Disease. *Circulation, 112*(1), 125-134.

Berne, R., & Levy, M. (1996). Principles of physiology. Mosby-Year Book. *Inc., St. Loius, Missouri*.

Bettendorff-Bakman, D. E., Schmid, P., Lunkenheimer, P., & Niederer, P. (2006). A finite element study relating to the rapid filling phase of the human ventricles. *Journal of theoretical biology, 238*(2), 303-316.

Bettendorff-Bakman, D. E., Schmid, P., Lunkenheimer, P., & Niederer, P. (2008). Diastolic ventricular aspiration: A mechanism supporting the rapid filling phase of the human ventricles. *Journal of Theoretical Biology, 250*(4), 581-592.

Beyar, R., Yin, F., Hausknecht, M., Weisfeldt, M. L., & Kass, D. A. (1989). Dependence of left ventricular twist-radial shortening relations on cardiac cycle phase. *American Journal of Physiology-Heart and Circulatory Physiology, 257*(4), H1119-H1126.

Bogaert, J., Dymarkowski, S., & Taylor, A. (2005). Coronary Artery Disease. *Clinical Cardiac MRI*, 381-437.

Bonow, R. O., Mann, D. L., Zipes, D. P., & Libby, P. (2011). *Braunwald's Heart Disease: A Textbook of Cardiovascular Medicine, 2-Volume Set*: Elsevier Health Sciences.

Bovendeerd, D., Arts, T., Huyghe, J., Campen, D., & Reneman, R. (1991). The mechanics of the ischemic left ventricle during the cardiac cycle. *Advances in Bioengineering, ASME, 26*, 651-654.

Bovendeerd, P., Arts, T., Huyghe, J., Van Campen, D., & Reneman, R. (1992). Dependence of local left ventricular wall mechanics on myocardial fiber orientation: a model study. *Journal of Biomechanics, 25*(10), 1129-1140.

Bovendeerd, P., Huyghe, J., Arts, T., Van Campen, D., & Reneman, R. (1994). Influence of endocardial-epicardial crossover of muscle fibers on left ventricular wall mechanics. *Journal of Biomechanics, 27*(7), 941-951.

Burch, G., Ray, C., & Cronvich, J. (1952). The George Fahr Lecture: Certain mechanical peculiarities of the human cardiac pump in normal and diseased states. *Circulation, 5*(4), 504-513.

Burton, A. C. (1957). The importance of the shape and size of the heart. *American Heart Journal, 54*(6), 801-810. doi: http://dx.doi.org/10.1016/0002-8703(57)90186-2

Carter, D., Greenson, J. K., Oberman, H. A., Reuter, V. E., & Stoler, M. H. (2004). *Sternberg's diagnostic surgical pathology* (Vol. 1): Lippincott Williams & Wilkins.

Chandler, T. J., & Brown, L. E. (2008). *Conditioning for strength and human performance*: Lippincott Williams & Wilkins.

Chen, J., Liu, W., Zhang, H., Lacy, L., Yang, X., Song, S. K., Yu, X. (2005). Regional ventricular wall thickening reflects changes in cardiac fiber and sheet structure during contraction: quantification with diffusion tensor MRI. *American Journal of Physiology-Heart and Circulatory Physiology, 289*(5), H1898-H1907.

Clark, R. K. (2005). *Anatomy and physiology: Understanding the human body*: Jones & Bartlett Learning.

Cosin Aguilar, J. A., Hernandiz Martinez, A., Tuzon Segarra, M. T., Aguero Ramon-Llin, J., & Torrent-Guasp, F. (2009). Experimental study of the so called left ventricular isovolumic relaxation phase. [Research Support, Non-U S Gov't]. *Rev Esp Cardiol, 62*(4), 392-399.

Costa, K. D., Takayama, Y., McCulloch, A. D., & Covell, J. W. (1999). Laminar fiber architecture and three-dimensional systolic mechanics in canine ventricular myocardium. *American Journal of Physiology-Heart and Circulatory Physiology, 276*(2), H595-H607.

Courneya, C. A. M., & Parker, M. J. (2010). *Cardiovascular Physiology: A Clinical Approach [With Access Code]*: Wolters Kluwer Health.

Davey, P., Wiley, J., & Blackwell, B. (2008). *ECG at a Glance*: Wiley-Blackwell.

Davies, C., Simons, D. G., & Davies, A. (2004). *The trigger point therapy workbook: your self-treatment guide for pain relief*: New Harbinger Publications Incorporated.

Deepa, G. (2012). *Textbook of Anatomy and Physiology for Nurses*: Jaypee Brothers Medical Pub.

Dent, C. L., Scott, M. J., Wickline, S. A., & Hall, C. S. (2000). High-frequency ultrasound for quantitative characterization of myocardial edema. *Ultrasound in medicine & biology, 26*(3), 375-384.

Dorri, F., Niederer, P., & Lunkenheimer, P. (2006). A finite element model of the human left ventricular systole. *Computer Methods in Biomechanics and Biomedical Engineering, 9*(5), 319-341.

Fann, J. I., Sarris, G. E., Ingels Jr, N. B., Niczyporuk, M. A., Yun, K. L., Daughters, G., Miller, D. (1991). Regional epicardial and endocardial two-dimensional finite deformations in canine left ventricle. *American Journal of Physiology-Heart and Circulatory Physiology, 261*(5), H1402-H1410.

Farwell, D., & Gollob, M. H. (2007). Electrical heart disease: Genetic and molecular basis of cardiac arrhythmias in normal structural hearts. *The Canadian journal of cardiology, 23*(Suppl A), 16A.

Fedorov, V. V., Kamkin, A. A. G., & Kiseleva, I. (2010). *Mechanosensitivity of the Heart* (Vol. 3): Springer.

Fung, Y.-c. (1965). *Foundations of solid mechanics*: Prentice Hall.

Fung, Y., & Cowin, S. (1994). Biomechanics: Mechanical properties of living tissues. *Journal of Applied Mechanics, 61*(4), 1007-1007.

Fuster, V., Gersh, B. J., Giuliani, E. R., Tajik, A. J., Brandenburg, R. O., & Frye, R. L. (1981). The natural history of idiopathic dilated cardiomyopathy. *The American journal of cardiology, 47*(3), 525-531.

Gaasch, W. H., Apstein, C. S., & Levine, H. J. (1985). Diastolic properties of the left ventricle. *The Ventricle: Basic and Clinical Aspects. Boston, MA: Martinus Nijhoff*, 143-170.

Gacek, A. (2012). *ECG Signal processing, classification and interpretation: a comprehensive framework of computational intelligence*: Springer.

Geerts, L., Bovendeerd, P., Nicolay, K., & Arts, T. (2002). Characterization of the normal cardiac myofiber field in goat measured with MR-diffusion tensor imaging. *American Journal of Physiology-Heart and Circulatory Physiology, 283*(1), H139-H145.

Ghaemi, H., Behdinan, K., & Spence, A. (2009a). In vitro technique in estimation of passive mechanical properties of bovine heart: Part II. Constitutive relation and finite element analysis. *Medical engineering & physics, 31*(1), 83-91.

Ghaemi, H., Behdinan, K., & Spence, A. D. (2009b). In vitro technique in estimation of passive mechanical properties of bovine heart part I. Experimental techniques and data. *Medical engineering & physics, 31*(1), 76-82.

Ghista, D. N., & Sandler, H. (1969). An analytic elastic-viscoelastic model for the shape and the forces in the left ventricle. *Journal of Biomechanics, 2*(1), 35-47.

Ghista, D. N., & Sandler, H. (1970). An indirect determination of the oxygen utilization of the human left ventricle. *Journal of Biomechanics, 3*(2), 161-174.

Göktepe, S., Acharya, S., Wong, J., & Kuhl, E. (2011). Computational modeling of passive myocardium. *International Journal for Numerical Methods in Biomedical Engineering, 27*(1), 1-12.

Göktepe, S., & Kuhl, E. (2010). Electromechanics of the heart: a unified approach to the strongly coupled excitation–contraction problem. *Computational mechanics, 45*(2-3), 227-243.

Gray, H., & Lewis, W. H. (1918). *Anatomy of the human body* (20th ed / throughly revised and re-edited by Warren H. Lewis. ed.). Philadelphia: Lea & Febiger.

Grewal, B. S. (1988). *The Mechanical Behaviour of the Left Ventricle of the Human Heart in Diastole*: PhD Thesis, University of Brunel.

Guccione, J. M., Kassab, G. S., & Ratcliffe, M. B. (2010). *Computational cardiovascular mechanics: modeling and applications in heart failure*: Springer.

Hall, J. E. (2011). *Guyton and Hall Textbook of Medical Physiology: Enhanced E-book*: Saunders.

Hamid, M. S., & Ghista, D. N. (1974). Finite element analysis of human cardiac structures. *Finite Element Analysis of Human Cardiac Structures,* in Finite Element Methods In Engineering, pp. 337–348. University of NewSouth Wales.

Haselgrove, J., & Huxley, H. (1973). X-ray evidence for radial cross-bridge movement and for the sliding filament model in actively contracting skeletal muscle. *Journal of molecular biology, 77*(4), 549-568.

Hashima, A. R., Young, A. A., McCulloch, A. D., & Waldman, L. K. (1993). Nonhomogeneous analysis of epicardial strain distributions during acute myocardial ischemia in the dog. *Journal of Biomechanics, 26*(1), 19-35.

Hassaballah, A. I., Hassan, M. A., Mardi, A. N., & Hamdi, M. (2013). An Inverse Finite Element Method for Determining the Tissue Compressibility of Human Left

Ventricular Wall during the Cardiac Cycle. *PLoS ONE, 8*(12), e82703. doi: 10.1371/journal.pone.0082703

Hassaballah, A. I., Hassan, M. A., Mardi, A. N., & Hamdi, M. (2014). Modeling the effects of myocardial fiber architecture and material properties on the left ventricle mechanics during rapid filling phase. *Journal of applied mathematics and information sciences; in press*.

Hassan, M., Hamdi, M., & Noma, A. (2012). The nonlinear elastic and viscoelastic passive properties of left ventricular papillary muscle of a Guinea pig heart. *Journal of the Mechanical Behavior of Biomedical Materials, 5*(1), 99-109.

Helm, P., Beg, M. F., Miller, M. I., & Winslow, R. L. (2005). Measuring and mapping cardiac fiber and laminar architecture using diffusion tensor MR imaging. *Communicative Cardiac Cell, 1047*, 296-307. doi: DOI 10.1196/annals.1341.026

Henein, M. Y. (2008). *Valvular heart disease in clinical practice*: Springer.

Hill, A. (1938). The heat of shortening and the dynamic constants of muscle. *Proceedings of the Royal Society of London. Series B, Biological Sciences, 126*(843), 136-195.

Holzapfel, G. A., & Ogden, R. W. (2009). Constitutive modelling of passive myocardium: a structurally based framework for material characterization. *Philosophical Transactions of the Royal Society A: Mathematical, Physical and Engineering Sciences, 367*(1902), 3445-3475.

Horowitz, A., Perl, M., Sideman, S., & Ritman, E. (1986). Comprehensive model for the simulation of left ventricle mechanics. *Medical and Biological Engineering and Computing, 24*(2), 150-156.

Hsu, E., Muzikant, A., Matulevicius, S., Penland, R., & Henriquez, C. (1998). Magnetic resonance myocardial fiber-orientation mapping with direct histological correlation. *American Journal of Physiology-Heart and Circulatory Physiology, 274*(5), H1627-H1634.

Hughes, T. J. (1994). *Mathematical foundations of elasticity*: DoverPublications. com.

Humphrey, J., Strumpf, R., & Yin, F. (1990a). Determination of a constitutive relation for passive myocardium: I. A new functional form. *Journal of biomechanical engineering, 112*(3), 333.

Humphrey, J., Strumpf, R., & Yin, F. (1990b). Determination of a constitutive relation for passive myocardium: II. Parameter estimation. *Journal of biomechanical engineering, 112*(3), 340.

Huyghe, J. M., van Campen, D. H., Arts, T., & Heethaar, R. M. (1991). A two-phase finite element model of the diastolic left ventricle. *Journal of Biomechanics, 24*(7), 527-538.

Iaizzo, P. A. (2009). *Handbook of cardiac anatomy, physiology, and devices*: Humana Press.

Janz, R. F., & Grimm, A. F. (1972). Finite-element model for the mechanical behavior of the left ventricle: Prediction of deformation in the potassium-arrested rat heart. *Circulation research, 30*(2), 244-252.

Katholi, R. E., & Couri, D. M. (2011). Left ventricular hypertrophy: major risk factor in patients with hypertension: update and practical clinical applications. *International journal of hypertension,*Volume 2011, Article ID 495349, 10 pages.

Katz, A. (2011). *Physiology of the Heart*: Wolters Kluwer Health.

Keele, K. D. (1951). Leonardo da Vinci, and the movement of the heart. [Biography]. *Journal of the Royal Society of Medicine, 44*(3), 209-213.

Kerckhoffs, R., Bovendeerd, P., Kotte, J., Prinzen, F., Smits, K., & Arts, T. (2003). Homogeneity of cardiac contraction despite physiological asynchrony of depolarization: a model study. *Annals of Biomedical Engineering, 31*(5), 536-547.

Kim, H. C., Min, B. G., Lee, M. M., Seo, J. D., Lee, Y. W., & Han, M. C. (1985). Estimation of local cardiac wall deformation and regional wall stress from biplane coronary cineangiograms. *Biomedical Engineering, IEEE Transactions* (7), 503-512.

Klabunde, R. E. (2011). *Cardiovascular physiology concepts*: Wolters Kluwer Health.

Koeppen, B. M., & Stanton, B. A. (2009). *Berne & Levy Physiology*: Elsevier Health Sciences.

Kohl, P., Sachs, F., & Franz, M. R. (2011). *Cardiac mechano-electric coupling and arrhythmias*: OUP Oxford.

Krishnamoorthy, C. S. (1995). *Finite element analysis : theory and programming*. New Delhi [u.a.]: Tata McGraw-Hill.

LeGrice, I., Hunter, P., Young, A., & Smaill, B. (2001). The architecture of the heart: a data–based model. *Philosophical Transactions of the Royal Society of London. Series A: Mathematical, Physical and Engineering Sciences, 359*(1783), 1217-1232.

LeGrice, I. J., Smaill, B., Chai, L., Edgar, S., Gavin, J., & Hunter, P. J. (1995). Laminar structure of the heart: ventricular myocyte arrangement and connective tissue architecture in the dog. *American Journal of Physiology-Heart and Circulatory Physiology, 269*(2), H571-H582.

Levy, M. N., Pappano, A. J., & Berne, R. M. (2007). *Cardiovascular physiology*: Mosby Elsevier.

Lin, D., & Yin, F. (1998). A multiaxial constitutive law for mammalian left ventricular myocardium in steady-state barium contracture or tetanus. *Journal of biomechanical engineering, 120*(4), 504-517.

Lombaert, H., Peyrat, J. M., Croisille, P., Rapacchi, S., Fanton, L., Cheriet, F., Ayache, N. (2012). Human Atlas of the Cardiac Fiber Architecture: Study on a Healthy Population. *IEEE Transactions on Medical Imaging, 31*(7), 1436-1447. doi: Doi 10.1109/Tmi.2012.2192743

Lombaert, H., Peyrat, J. M., Croisille, P., Rapacchi, S., Fanton, L., Clarysse, P., Ayache, N. (2011). Statistical Analysis of the Human Cardiac Fiber Architecture from DT-MRI. *Functional Imaging and Modeling of the Heart, 6666*, 171-179.

Malvern, L. E. (1969). *Introduction to the Mechanics of a Continuous Medium*.

Marchesseau, S., Delingette, H., Sermesant, M., Sorine, M., Rhode, K., Duckett, S.,. Ayache, N. (2012). Preliminary specificity study of the Bestel-Clément-Sorine electromechanical model of the heart using parameter calibration from medical images. *Journal of the Mechanical Behavior of Biomedical Materials*, Volume 20, Pages 259–271.

Martini, F., Timmons, M. J., & Tallitsch, R. B. (2012). *Human anatomy* (7th ed.). Boston, Mass. ; London: Benjamin Cummings.

McPherson, D. D., Skorton, D. J., Kodiyalam, S., Petree, L., Noel, M. P., Kieso, R., Chandran, K. B. (1987). Finite element analysis of myocardial diastolic function

using three-dimensional echocardiographic reconstructions: application of a new method for study of acute ischemia in dogs. *Circulation research, 60*(5), 674-682.

Mirsky, I. (1969). Left ventricular stresses in the intact human heart. *Biophysical journal, 9*(2), 189-208.

Niederer, S. A., & Smith, N. P. (2009). The role of the Frank–Starling law in the transduction of cellular work to whole organ pump function: A computational modeling analysis. *PLoS computational biology, 5*(4), e1000371.

Nikravesh, P., Chandran, K., Skorton, D., Pandian, N., & Kerber, R. (1981). *3-D finite element reconstruction of left ventricular geometry from cross-sectional echocardiographic recordings.* Paper presented at the Proc. Biomech. Symp. New York, AMD.

Nonogi, H., Hess, O. M., Ritter, M., & Krayenbuehl, H. P. (1988). Diastolic properties of the normal left ventricle during supine exercise. *British heart journal, 60*(1), 30-38.

Otto, C. M., & Bonow, R. O. (2013). *Valvular Heart Disease: A Companion to Braunwald's Heart Disease*: Elsevier Health Sciences.

Périé, D., Dahdah, N., Foudis, A., & Curnier, D. (2013). Multi-parametric MRI as an indirect evaluation tool of the mechanical properties of in-vitro cardiac tissues. *BMC cardiovascular disorders, 13*(1), 1-9.

Pfeffer, M., & Braunwald, E. (1990). Ventricular remodeling after myocardial infarction. Experimental observations and clinical implications. *Circulation, 81*(4), 1161-1172.

Phibbs, B. (2007). *The human heart: a basic guide to heart disease*: Lippincott Williams & Wilkins.

Phillips, C. A., & Petrofsky, J. S. (1984). Myocardial material mechanics: characteristic variation of the circumferential and longitudinal systolic moduli in left ventricular dysfunction. *Journal of Biomechanics, 17*(8), 561-568.

Plowman, S. A., & Smith, D. L. (2013). *Exercise physiology for health fitness and performance*: Wolters Kluwer Health.

Rao, G. H., & Thanikachalam, S. (2005). *Coronary Artery Disease: Risk Promoters, pathophysiology and Prevention by Rao*: Jaypee Brothers Publishers. Delhi, India.

Reddy, J. N. (2008). *An introduction to continuum mechanics*: Cambridge university press.

Rhoades, R. A., & Bell, D. R. (2009). *Medical physiology: principles for clinical medicine*: Wolters Kluwer Health.

Rn, D. M. M. (2007). *The Complete Study Guide to Learning the Electrocardiogram*: http://www.lulu.com/shop/douglas-martin-msn-rn/the-complete-study-guide-to-learning-the-electrocardiogram/ebook/product-17517817.html.

Rohmer, D., Sitek, A., & Gullberg, G. T. (2006). Reconstruction and visualization of fiber and laminar structure in the normal human heart from ex vivo DTMRI data: Tech. Rep., Lawrence Berkeley National Laboratory.

Sandhar, H. (2004). *Textbook of Physiology*: B. Jain Publishers. New Delhi, India.

Sandler, H., & Dodge, H. T. (1963). Left ventricular tension and stress in man. *Circulation research, 13*(2), 91-104.

Schmid, P., Niederer, P., Lunkenheimer, P., & Torrent-Guasp, F. (1997). The anisotropic structure of the human left and right ventricles. *Technol Health Care, 5*(1-2), 29-43.

Scollan, D. F., Holmes, A., Winslow, R., & Forder, J. (1998). Histological validation of myocardial microstructure obtained from diffusion tensor magnetic resonance imaging. *American Journal of Physiology-Heart and Circulatory Physiology, 275*(6), H2308-H2318.

Sembulingam, K., & Sembulingam, P. (2002). *Essentials of medical physiology*: New Delhi: Jaypee Brothers, 2002.

Sengupta, P. P., Korinek, J., Belohlavek, M., Narula, J., Vannan, M. A., Jahangir, A., & Khandheria, B. K. (2006). Left ventricular structure and function: basic science for cardiac imaging. *Journal of the American College of Cardiology, 48*(10), 1988-2001.

Shapiro, E. P., & Rademakers, F. E. (1997). Importance of oblique fiber orientation for left ventricular wall deformation. *Technol Health Care, 5*(1-2), 21-28.

Sherwood, L. (2012). *Human physiology: from cells to systems*: Brooks/Cole Publishing Company.

Shim, J., Grosberg, A., Nawroth, J. C., Kit Parker, K., & Bertoldi, K. (2012). Modeling of cardiac muscle thin films: Pre-stretch, passive and active behavior. *Journal of biomechanics, 45*(5), 832-841.

Sicar, S. (2008). *Principles of medical physiology*: Thieme.

Smaill, B. H., LeGrice, I. J., Hooks, D. A., Pullan, A. J., Caldwell, B. J., & Hunter, P. J. (2004). Cardiac structure and electrical activation: models and measurement. *Clinical and experimental pharmacology and physiology, 31*(12), 913-919.

Smith, J., & Roberts, R. (2011). *Vital Signs for Nurses: An Introduction to Clinical Observations*: Wiley. com.

Snell, R. S. (2011). *Clinical anatomy by regions*: Wolters Kluwer Health.

Sperelakis, N., Kurachi, Y., Terzic, A., & Cohen, M. V. (2000). *Heart physiology and pathophysiology*: Access Online via Elsevier.

Steere, A. C., Batsford, W. P., Weinberg, M., Alexander, J., Berger, H. J., Wolfson, S., & Malawista, S. E. (1980). Lyme carditis: cardiac abnormalities of Lyme disease. *Annals of internal medicine, 93*(1), 8.

Stevens, C., & Hunter, P. J. (2003). Sarcomere length changes in a 3D mathematical model of the pig ventricles. *Progress in biophysics and molecular biology, 82*(1), 229-241.

Stevens, C., Remme, E., LeGrice, I., & Hunter, P. (2003). Ventricular mechanics in diastole: material parameter sensitivity. *Journal of Biomechanics, 36*(5), 737-748.

Stouffer, G. (2011). *Cardiovascular hemodynamics for the clinician*: Wiley. com.

Streeter, D. D. (1979). Gross morphology and fiber geometry of the heart. *Handbook of physiology*, 61-112.

Streeter, D. D., Vaishnav, R. N., Patel, D. J., Spotnitz, H. M., Ross, J., & Sonnenblick, E. H. (1970). Stress distribution in the canine left ventricle during diastole and systole. *Biophysical journal, 10*(4), 345-363.

Streeter Jr, D. D., Spotnitz, H. M., Patel, D. P., Ross Jr, J., & Sonnenblick, E. H. (1969). Fiber orientation in the canine left ventricle during diastole and systole. *Circulation research, 24*(3), 339-347.

Sutton, M. G. S. J., & Sharpe, N. (2000). Left Ventricular Remodeling After Myocardial Infarction : Pathophysiology and Therapy. *Circulation, 101*(25), 2981-2988. doi: 10.1161/01.cir.101.25.2981

Taber, L. A., Yang, M., & Podszus, W. W. (1996). Mechanics of ventricular torsion. *Journal of Biomechanics, 29*(6), 745-752. doi: Doi 10.1016/0021-9290(95)00129-8

Toronto, A. F. (1964). *Structure and function of the heart*. Boston: D.C. Heath and Co.

Tözeren, A. (1983). Static analysis of the left ventricle. *Journal of biomechanical engineering, 105*(1), 39.

Ubbink, S., Bovendeerd, P., Delhaas, T., Arts, T., & Van de Vosse, F. (2006). Towards model-based analysis of cardiac MR tagging data: relation between left ventricular shear strain and myofiber orientation. *Medical Image Analysis, 10*(4), 632-641.

Usyk, T., Mazhari, R., & McCulloch, A. (2000). Effect of laminar orthotropic myofiber architecture on regional stress and strain in the canine left ventricle. *Journal of Elasticity, 61*(1), 143-164.

Van Campen, D., Huyghe, J., Bovendeerd, P., & Arts, T. (1994). Biomechanics of the heart muscle. *EUROPEAN JOURNAL OF MECHANICS SERIES A SOLIDS, 13*, 19-19.

Venugopal, J. R., Prabhakaran, M. P., Mukherjee, S., Ravichandran, R., Dan, K., & Ramakrishna, S. (2012). Biomaterial strategies for alleviation of myocardial infarction. *Journal of the Royal Society Interface, 9*(66), 1-19. doi: DOI 10.1098/rsif.2011.0301

Veress, A. I., Gullberg, G. T., & Weiss, J. A. (2005). Measurement of strain in the left ventricle during diastole with cine-MRI and deformable image registration.

Vetter, F. J., & McCulloch, A. D. (2000). Three-dimensional stress and strain in passive rabbit left ventricle: a model study. *Annals of Biomedical Engineering, 28*(7), 781-792.

Vinson, C. (1977). *Analysis of Stress and Deformation in the Human Left Ventricle.* Brunel University.

Walsh, M., & Crumbie, A. (2007). *Watson's clinical nursing and related sciences*: Elsevier Health Sciences.

Wang, H., Gao, H., Luo, X., Berry, C., Griffith, B., Ogden, R., & Wang, T. (2012). Structure-based finite strain modelling of the human left ventricle in diastole. *International Journal for Numerical Methods in Biomedical Engineering*.

Wang, V. Y., Lam, H., Ennis, D. B., Cowan, B. R., Young, A. A., & Nash, M. P. (2009). Modelling passive diastolic mechanics with quantitative MRI of cardiac structure and function. *Medical Image Analysis, 13*(5), 773.

Watanabe, H., Sugiura, S., Kafuku, H., & Hisada, T. (2004). Multiphysics simulation of left ventricular filling dynamics using fluid-structure interaction finite element method. *Biophysical journal, 87*(3), 2074-2085.

Watanabe, S., Shite, J., Takaoka, H., Shinke, T., Imuro, Y., Ozawa, T., Paredes, O. L. (2006). Myocardial stiffness is an important determinant of the plasma brain natriuretic peptide concentration in patients with both diastolic and systolic heart failure. *European heart journal, 27*(7), 832-838.

Wheeler, D. S., Wong, H. R., & Shanley, T. P. (2009). *Cardiovascular Pediatric Critical Illness and Injury*: Springer.

Widmaier, E. (2013). *Human physiology*: McGraw-Hill.

Wong, A. Y. (1973). Myocardial mechanics: application of sliding-filament theory to isovolumic concentration of the left ventricle. *Journal of Biomechanics, 6*(5), 565-581.

Wong, A. Y., & Rautaharju, P. (1968). Stress distribution within the left ventricular wall approximated as a thick ellipsoidal shell. *American Heart Journal, 75*(5), 649-662.

Woods, R. H. (1892). A few applications of a physical theorem to membranes in the human body in a state of tension. *Transactions of the Royal Academy of Medicine in Ireland, 10*(1), 417-427.

Xia, L., Huo, M., Wei, Q., Liu, F., & Crozier, S. (2005). Analysis of cardiac ventricular wall motion based on a three-dimensional electromechanical biventricular model. *Physics in Medicine and Biology, 50*(8), 1901.

Yang, F., Zhu, Y. M., Magnin, I. E., Luo, J. H., Croisille, P., & Kingsley, P. B. (2012). Feature-based interpolation of diffusion tensor fields and application to human cardiac DT-MRI. *Medical Image Analysis, 16*(2), 459-481. doi: DOI 10.1016/j.media.2011.11.003

Yettram, A., & Beecham, M. (1998). An analytical method for the determination of along-fibre to cross-fibre elastic modulus ratio in ventricular myocardium—a feasibility study. *Medical engineering & physics, 20*(2), 103-108.

Yettram, A., Vinson, C. A., & Gibson, D. (1983). Effect of myocardial fibre architecture on the behaviour of the human left ventricle in diastole. *Journal of biomedical engineering, 5*(4), 321-328.

Yin, F., Chan, C., & Judd, R. M. (1996). Compressibility of perfused passive myocardium. *American Journal of Physiology-Heart and Circulatory Physiology, 271*(5), H1864-H1870.

Yusuf, S., Hawken, S., Ôunpuu, S., Dans, T., Avezum, A., Lanas, F., Varigos, J. (2004). Effect of potentially modifiable risk factors associated with myocardial infarction in 52 countries (the INTERHEART study): case-control study. *The Lancet, 364*(9438), 937-952.

Zhong, L., Ghista, D., & Tan, R. (2012). Left ventricular wall stress compendium. *Computer Methods in Biomechanics and Biomedical Engineering, 15*(10), 1015-1041.

ZHONG, L., GHISTA, D. N., NG, E. Y.-K., CHUA, T. S.-J., LEE, C. N., LIM, S. T., CHUA, L. P. (2007). Left ventricular functional indices based on left ventricular elastances and shape factor. *Journal of Mechanics in Medicine and Biology, 07*(01), 107-116. doi: doi:10.1142/S0219519407002182

Zienkiewicz, O. (1971). The finite element in engineering science. *McGrau Hill, London*.

Zienkiewicz, O. C., & Taylor, R. L. (2000). *The Finite Element Method: Solid Mechanics* (Vol. 2): Butterworth-heinemann.

LIST OF PUBLICATIONS AND PAPERS PRESENTED

1. Hassaballah, A. I., Hassan, M. A., Mardi, A. N., & Hamdi, M. (2013). An Inverse Finite Element Method for Determining the Tissue Compressibility of Human Left Ventricular Wall during the Cardiac Cycle. *PLoS ONE*, 8(12), e82703. doi: 10.1371/journal.pone.0082703

2. Hassaballah, A. I., Hassan, M. A., Mardi, A. N., & Hamdi, M. (2014). Modeling the effects of myocardial fiber architecture and material properties on the left ventricle mechanics during rapid filling phase. *Journal of applied mathematics and information sciences,* In press